DOCTOR OF PHILOSOPHY

Automatic Cell Tracking For Studying Large Epithelial Sheets Of Cells And Its Application To Chicken Gastrulation

Karjalainen, Antti I.

Award date:
2015

AUTOMATIC CELL TRACKING FOR STUDYING LARGE EPITHELIAL SHEETS OF CELLS AND ITS APPLICATION TO CHICKEN GASTRULATION

Antti I. Karjalainen

Thesis presented for the degree of

Doctor of Philosophy

University of Dundee

September 2015

TABLE OF CONTENTS

LIST OF FIGURES

LIST OF TABLES

LIST OF ABBREVIATIONS

2D	2 Dimensional
3D	3 Dimensional
AOTF	Acousto-Optic Tunable Filter
CAM	Computer Aided Microscopy
CMOS	Complementary Metal–Oxide–Semiconductor
CPM	Cellular Potts Model
CUDA	Compute Unified Device Architecture
DFT	Discrete Fourier Transform
DSLM	Digital Scanned laser Light sheet fluorescence Microscopy
EGFP	Enhanced Green Fluorescent Protein
EMT	Epithelial Mesenchymal Transition
FFT	Fast Fourier Transform
FGF	Fibroblast Growth Factor
GPU	Graphics Processor Unit
GUI	Graphical User Interface
GFP	Green Fluorescent Protein
LSM	Light-Sheet Microscope

Myr-EGFP	Myristoylated Enhanced Green Fluorescent Protein
PCP	Pentachloropseudilin
PCP pathway	Planar Cell Polarity pathway
PIV	Particle Image Velocimetry
ROI	Region Of Interest
SPIM	Selective Plane Illumination Microscopy
VEGF	Vascular Endothelial Growth Factor

ACKNOWLEDGEMENTS

I would like to thank Professor Kees Weijer, who gave me the opportunity to work on this interesting research project. Close supervision of Kees was essential for me to learn about the field, to keep applying new techniques to tackle the research problems and to finally compose all the findings into this thesis.

I would like to also thank Dr Emil Rozbicki for sharing ideas and for the pleasant work environment in the lab during first two years of my Ph.D. project. The image sequences Emil acquired were essential for my research.

Thirdly, I thank Dr Manli Chuai for carrying out biological experiments and thus generating data for me to analyse.

I also thank Dr Richard Tyson for the work we did together with the light sheet microscope.

I am grateful to Professor Helen Sang and to Dr Feifei Song for development of the chicken strain that was basis for my research.

Finally, I want to thank my family for the support. I especially thank Vanya for all the love and caring she has given me during these years of our Ph.D.s. Vanya's comments and suggestions have greatly helped me to reach the stage where I am at the moment.

DECLARATION

I hereby declare that this thesis is my own work and it presents my original research. It has not been submitted anywhere for any award. Whenever contributions of others are involved, every effort is made to state it clearly and references to the literature are provided.

Signed ……..

Antti I. Karjalainen

Date ……..

STATEMENT

I certify that Antti I. Karjalainen has fulfilled the conditions of the University of Dundee and that he is qualified to submit the accompanying thesis in the application for the degree of Doctor of Philosophy.

Signed ……..

Professor Cornelis Jan Weijer, FRSE

Date ……..

ABSTRACT

During gastrulation of chicken embryo the three major germ layers, ectoderm, mesoderm and endoderm, are formed and organised into the correct topological order. A key event of the gastrulation is formation of the primitive streak that is characterised by large scale vortical flows that involve an order of >200,000 cells. During this self-organised process individual epithelial cells are migrating in a highly coordinated manner. The cell behaviours driving the flows and migration are unknown due to the lack of high resolution time lapse sequences showing each individual cell and its behaviour in detail. Several hypotheses including cell-cell intercalation, chemotaxis and oriented cell divisions, have been put forward to explain how individual cells induce the highly coordinated formation of the primitive streak. Furthermore, another open question is which of the observed motions of cells are active and which occur passively as a result from the active motions.

To answer these questions we use light sheet microscopy to acquire large volumetric time-lapse image sequences covering more than half of the chick embryo. We developed an algorithm to automatically extract the apical cell surface from the acquired volumetric image sequences. Manual tracking and segmentation of all the individual cells from the embryo wide image sequences is unfeasible. To solve this problem, we developed algorithms to segment cell membranes and to automatically track each individual cell during primitive streak formation. This provided highly detailed data of position, size, cross sectional area and neighbours of each cell throughout the time sequence. The quality of tracking achieved by the automatic tracking algorithm used was validated by comparing the automatically obtained tracks with tracks from the semi-automatically annotated domains. Large scale high resolution imaging and

automatic tracking has not been performed previously in chicken epiblast and this provided a good basis for quantitative analysis of tissue and cell behaviours.

Analysis of the cell tracking data reveals a set of mesendoderm cells performing cell intercalation, which drives elongation of the primitive streak. The intercalation process also pulls cells from the lateral positions to the midline of the embryo and causes tissue to buckle in the anterior end of the forming primitive streak. Thus intercalation appears to drive the observed vortical tissue flows. Simultaneously with the intercalation, a set of mesendoderm cells undergoes apical contraction culminating in ingression in the site of primitive streak. This weaker tissue deformation process partially counteracts the elongation of the primitive streak but facilitates pulling of cells towards the midline. Additionally, we found that at the site of the primitive streak both apical cell shapes and orientation of cell divisions are polarised perpendicular to the streak. This implies that that oriented cell divisions are unlikely to drive the primitive streak formation.

1 INTRODUCTION

1.1 Gastrulation in chicken embryo

Gastrulation is a fundamentally important event in the development of higher organisms like amniotes. During this process the three major germ layers, the ectoderm, mesoderm and endoderm are formed and organised into the correct topological order[1]. During this process individual epithelial and mesenchymal cells migrate in a coordinated manner[2]. These coordinated cell motion patterns give rise to the primitive streak, an axial structure in the midline of the embryo[1]. Epithelial cells at the site of the primitive streak undergo an epithelial to mesenchymal transition (EMT)[3]. These ingressing cells then move further from the site of the primitive streak underneath the epiblast to ultimately giving a rise to organs and tissues[1].

Development starts with the fertilisation of the egg cell, which leads to the formation of a single cell zygote[1]. The zygote then undergoes multiple rapid cell division cycles until the egg is laid 24 hours after the fertilisation[1]. At the time the egg is laid the embryo consist of around 50,000 cell indicating that around 15 rounds cell divisions took place[4]. This rate of divisions indicates a cell cycle length of around 1.6 hours. During these early stages the blastoderm forms into an almost flat radially symmetric disk[1]. The disk consists of a single layer of epithelial cells, the epiblast. The cells of the epiblast are highly polarised along their apical basal direction and the cells are connected to each other with apical tight and adherens junctions[4,5]. The outer boundary of the epiblast disc is attached to the vitelline membrane. The cells in the outer boundary move outward on the vitelline membrane keeping embryo under tension and enabling the development[6, 7]. The inner region of the epithelial disk is called area pellucida, the surrounding region is called area opaca. The area opaca gives rise to the extra embryonic tissues (Figure 1.1)[1]. At later stages of development the cells in the area opaca become less columnar than

cells in the area pellucida in the central area of the embryo[1]. Simultaneously, a transient structure, the hypoblast starts to develop underneath the epithelial sheet (epiblast). The hypoblast is formed from small groups of individual epiblast cells that have undergone an EMT and have ingressed Figure 1.1)[3, 8]. The hypoblast has been shown to play a role in correct localisation of the primitive streak via inhibition of Wnt and Nodal signalling[9].

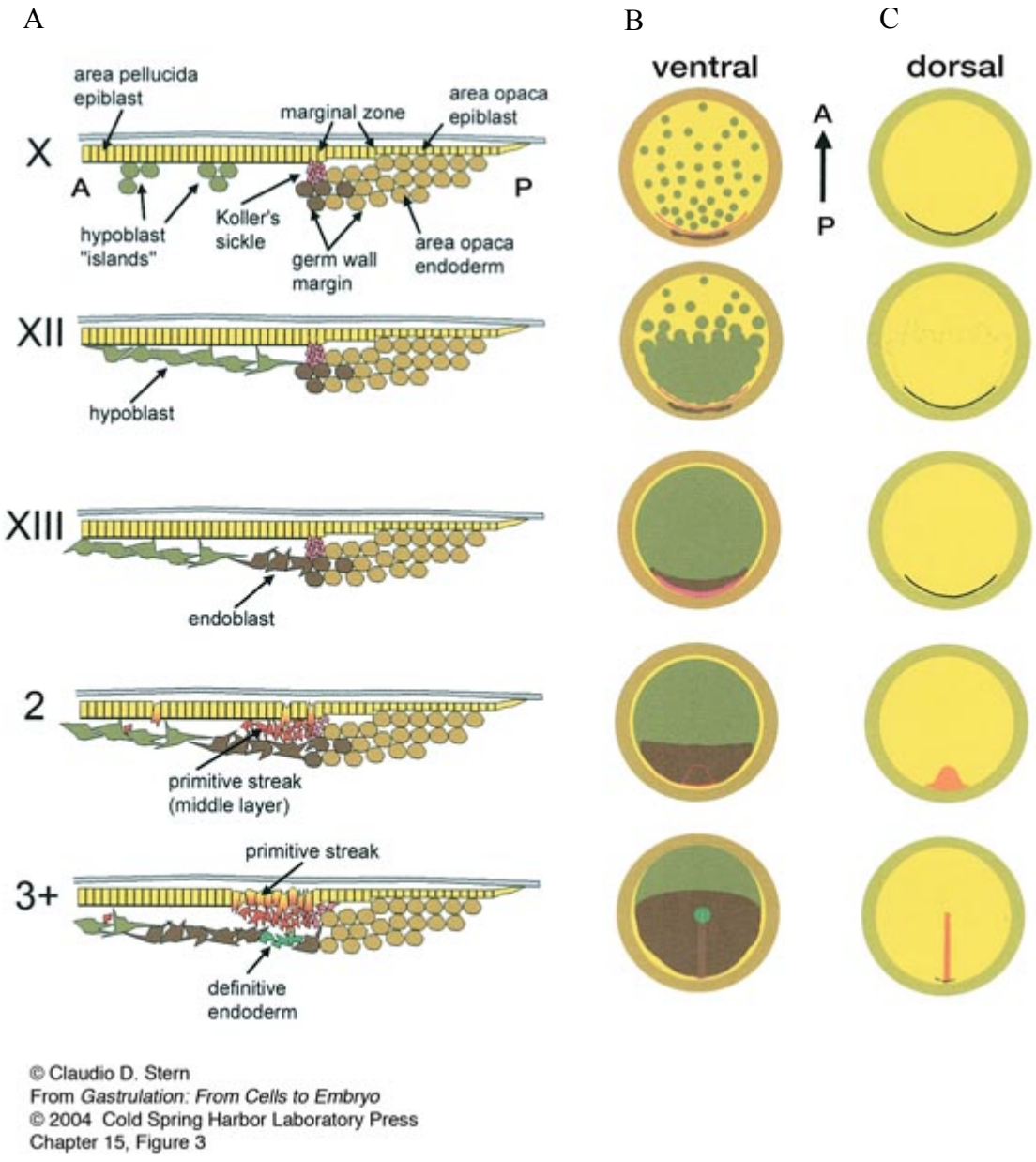

Figure 1.1 Structure and stages of chicken embryo during gastrulation. A) Cross-sectional view of the blastoderm of chicken embryo. **B-C)** Embryo viewed from ventral side and from dorsal side, respectively. Following structures are represented: vitelline membrane (grey), epiblast (yellow), hypoblast (dark green), area opaca endoderm (light brown), endoblast (dark brown), primitive streak mesendoderm (red) and Koller's sickle (purple).

The boundary zone between the area opaca and area pellucida is known as the marginal zone. In the posterior end of the marginal zone a shallow Vg1 gradient is present[1]. Under the epiblast in the posterior marginal zone lies a sickle shaped population of cells known as Koller's sickle (Figure 1.1)[2]. This cell population is tightly attached to the epiblast and marks the site from where the primitive streak starts to form[1].

After formation of these structures the first movements start to occur in the epiblast and hypoblast of the embryo[10]. Cells start to move along the midline of the embryo from the posterior marginal zone towards the anterior area pellucida (Figure 1.2)[10]. Simultaneously, cells from the lateral to the posterior marginal zone start to move towards the midline. Furthermore, cells in the anterior end of the area pellucida are moving outward from the midline of the embryo. Together all these movements form two counter-rotating vortical flows (Figure 1.3)[2, 10-13]. The cellular processes driving these flows are unknown and the hypothetical mechanisms reported in literature are reviewed in detail in the next section[2]. The two vortical flows transport cells from lateral positions to the midline of the embryo in the posterior area pellucida. At this site the cells start to form a thicker cell layer and finally cells start to undergo EMT and ingress to form mesoderm and endoderm[1]. The forming primitive streak now starts to be macroscopically visible. This is followed by extension of the primitive streak into the anterior direction. Soon after this the primitive streak starts to extend also in the posterior direction, whilst the lateral flows of cells continue to bring more cells to the midline of the embryo[4].

After the primitive streak has extended in anterior direction over 70% of the epiblast, cells in the anterior end of the primitive streak, the tip of the streak, start to reorganise into a distinct structure known as Hensen's node[1]. After its formation Hensen's node starts to move towards the posterior end of the embryo in a process that is known as regression[4]. The regression of the Hensen's node initiates the formation of the floor plate and notochord[1].

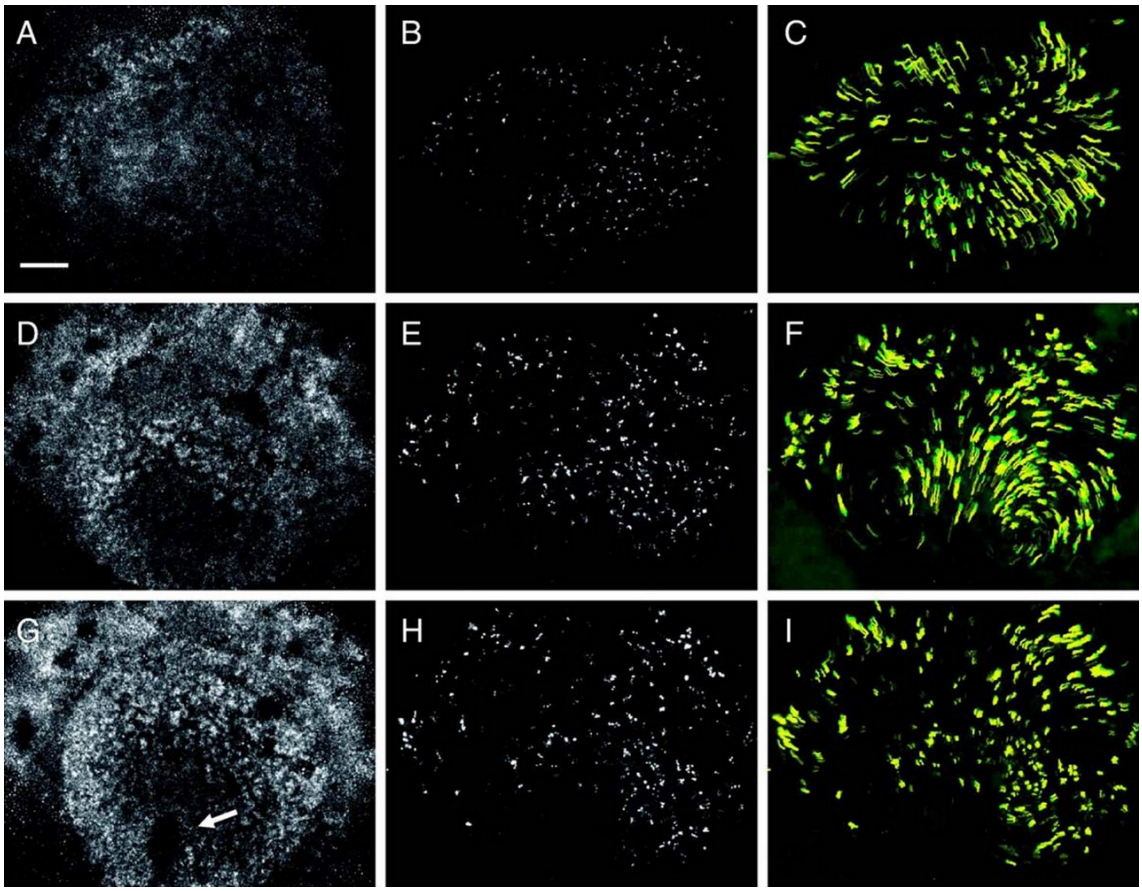

Figure 1.2 Tracking of labelled cells in epiblast during primitive streak formation. **A-C)** Bright-field image, fluorescence image and cell tracks of the same embryo 7 hours after the start of the development. Yellow lines are 4 h long tracks and the green lines indicate the tracks over the last 1 hour. Scale bar is 0.5 mm. **D-F)** Same embryo after 15 hours of development. **G-I)** The embryo after 18 hours of development. Posterior-anterior axis is pointing up in the images. White arrow is pointing the primitive streak in panel G. This figure has been adapted from following source[10].

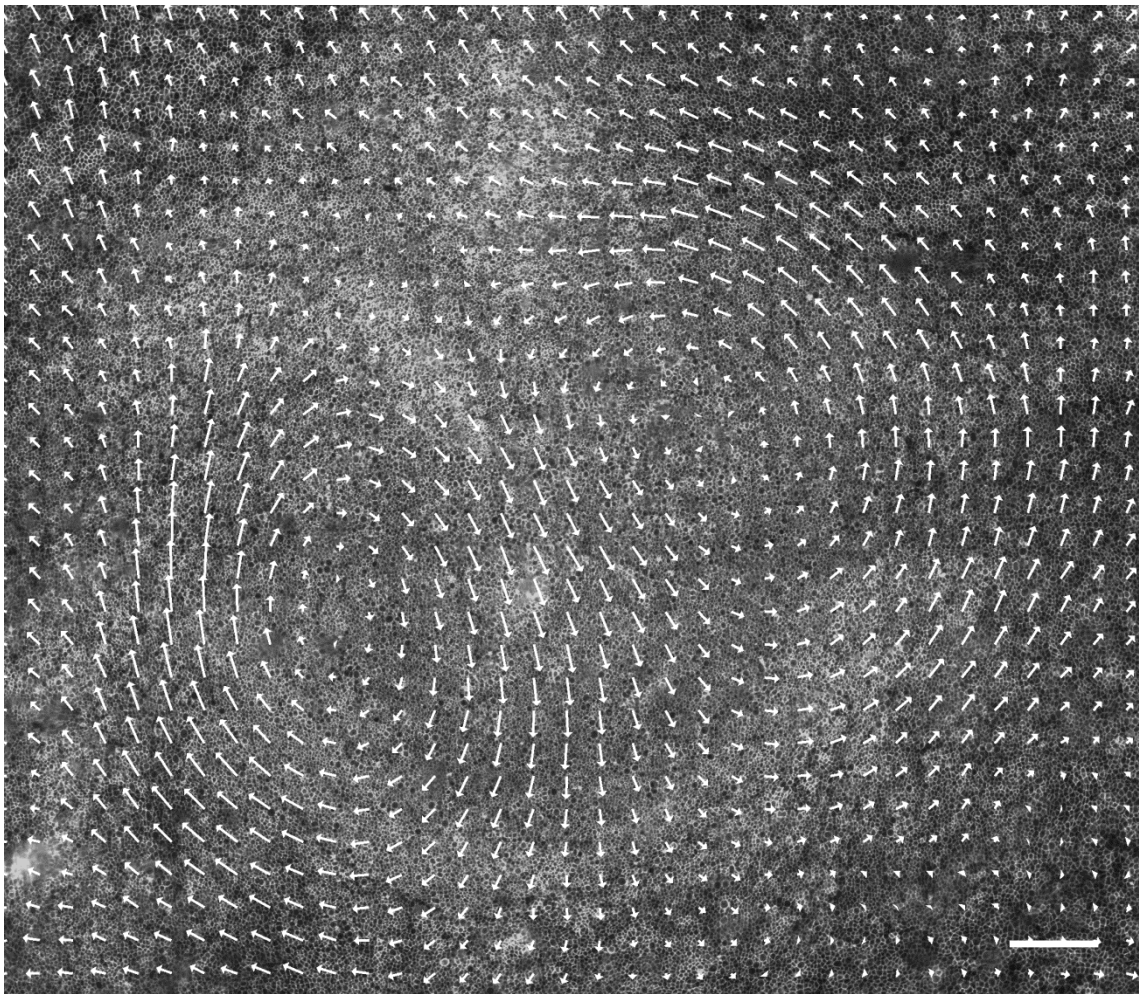

Figure 1.3 Tissue velocity fields in epiblast of chicken embryo during primitive streak formation. White arrows show direction of tissue flow. The white scale bar is 300 μm in length 4 μm/min in tissue velocity.

Chicken embryos are a convenient model for studying gastrulation as the development of the embryo occurs outside the mother organism. Additionally the embryos can be cultured ex-ovo in a sample dish, which facilitates the imaging of the embryos[14]. Finally, the flat shape of the embryos facilitates imaging of the embryos.

An interesting question is which cellular mechanisms drive the observed cell flows in the epiblast of chicken embryo during the primitive streak formation? Furthermore, another open question is which of the observed motions of cells are active and which occur passively as a result from the active motions elsewhere? Several hypothetical

mechanisms have been proposed to drive the observed cell flows. An overview of these proposed mechanisms is given in the following section.

1.2 Mechanisms driving the primitive streak formation

As described in the previous section primitive streak formation in the chick embryo is characterised by cell flows around two centres (Figure 1.3). These flows transport mesendoderm precursor cells to the midline of the embryo to a site where the primitive streak will start to form and extend along the midline of the embryo[10, 11, 13, 15]. The mesendoderm tissue is generated in a sickle shaped region between posterior area pellucida and posterior marginal zone. The mesendoderm cells are showing different cell behaviours and the inhibition of the mesendoderm differentiation blocks the observed cell flows moving cell the midline of the embryo[13, 16]. Mechanisms proposed to drive the cell flows include oriented cell divisions, cell-cell intercalation, chemotaxis, movement of extra cellular matrix, localised ingression and cell shape changes[2, 4].

1.2.1 Oriented cell divisions

Oriented cell divisions have been shown to a play role in animal-vegetal body axis elongation in dorsal tissues during zebrafish gastrulation[17]. To drive tissue elongation in the certain direction cells are assumed to divide in a polarised manner (Figure 1.4 AB). It has been proposed that similar mechanisms could drive primitive streak elongation in chicken embryos[18]. The authors showed that divided daughter cells were aligned along the formed primitive streak. Is not clear whether this actively drives the primitive streak formation or is a consequence of other mechanisms. Experimental work has shown that inhibition of cell divisions does not completely block formation of the primitive streak[13]. Furthermore, computer simulations have shown that cell divisions cannot be the sole mechanism driving the primitive streak formation[19]. Although, both of these

studies suggest that the oriented cell divisions could facilitate the formation and maintain the observed cell flows.

1.2.2 Cell-cell intercalation

A second mechanism proposed to drive the observed cell flows in the chicken epiblast during the gastrulation is cell-cell intercalation (Figure 1.3)[20]. This mechanism operates by interdigitating cells in a polarised manner. This mechanism can extend tissue in one direction while contracting in a perpendicular direction (Figure 1.4 CD). Some direct evidence obtained utilising multiphoton microscopy to image small groups of cells supports the hypothesis that cell-cell intercalation could be a process involved in primitive streak formation[15]. Cell-cell intercalation plays a role in the morphogenesis of frog and zebrafish mesoderm[21, 22]. In both cases the intercalation is thought to depend on the planar cell polarity (PCP) pathway. This pathway is responsible of controlling cell polarity (mediolateral cross section and apical-basal length) in plane of the epithelial layer which then in turn enables cells to move relative to each other in process called intercalation. Additionally, knockdown of several PCP pathway components simultaneously interfered with formation of the primitive streak[15].

1.2.3 Cell shape change and localised ingression

Epithelial cells changing their length in apical-basal direction would result in a reduction of the surface area of these cells[23]. Such changes in the cross sections of the epithelial sheet have been found to contribute and to drive morphological processes in Drosophila melanogaster [23]. Furthermore, epithelial cells may undergo anisotropic changes of their cross sections inducing change in shape of the whole tissue[24]. Such a process can actively drive tissue deformation and influence to the surrounding connected tissues (Figure 1.4 G)[24]. Similar cell cross section altering processes have been identified during zebrafish development[25]. Anisotropic or isotropic changes in the

cross sectional area of cells could contribute to the initiation and further elongation of the primitive streak in chicken embryos[4].

The hypoblast forms by ingression of randomly localised epithelial cells[26]. It is possible that ingression of the these cells would facilitate or drive primitive streak formation[4]. This mechanism would need to act in a differential manner occurring only in the area of contraction but not in the other regions[4]. If this mechanism would act in the posterior area pellucida at the site of the primitive streak formation this would induce contraction of tissue and thus contribute to the cell flows towards the site of primitive streak (Figure 1.4 EF)[4]. In a recent study it was suggested that a Nodal dependent effect promotes cell ingression in the site of the primitive streak formation and consecutively drives the observed cell flows[27].

1.2.4 Chemotaxis of subpopulation of cells

Yet another mechanism to explain primitive streak formation in the epiblast of the chicken embryo is chemotaxis[10, 28]. In this mechanism chemotactic agents in the epiblast are responsible for directing the movement of cells. The agents may either be chemotactic attractants or chemotactic repellents, which together may induce movement of surrounding cells (Figure 1.4 H). Theoretical calculations and simulations have provided evidence for feasibility of such a hypothesis, although these simulations required that cells in the streak had to adhere more strongly to each other than to other cells[29]. The computation framework used in this study was Cellular Potts Model (CPM)[30]. In another theoretical work computer simulations were used to construct two adjacent chemotactic regions into the site of forming primitive streak. Chemo attractant was produced in the posterior side while a chemo repellent was produced in the anterior cells (Figure 1.4 H)[31]. Together these two chemotactic agents were able to replicate the observed vortical cell flows in the epiblast of chicken embryo during the primitive

streak formation. It remains unclear whether signalling molecules like FGF growth factors or VEGF growth factors could be the in-vivo attractant and repellent chemicals and further experimental work would be required to confirm this[4].

1.2.5 Movement of the extracellular matrix

The extracellular matrix is a structure located at the basal side of the of epiblast cells[32]. This basement membrane like structure is known to contain both collagen and fibronectin (and it is likely to contain other proteins)[32]. Surprisingly the extracellular matrix was found to move at speeds similar to those of the cells of the adjacent epiblast[32]. Due to this fact it seems unlikely that epiblast cells can get traction from the extracellular matrix during the cell flows resulting in the formation of the streak[4]. A further implication of this is that epiblast cells should get traction from each other in order to execute the cell flows or alternatively that the extracellular matrix is responsible of the motion of the epiblast, although it is difficult to imagine how this would work[33]. In case the extracellular matrix is a passive component of the embryo it is evident that the rearrangement of the epiblast cells is responsible of the observed cell movement that gives a rise to the primitive streak.

An open question is which of the hypothetical tissue deformation mechanisms described in this section or any combination of these mechanisms is causing the observed vortical cell flows in the epiblast of the chick embryo. In addition, some cell behaviours presumable occur actively and others passively as a result of the actively driven behaviours. In this case it is an interesting question which of behaviours are active and which are passive? To observe what occurs in the tissue at the level of individual cells an imaging method is needed that is capable of imaging large tissue sections in the embryo. In addition, the resolution of the imaging must be detailed enough to capture individual cell behaviours. Imaging of cell outlines would enable accurate determination

of which cells are neighbours. Light sheet microscopy is a highly suitable technique to achieve excellent imaging of large tissue sections at cellular resolution. An overview of this technique is given in the next section.

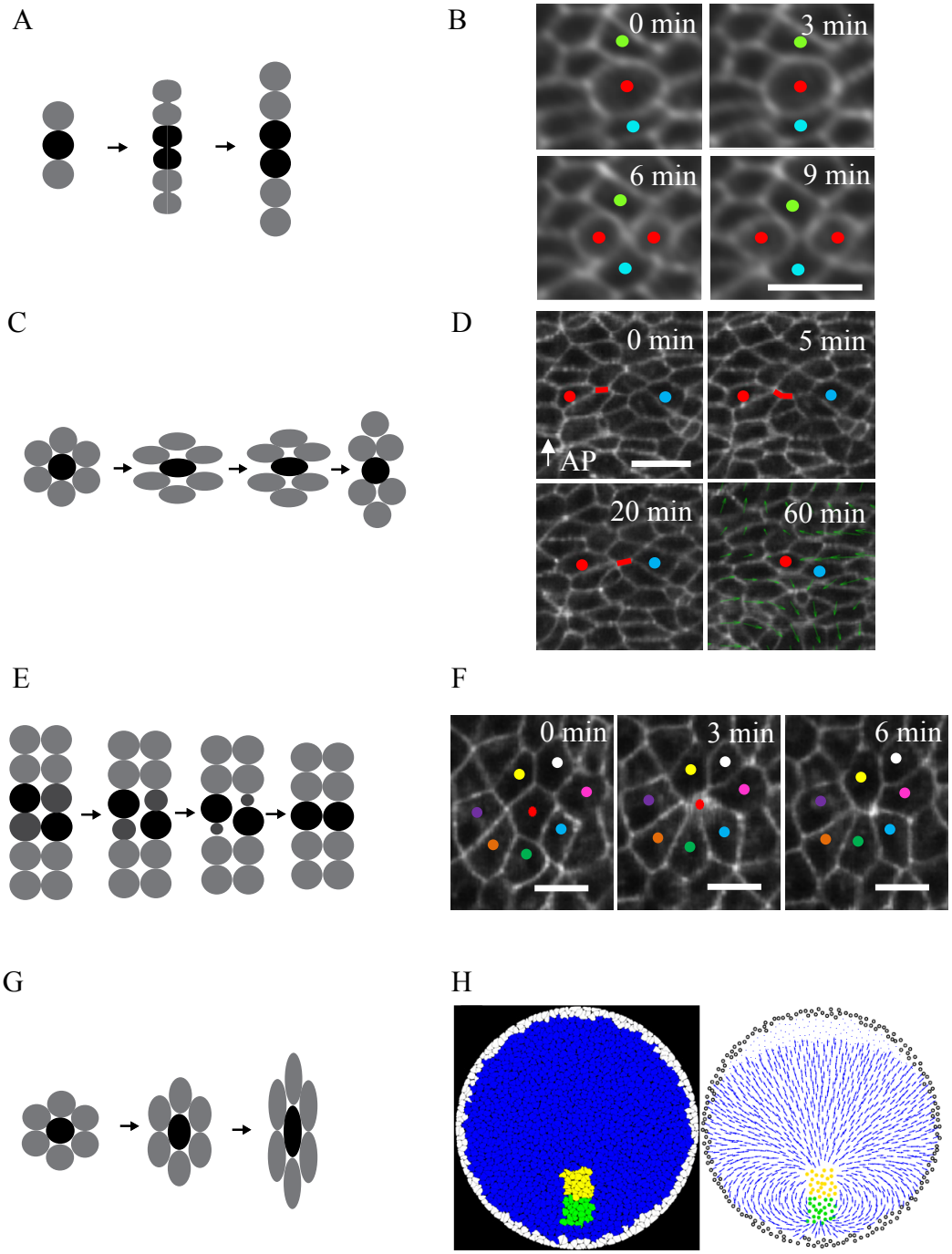

Figure 1.4 Hypothetical mechanisms of primitive streak formation. A) Oriented cell divisions could elongate tissue in direction of division axis. **B)** A cell division in chicken embryo. **C)** Cell-cell intercalation could drive expansion of tissue in a certain direction and contract tissue perpendicular to that. **D)** Example of several intercalations in chicken epiblast. Red line segments illustrate individual contracting junctions. **E)** Local ingression of cells could contract tissue. **F)** An example of ingression event in chicken epiblast. **G)** Cell shape changes may deform tissue. **H)** Chemotactic attractant cells (green) pull cells from the lateral positions to the midline of the embryo whilst chemotactic repellent cells (yellow) push cells away from the midline. This causes surrounding cells (blue) to move as two vortical flows (right panel) (adapted from[34]). The white scale bar is 25 μm.

1.3 Light sheet microscopy enables investigation of large tissue samples with fine resolution

In epifluorescence microscopes and in conventional wide-field microscopy the sample is illuminated and imaged using a same objective[35]. Light sheet fluorescence microscopes have two main optical paths, one for illumination and another for collecting the light from the object to form an image[35] (Figure 1.5). Light from the excitation path illuminates the sample from the side. The detection path has an objective, a spectral filter, a tube lens and a camera. The spectral filter rejects the excitation light[36]. Only a thin volume of the sample, the section that is going to be imaged, is illuminated by the light from the excitation path resulting in minimal photo toxicity and photobleaching of the sample[35]. This is one of the major advantages of light sheet microscopy[37]. Three dimensional imaging is achieved with light sheet microscope by moving the sample through the light sheet (or vice versa) to collect multiple images. Such three dimensional imaging exposes the sample to considerable less energy during the whole imaging process than conventional microscopy or confocal microscopy[38]. It also results in faster imaging since imaging of a section is generally performed by a camera and not by a point detector[39].

Two methods exist for generating the light sheet. In the first method a single plane is illuminated using cylindrical lens for the light sheet generation[39]. This method is called Selective Plane Illumination Microscopy (SPIM). It generates a light sheet that can be directly imaged by the camera. The other method is Digital Scanned laser Light sheet fluorescence Microscopy (DSLM)[39]. In this method a light sheet is generated by rapidly scanning a focused light beam to generate a light sheet. Advantages of the DSLM are that it generates less artefacts than SPIM and that structured illumination can be achieved[40]. A disadvantage of DSLM is that imaging is potentially slower as the light sheet is generated by scanning[35]. In addition to these basic methods, further

developments of the light sheet microscopy include different beam shaping methods (Bessel beams and Airy beams) and application of two photon excitation[41, 42]. With advanced beam shaping methods the uniformity of the light sheet, along the axial direction can be increased which provides an extended focus[42]. A disadvantage for using the Bessel and Airy beams is that a deconvolution of images has to be performed, to remove the effects of the illumination sidelobes, which can be time consuming[42]. Elimination of the effect of non-focus light (side lobes) produces sharper images although the image may suffer from artefacts like ringing and striping. Multiphoton beams enable suppression of the side lobes as well as potentially deeper tissue penetration, however multiphoton microscopy requires a higher light radiation exposure[41].

An advantage of the light sheet microscopy is that high spatiotemporal resolution can be reached which enables imaging of whole organisms in 3D[43, 44]. Light sheet microscopy has been successfully used for imaging whole zebrafish and Drosophila embryos in 3D during the development[43, 45-47]. Imaging whole organism with high spatiotemporal resolution implies increased amount of image data per experiment[48]. The data set size increases due to ability to image large three dimensional samples with high resolution along all three spatial axes as well as due to very good temporal resolution[48]. A typical data set often exceeds several terabytes and this creates considerable challenges to the image analysis, feature extraction and data storage[48].

Light sheet microscopy has not previously been applied to imaging of chick embryos. An open question is how to take advantage of this imaging technique in order achieve sufficient spatiotemporal resolution when imaging primitive streak formation in the chick embryo? More specifically, how to image the outlines of all the individual epiblast cells in order to draw conclusions of cell behaviours driving streak formation?

To further analyse cell behaviours from the obtained image data, automatic methods are required. An overview of such methods is given in the following section.

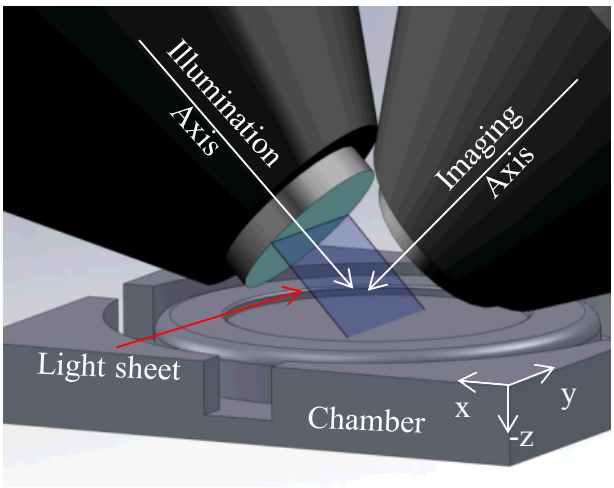

Figure 1.5 Principle of light sheet microscopy. Sample is places onto chamber and illuminated with the light sheet. Imaging axis is perpendicular to the illumination axis. Sample is moved (in direction of x-axis) to collect a three dimensional image volume.

1.4 Cell tracking and segmentation

Advances in microscopy, notably in the light sheet microscopy, have enabled acquisition of high resolution time lapse image sequences with three spatial dimensions covering potentially the whole organism[49]. With these new several terabytes sized data sets, image analysis has become a bottleneck and efforts are required to develop automatic analysis methods[49, 50]. Extracting the detailed position, shape, size and neighbourhood information of individual cells from these embryo wide image data is crucial for answering key questions in developmental biology[48, 51]. These questions involve understanding the mechanisms of cell differentiation, cell proliferation, cell-cell intercalation, migration of cells and ingression of cells[49]. The ability to track and to segment cells also enables comparison between normal and perturbed conditions of development[52]. Typically embryo wide experiments contain 10,000-100,000 cells[49]. Manual tracking and segmentation of such vast data sets is unfeasible and thus robust, efficient and reliable automatic image analyses methods are required gain further insight to developmental processes[49].

Challenges of automatic cell tracking and segmentation are variable image quality, varying density of cells and occasionally obscured boundaries between cells[49]. The cell density may be varying due to cell divisions, cell ingressions or due to difficulty of imaging the same z-plane accurately over time[49]. Several automated tools have been developed to assist with the tracking and segmentation problems but these tools are often not generic enough to be easily applied to a new context[53].

Image data used for cell tracking typically includes a nuclear marker, a cell membrane marker or a combination of these two[54]. Tracking using only a membrane marker is considered more challenging than use of the nuclear marker[54]. The cell tracking task may be split into two processes, cell segmentation and tracking. The cell segmentation covers the spatial aspect, in which the image gets shared into segments representing different features (cells)[49]. The cell tracking is the temporal aspects in which the two or three dimensional segments representing cells in successive images are linked to form tracks of cells[49]. These two aspects of the cell tracking are reviewed in following two subsections.

1.4.1 Segmentation techniques

Prior to cell segmentation specific pre-processing steps are often required to prepare the image for segmentation. These pre-processing steps include noise reduction, correction of inhomogeneous illumination, stitching of images and fusing z-slices into one 2D image[48]. After the pre-processing the actual segmentation is performed. The simplest image segmentation technique is image thresholding[50]. In this technique the pixels with intensity value over a certain fixed threshold form a foreground and rest of the pixels form a background[50]. This technique is error prone under varying image conditions (like noise), photobleaching, auto fluorescence or locally varying intensities[55]. A second, more advanced segmentation technique is to fit cell models to the image data[56]. In this

technique predetermined intensity templates are fitted to the shape and intensity profiles of the cells in the image data. This technique works well if cells have relatively uniform shapes and intensity profiles. On contrast the model fitting is likely to fail if cells display a varying morphology[49].

A popular technique for the cell segmentation is the watershed transform[49]. In this technique the image is considered as an intensity landscape. The idea is that the image forms a landscape of 'ridges' and 'valleys' and this is utilised to achieve segmentation by filling the landscape from the 'valleys' with water and checking where the 'water' meets the segment boundaries[57]. Problems of this technique are sensitivity to noise and fragmented segmentation result (oversegmentation)[49]. With appropriate postprocessing and preprocessing this technique is usable in many instances[49]. The watershed segmentation approach may be used for segmenting individual cells or tissue with tightly packed cells[58, 59]. If a nuclear marker is used for the segmentation or cells are loosely packed, the image data is first thresholded to define the foreground and background intensity levels[60, 61]. Only the foreground is then segmented to capture shapes of nuclei. Both two and three dimensional image data may be segmented using this technique[60, 62]. Alternative formulations of the watershed segmentation algorithm exist to handle discontinuous cells boundaries[63]. In case of a membrane marker initial thresholding of the image is not required as the local image features (like local minima) are used as segmentation seed points[54]. The tendency of oversegmentation may be utilised as an advantage to generate multiple sets of voxels representing parts of cells[58]. These sets are typically called supervoxels. Furthermore, a hierarchical tree structure may be established amongst the supervoxels and this structure may then be used when merging the supervoxels into segments representing cells[60, 64]. Additionally, the hierarchical supervoxel structure may be used in the cell tracking (described in next subsection) [64]. Finally, membrane segmentation may be achieved by using nuclei as

seed points for the membrane segmentation[63]. Most of the segmentation algorithms are using the nuclei instead of cell membranes to establish whether a part of an image should form a segment representing a cell or no[54].

The fourth category of segmentation algorithms is comprised of deformable models[49]. The definition of the deformable model is either explicit (active contours) or implicit (level sets)[65]. Explicit models are normally used in two dimensional applications and the implicit methods can have any dimension[49]. Active contour methods require a coarse initial segmentation as a starting point which then is refined by the method[66]. Level set based methods can segment multiple non connected segments simultaneously[49]. All the deformable models operate by minimising an energy functional which causes evolution of the segment boundary to converge around a desired structure in the image[67-69]. The energy functional is composed of two types of terms, image related terms and image independent terms[70]. The dependent terms are used take into account image based features like intensity, texture and intensity gradients. The image independent terms are responsible of shape features like curvature, surface area and length of the boundary[71]. The deformable model segmentation techniques tend under segmentation the image data[49]. Level set based methods can be used in tracking and in detection of cell divisions (described in more detail in next subsection)[65]. Finally, gradient flow based method can be used to segment nuclei[72]. In this technique local image gradient fields are used to find local points to which the field is converging (sink)[72]. A segment is then formed by tracing back all the pixels in the image that converged into the local sink. In this project we have used watershed segmentation based approach to segment outlines of cells from 2D time-lapse image sequences. The reasoning behind this choice is presented in discussion the chapter (see subsection 6.2.2).

1.4.2 Tracking techniques and applications

The next step in the cell segmentation and tracking pipeline is to connect the obtained segments temporarily to achieve tracking of cells[49]. The simplest approach, to achieve tracking of cells is to connect the segments to the closest segments in the following time frame[73]. This tracking approach works only if absolute and relative motions of the cells are sufficiently small (less than half of cell diameter).[49] Tracking of sparsely spaced individual particles is easier but this does not often yield enough information about the system that is being studied[73]. In epithelial sheets all the cells are tightly packed and tracking of objects that are next to each other is necessary[54, 74].

The level set technique described in previous subsection may be used achieve tracking in addition to the segmentation of cells[65]. This is possible as the dimensionality of the technique is not limited. The tracking aspect is achieved by placing the segment of the current time point over the image of the following time point and by evolving the level set boundary using the energy functional based on the new image data[65]. The same technique then allows detection of cell lineage branching as the evolved level set boundary will split into different boundaries[65]. A disadvantage of this technique is that the displacement of locations of cells between two consecutive time points are assumed to be relatively small (less than half cell diameter)[65]. In addition, level set techniques are slow when tracking order of 10,000 or more cells[64].

Particle image velocimetry may be utilised to connect segmentation of two consecutive time points[46]. In this technique local image features are correlated with a local neighbourhood in the subsequent image[49]. This technique may be further improved by first sharing image into supervoxels (described in previous subsection) representing local features then evaluating the deformation between consecutive frames of the image sequence using the supervoxels[74]. An interesting extension of this technique is to

establish a hierarchy between the supervoxels, that is to find which supervoxels should be merged first in case an oversegmentation has occurred[64]. Furthermore, a Gaussian mixture model is used to merge the over-segmented segments and to find the most probable matching segment from the subsequent time point in order to achieve tracking of cells[64]. Use of the supervoxels and GPU based computations greatly reduced the time required for tracking using Gaussian mixture model[64].

Finally, to achieve temporally consistent segmentation global methods may be used[73]. In this technique particles are first segmented and then the particles are linked into initial tracks. This is followed by a process of merging and splitting the obtained tracks in order to gain more consistent and correct final tracking result[73]. Both of the tracking steps are formulated as linear assignment problems and solved using heuristic techniques to achieve near globally optimal solution[73]. A more recent technique extends the previous approach by utilising hierarchical supervoxels obtained by oversegmentation[60]. A global optimisation was then performed to find a solution to a formulation (joint segmentation graphical model) connecting all spatiotemporal supervoxels into tracks of cells[60]. A probabilistic classifier was included into the formulation of tracking problem to achieve automatic cell division detection, that is to connect mother and daughter cells temporally[60]. Other techniques reported for the cell division detection included automatic monitoring of the shape of the nucleus, automatic detection of specific features associated with cell division such as intensity change and manual division annotation as part of the automatic tracking[46, 62-64, 75, 76]. In this project we have used PIV based technique to achieve tracking of cells. The reasoning behind this choice is presented in the discussion chapter (see subsection 6.2.2).

Several techniques have been developed to quantitatively analyse cell behaviours using the automatically (or manually) obtained cell tracking and segmentation data[24, 77]. These

techniques achieve continuous spatiotemporal dissection and quantification of tissue deformation, cell intercalation and local cell shape changes[24, 77]. With the quantitative techniques detailed information about morphogenetic processes of zebrafish and Drosophila development have been achieved[24, 78, 79]. Automatic tracking of cells is becoming an increasingly popular technique and it has been used in several recent studies to investigate development of Drosophila and zebrafish[24, 60, 62-64, 71, 79-81]. Automatic cell tracking has not been used to obtain quantitative information of all the cells in epiblast of chicken embryo. An open question is how to achieve reliable and robust segmentation and tracking of cells in the chick epiblast during the formation of the primitive streak? Furthermore, how to achieve this using cell membrane marker in absence of nuclei and mitotic markers? A major biological question is how to utilise the segmentation and tracking information to quantitatively understand which combination of cell behaviours is responsible for the tissue deformation driving primitive streak formation during gastrulation?

2 AUTOMATIC TRACKING ALGORITHM FOR FOLLOWING CELLS IN EPITHELIAL SHEETS

The epithelial sheets of interest in our study contain ~100,000 cells as detailed in the previous chapter. Due to the vast number of cells it is important to able to track cells in an automatic manner. This chapter describes the details of an automatic tracking algorithm that is used to segmentation and track cells in the chick epiblast. In this study segmentation is a process in which image shared into segments (sets of pixels) representing cells.

The tracking algorithm itself is outlined in detail in section 2.1. This is followed by introduction of a variant of the tracking algorithm used for manual validation of the tracking data (section 2.2). Finally, the manually validated data is used to evaluate the correctness of the tracking algorithm (section 2.3). In addition the performance of the tracking algorithm is measured in the same section.

2.1 Automatic tracking algorithm

The automatic tracking algorithm operates on a time lapse sequence of 2D sections of the apical chicken epiblast. The next subsection (subsection 2.1.1) describes main idea of the automatic tracking algorithm and the following subsections describe details of the algorithm.

2.1.1 Key idea of the automatic tracking algorithm

Goal of the automatic tracking algorithm is to track cell centroids over time, to detect cell divisions, to detect ingressing cells and to identify outlines of each cell in each time point. Volumetric time lapse sequences were imaged using a light sheet microscope. Details of the used microscope and data handling are described in section 4.1 of the computational methods chapter. The tracking algorithm operates on 2D time lapse

sequences of outlines of cells. In our study a 2D time lapse sequence is obtained from a volumetric time lapse sequence by first identifying the apical surface of epiblast of the chick embryo. The surface is then projected on a plane to obtain a 2D image. This process is then repeated independently for all desired time points. The procedure of surface projection is described in detail in computational methods chapter in section 4.2. In some experiments the embryo was imaged in two complementary halves by imaging both sides sequentially. In these instances the surface projection data sets were stitched together using method described in the methods chapter in section 4.3.

The automatic tracking algorithm starts by segmenting the first image of the 2D time lapse sequence (Figure 2.1). In this process the image is divided into sets of pixels representing cells. The sets are called segments. The first segmentation does not use prior information about the locations of the cells and is called time independent segmentation. Details of this segmentation are given in subsection 2.1.2. Each segment in the first segmentation initiates a track of cell (Figure 2.1). These tracks are then used to initialise a tracking structure. The structure is used for storing cell centroids, cell neighbourhood relations, temporal connectivity of cell centroids and information about cell lineages. Details of the data structure are given in subsection 2.1.5.

After the first segmentation and initialisation of the data structure the automatic tracking algorithm will proceed in a sequential manner through all the remaining time points. This is illustrated by loop in the flow chart of the figure 2.1. The first step in the loop is to evaluate the local tissue flow between the previously segmented image and the subsequent image (time points t and t+1). As tissue is deforming locally over two consecutive time points and field of view is large it is not sufficient to use rigid registration. Instead, a particle image velocimetry based tissue velocity field is evaluated between two consecutive time points (t and t+1). The resolution of this tissue

displacement field is similar to the average diameter of cells. This guarantees that individual cells can be tracked correctly. Details of this method are described in computational methods chapter in section 4.4.

A

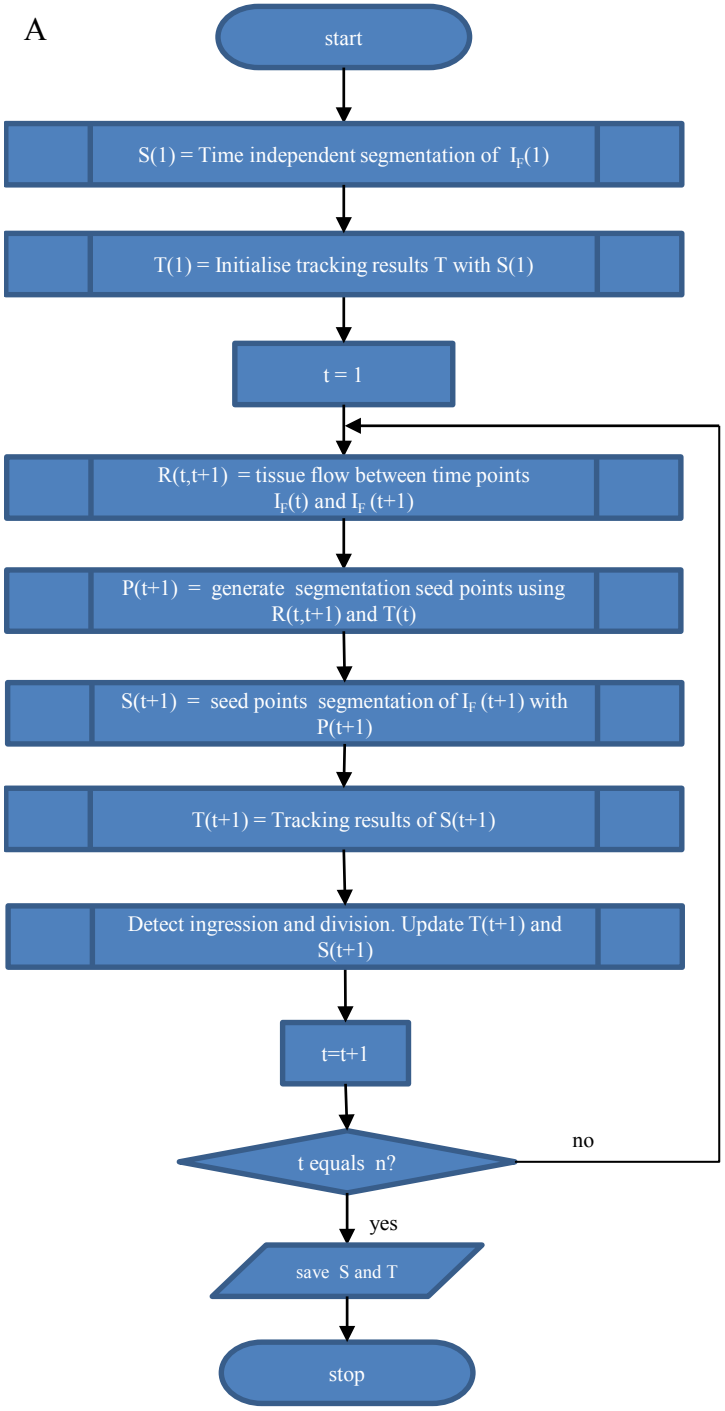

B **VARIABLES**

description	symbol	interval
number of images	n	N/A
filtered images	$I_F(t)$	t=1,2,…,n
segmentation	S(t)	t=1,2,…,n
tracking results	T(t)	t=1,2,…,n
registration	R(t,t+1)	t=1,2,…,n-1
seed points	P(t)	t=1,2,…,n

C **LEGEND**

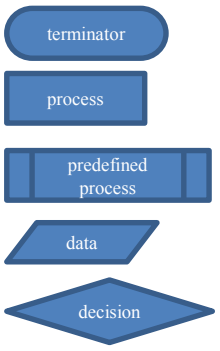

Figure 2.1 Flow chart of outline of automatic tracking algorithm. A) The tracking algorithm starts by time independent segmentation of first time point. Subsequent time points are tracked and segmented in a sequential manner. New cell segmentation is achieved by utilising current segment centroids and registration between two consecutive time points. Ingression and division events are detected from the new segmentation. **B)** Variables used in A are detailed in this table. **C)** Legend for different types of flow chart symbols.

The tissue velocity field between the consecutive time points (t and t+1) is then used together with previously identified cell centroids (in time point t) to predict which are new centroid locations of the cells (in time point t+1) (Figure 2.1). Shapes of previously segmented cells (time t) together with the predicted new locations of cells in time point t+1 are used to generate seed points for the segmentation. These seed points are then used to segment the image of time point t+1. This will guarantee that number of segments is preserved over two consecutive time points. New segments of cells (in time point t+1) are then used to calculate new centroid locations and these are then used to refine the initial estimate of the cell's location. This cell centroid based segmentation method is described in detail in subsection 2.1.3. After the segmentation the track data structure is updated with new cell outlines and centroids (Figure 2.1).

The procedure described above guarantees that number of cells is conserved over two consecutive time points. In epithelial tissue number of cells may not stay constant as cells divide and ingress. In the automatic tracking algorithm cell divisions and ingressions are detected by comparing segmentation of two consecutive time points (time points t and t+1, see subsection 2.1.4). If a cell is detected to ingress it is removed from the tracking structure. Similarly, if cell is detected to divide its track is connected to two newly induced daughter cells (for details of this procedure see subsection 2.1.4). After changes in the number of cells are made a new time point is processed (Figure 2.1). Finally, the tracking structure and all the cell segmentations are saved to be used for further analysis. The tracking algorithm is implemented in Matlab scripting language. A short description of Matlab is given in computational methods chapter in section 4.5.

2.1.2 Time independent cell segmentation

As described in previous section the tracking algorithm segments the image of the first time point without prior tracking information about cell locations. Prior to segmentation the image is filtered with a bandpass filter in ImageJ with following settings: large structures down to 20 pixels, small structures up to 1 pixel and automatic saturation. This is followed by smoothing of the images with a Gaussian filter (radius of 1 pixel). The bit depth of the images is 8. For more details about ImageJ see section 4.6 in the computational method chapter.

After the filtering the image is segmented. To segment the filtered image local minima with height less than 10 are suppressed. This is followed by watershed segmentation of the image. As a result each remaining local minima in the suppressed image forms a segment (set of pixels) around of it. An example of suppressed local minima and corresponding watershed segmentation is illustrated in panels B and C of figure 2.2, respectively. These image processing steps are implemented in Matlab (see section 4.5).

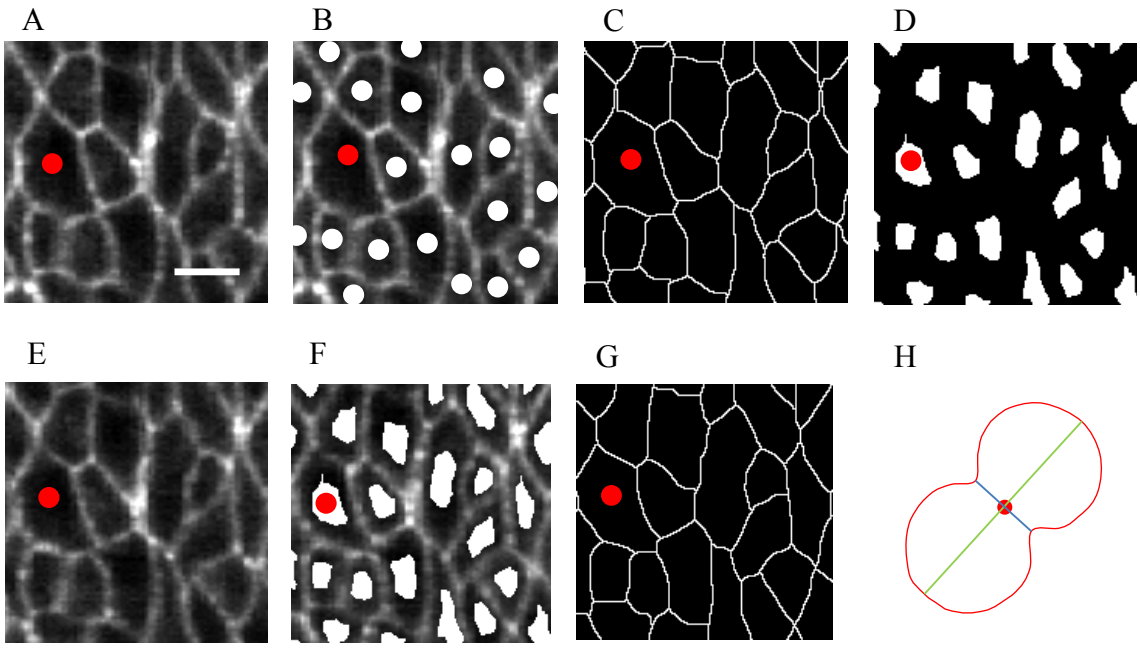

Figure 2.2 Outline of the automatic tracking algorithm. A) Raw image of cell membranes in the first time frame. **B)** Segmentation of the image A is obtained by using local grey value minima (white blobs) as seed points for watershed segmentation algorithm. **C)** Segmentation of the image A. Outlines of cells (white lines) are found by the segmentation algorithm and saved as a binary image. **D)** Seed points for segmentation of the second time point are obtained by shrinking segments of the image C. In addition, registration between the two time points is utilised to tracking and correct positions of segments. **E)** Image of cell membranes of the second time frame. The tracking algorithm aims to track cells between images A and E. Throughout this figure location of a cell is marked with red blob. **F)** New seed points (D) obtained from the first image are projected over the image E using tissue velocity field. **G)** Segmentation of the image E is obtained using the seed points of the image F. **H)** Outline of a diving cell shown as red. Green and blue lines are long axis and short axis of dividing cell, respectively. The white scale bar is 10 μm.

2.1.3 Segmentation using cell centroids

After the segmentation of the first time point rest of the time points are segmented in a sequential manner using the previous segmentation and tissue velocity field between two consecutive time points (t and t+1). The first step in this process is to consider each segment in the current segmentation (Figure 2.2 C). These segments are then shrunk to 40% of their original size. The seed point is chosen to be bigger than just a single pixel to increase likelihood of capturing the local image minima within the cell. The initial centroids of these shrunk segments are the same as the centroids of the original

segments (Figure 2.2 D). The shrunk segments are used as segmentation seed points for the time point t+1 (Figure 2.2 E). To compensate for local drifts in the tissue the shrunk segments are then positioned over the time point t+1 displaced by a certain distance calculated from the tissue velocity field (Figure 2.2 F). In this process the tissue velocity field is used to estimate a displacement vector for each segment centroid independently. Once the seed points are determined, the image of time t+1 is segmented in same manner as in time independent segmentation (Figure 2.2 G and subsection 2.1.2). The cell centroid locations are then computed from the new segmentation and the initial estimates of locations of cells are updated with the new centroid locations. This segmentation scheme achieves simultaneously tracking and segmentation. In addition the number of segments is guaranteed to be conserved over time.

A problem of this type of segmentation is that cells flow into the field of view being imaged. These cells do not get correctly segmented as number of segments is conserved. An example of this problem is illustrated in panels A and B of figure 2.3 where cells are flowing into field of view from the bottom boundary. To deal with this problem, PIV based tissue velocity fields are used to identify which parts of the boundaries have flowed in. This is done by placing a densely sampled polygon on the boundary of the image (red line in Figure 2.3 A). Each vertex point of this polygon is then displaced with the velocity field to obtain a deformed polygon (red line in Figure 2.3 B). To find out which cells have flowed in, a time independent segmentation is performed for the image region that is outside of the deformed polygon (Figure 2.3 C and subsection 2.1.2). Furthermore, all segment centroids that are outside of the deformed polygon are used as additional seed points for the segmentation of the following time point (black dots in Figure 2.3 D). An example of such segmentation is shown in panel E of figure 2.3. This method guarantees correct segmentation of inflowed cells regardless of magnitude of inflow velocity of tissue (see figure 2.3 F for a comparison). The

reasoning why the watershed segmentation and PIV based tracking algorithm was developed is provided as part of the discussion chapter (see subsection 6.2.2).

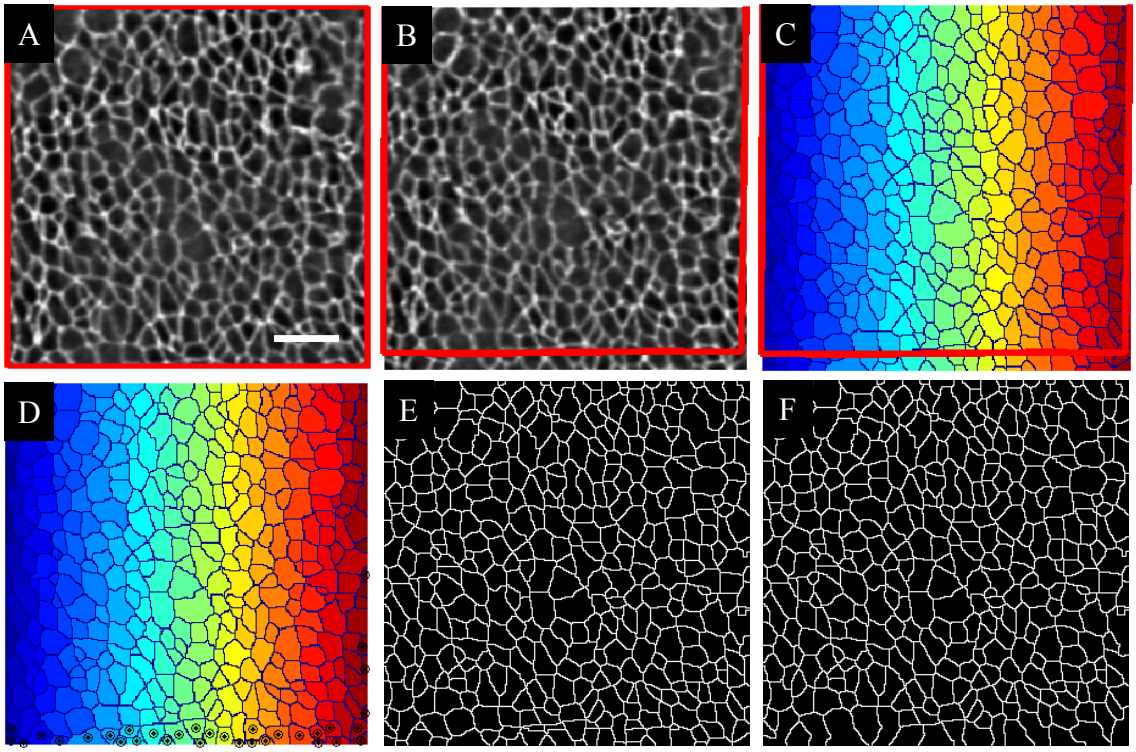

Figure 2.3 Automatic tracking of cells that flow into field of view. A) Raw image of cell outlines of first time point. **B)** Raw image of cell outlines of second time point. Particle Image Velocimetry (PIV) velocity field is used to determine how boundary of field of view (red outline in A) deforms between images of panels A and B. Red line in panel B shows that inflow has occurred from outside in the lower part of the image. **C)** To segment these new cells correctly, time independent segmentation is performed. **D)** Black circles mark cells that were detected to be outside the red inflow boundary in panel C. **E)** The detected new cells are used together with already existing cells to segment the new time point (panel B). **F)** Segmentation of panel B without adding new cells to the segmentation. The white scale bar is 40 μm.

2.1.4 Cell division and ingression detection

The automatic tracking algorithm conserves to number of tracked cells over time as shown in previous subsections. As number of cells is not conserved in ingression and cell division events these cell behaviours need to be detected separately. Ingressing cells are detected using two criteria. Firstly, if a cell after segmentation has only two neighbours it is considered to ingress. Secondly, if area of a cell after segmentation has a smaller area than a certain threshold (150/magnification in this study [an area much

smaller than an average cell]) the cell is marked as ingressing cell. Reliable segmentation of cells smaller than this was found difficult in practice. Once a cell has been marked as an ingressed cell in the tracking data structure it is no longer considered as a new seed point in the following segmentations.

Cell divisions are detected by first considering how long time a cell has been tracked. The track of a cell has to be longer than a threshold (5 h in this study). If track of a cell starts from the first time point the cell is allowed to divide at any time starting from the second time point. Similarly, if a cell has flowed into field of view the cell may divide at any time. In case a cell meets the listed requirements of shape and cross sectional area of the cell are considered. Length and width of the cell is measured along major axis and minor axis of an ellipse that is fitted to the shape of the cell, respectively (Figure 2.2 H). If the length is 2.5 times longer than the width, the area is greater than a threshold (in this study 2500/magnification [an approximate area of a dividing cell]) and the area is smaller than a threshold (in this study 25000/magnification [area that is significantly larger than a dividing cell]), the cell is tested for a cell division.

To test if the cell should divide further checks are made. Firstly the cell is segmented into two daughter cell candidates. The time independent segmentation is used for this by inserting two seed points onto major axis of an ellipse fitted to the shape of the cell (see subsection 2.1.2 for details). Both seed points are one fourth of the cell's length from cell's centroid. After the segmentation of the daughter cell candidate segments are quantified to test whether the mother cell should divide. The cross sectional area of a larger daughter cell may not be more than 50% greater than cross sectional area of smaller daughter cell. This guarantees that daughter cell candidates have a similar size. Eccentricities of both daughter cell candidate segments must be below 0.7. This guarantees that daughter cells are not too elliptic. In addition, the average pixel intensity

on the newly created segment boundary between new daughter cells must be greater than the average pixel intensity within the mother cell. This guarantees that a new cell junction is forming between the daughter cells. If all these conditions are met the cell is marked to divide in the tracking structure.

2.1.5 Data structure of tracking data

The automatic tracking algorithm stores cell based tracking data into a data structure that is organised in such a way that the tracking data of each individual is stored as an individual data entry. The data storage is implemented as a Matlab structure array. Each element in the structure array has fields for storing all the following information about a cell: time indices, centroid location, fitted ellipse parameters, perimeter and list of neighbours (Table 2.1). All of these four fields contain information for every time point in which the cell is present. In addition information of where the track started and finished are stored. Each cell has its own unique index in the tracking structure. These indices are used to store the neighbouring cells in the tracking structure. Additionally, the cell indices are used for marking the mother-daughter cell relations (Table 2.1). Cell lineages may be constructed using these stored indices.

description	attribute	size
Number of time points in track	n	scalar
Time point index	t	1 x n
Centroid location [pixel]	cent	n x 2
Fitted ellipse parameters (major axis [pixel], minor axis [pixel], orientation of major axis [degrees])	ellipse	n x 3
Perimeter of cell [pixel]	perim	1 x n
Index of mother cell. -1 if cell exists in first time point. -42 if cell flows into field of view.	birth	scalar
Cell termination status. 0 if cell still exists. -1 if cell ingressed. -3 if cell divided.	death	scalar
Indices of daughter cells. Zeros if no daughters.	daughters	1 x 2
A structure for storing neighbouring cells. Each element contains a set of indices of neighbouring cells at the time point.	neighs	1 x n

Table 2.1 Data structure of a track of a cell.

2.1.6 Embryo wide cell tracking example

The automatic tracking algorithm described in this section can be used to track large numbers of packed epithelial cells over periods of time that are relevant for analysing cell behaviours during early gastrulation of chicken embryo. An example such a tracking result is shown in figure 2.4. The figure illustrates clearly vortical tissue flows during formation of the primitive streak as cells are moving to the midline to the site of forming primitive streak.

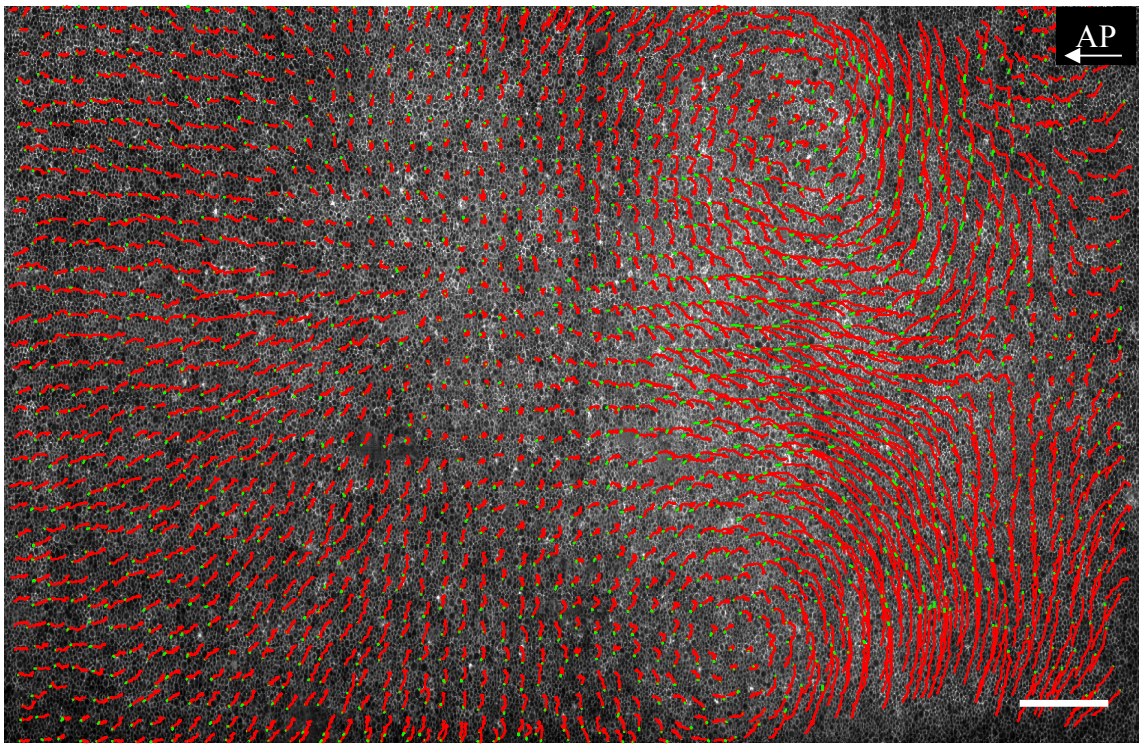

Figure 2.4 cell tracks of epiblast cell flows obtained using the tracking algorithm. Each red line segment represents the track of a cell over a 2.5 h period. The green lines show the positions of cells over the last 15 min. For clarity only 5% of all the tracks are shown in this presentation. The white scale bar is 200 μm.

2.2 Collection of ground truth tracking and segmentation data

To validate tracking quality of the automatic tracking algorithm described in previous section it is important to collect ground truth data sets. To do this I implemented a semi-automatic tracking algorithm which works similarly to the automatic tracking algorithm. In this algorithm the user is visually inspecting the tracking result and interactively correcting the locations of seed points in order to achieve a correct segmentation. Ingressions and cell divisions events are marked manually when necessary. The semi-automatic tracking algorithm provides all the same tracking data as the automatic tracking algorithm.

2.2.1 PIV based drift compensation of region of interest

To validate tracking result is it important to follow same set of cells from an embryo over time. It is not sufficient to follow a fixed field of view in the embryo due to tissue

flows occurring during the normal development. These local tissue flows or a drift of the whole embryo may occur along anterior-posterior or lateral directions. To cope with this problem I am using PIV tissue velocity fields to follow and cut out a desired part of the tissue over time (see more details from subsection 4.4.2). This drift compensated image sequence is then used as the input time lapse sequence for the semi-automatic tracking algorithm described in next subsection.

2.2.2 Semi-automatic tracking algorithm

In order to gather ground-truth data sets user has to manually correct the tracking result in a drift compensated image sequence. It would be fairly complicated to manually correct a fully tracked sequence as tracking errors often propagate. A better way for dealing with tracking errors is to correct them immediately after they have occurred. On the other hand it is advantageous if user does not need to deal with trivial tracking decision like linking up a centroid of a cell that did not change its position relative to its neighbours and did not considerably change its shape or size. The user will generally need to give more attention to a region with frequent cell divisions as dividing cells need to be annotated manually. In addition, cells close to dividing cells are often changing their cross sectional area due to pressure exerted by the dividing cell.

The semi-automatic tracking algorithm is similar to the automatic tracking algorithm with a few simplifications (see section 2.1). The semi-automatic tracking algorithm starts by performing a time independent segmentation of the first frame of a desired time sequence (Figure 2.5, subsection 2.1.2). Here segmentation means that image is divided into simply connected sets of pixel and segment boundaries between these pixels. The segmentation is performed with a watershed segmentation algorithm (for more details see section 4.5). The resulting cell segmentation of the first time point is shown to the user by overlaying the segment boundaries (cell outline), with the original

background image. In addition cell centroids are marked with coloured blobs. It is then task of the user to visually verify that that correct number of segments is created (no over segmentation and no under segmentation) and that cells are segmented along their outlines (Figure 2.5). If number of cells is not correct user can either add or delete segments. If cells are not correctly segmented user may modify segmentation by altering locations of the segmentation seed points (Figure 2.5). In both cases, after an action of the user, a new segmentation is calculated and shown to the user.

Once a correct segmentation of the first time point is accomplished, the user may proceed to the next time point. In this case positions of cell centroids and precomputed PIV based tissue velocity fields are used to compute new centroid positions (similar to the automatic tracking algorithm described in previous section). User is expected to cut out a large enough region from an embryo so that cells do not flow in or flow out from the selected field of view. New centroid positions are then used to compute a new segmentation in same way as described in the previous paragraph. The user may then visually inspect the new segmentation and alter number of cells or locations of the cell centroids. A cell belonging to the same track has the same colour in all the time points, which facilitates the tracking. In case of a cell division the user must manually annotate new daughter cells (Figure 2.5). Similarly, ingressing cells will be annotated separately. At any time user may save the tracking information and segmentation. This data is stored into a file that can be loaded back to the semi-automatic tracker script to continue the work. Data structure of the semi-automatic tracking algorithm is same as the one used for the automatic tracking algorithm (2.1.5). An implementation of graphical user interface of the semi-automatic tracking algorithm is described in detail in Appendix I. In addition, instructions how to use the GUI are provided.

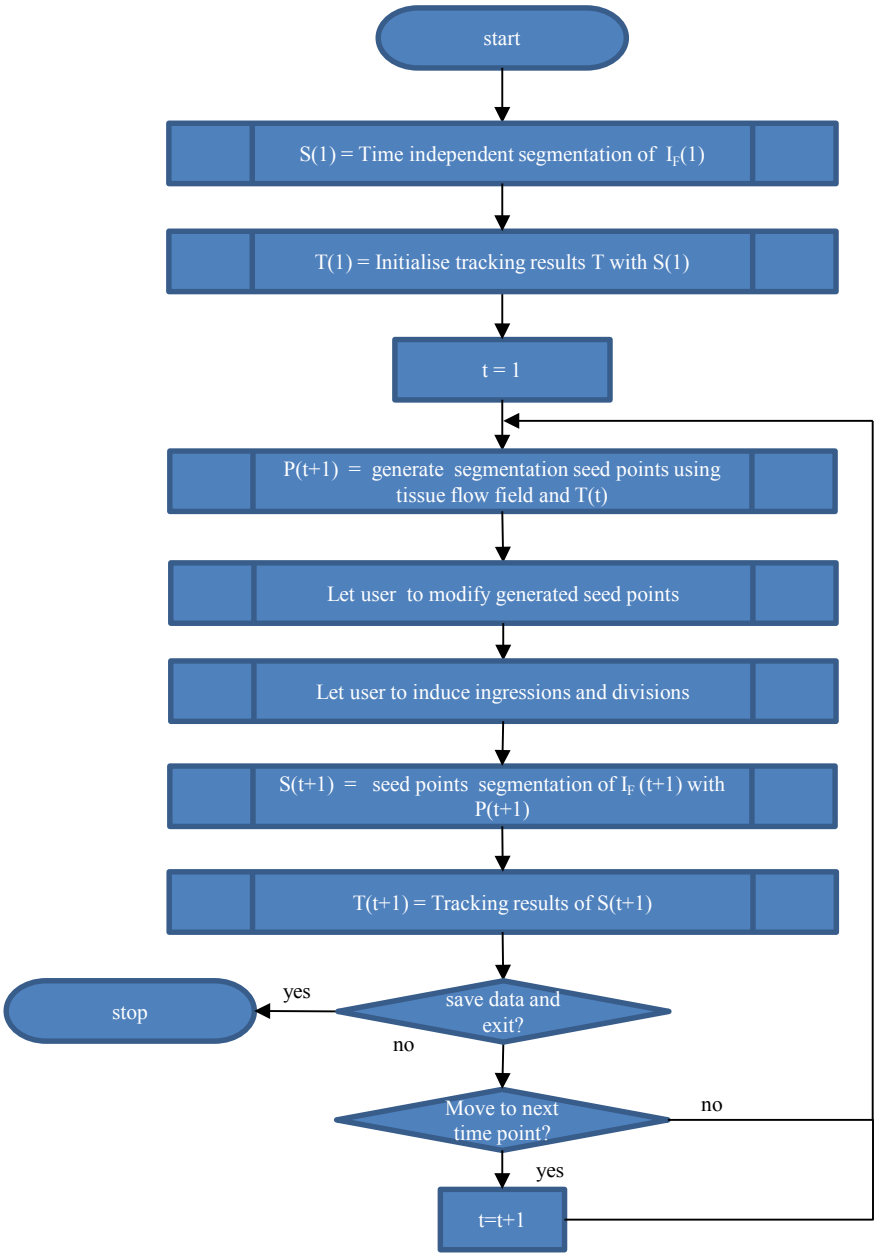

Figure 2.5 Flow chart of outline of semi-automatic tracking algorithm. The tracking algorithm starts by time independent segmentation of first time point. Subsequent time points are tracked and segmented in a sequential manner. New cell segmentation is initially achieved by utilising current segment centroids and registration between two consecutive time points. The achieved segmentation is then modified by user if needed by repositioning segmentation seed points. In addition the user has to induce division and ingression events. Once all the modifications are done for the current time point user may move to the next time point. At any time user may save the current session. Variables and flow chart symbols used here are same as in figure 2.1.

2.2.3 Semi automatically annotated domains

The semi-automatic tracking algorithm described in the previous section was used to collect manually validated tracking data. This was done by choosing four domains from

different regions of chicken epiblast while the primitive streak was forming. These regions were from the developing streak, lateral from the streak, posterior from the streak and anterior from the streak. The lateral domain was followed over period of 750 min and all the other domains were followed over period of 600 min (Figure 2.6 A). It can be seen from the initial and final positions of the domains that anterior and posterior domains stay close to their initial positions and that streak and lateral domains move towards the developing primitive streak.

Initially each of the domains consisted of a selection of cells from a square area (Figure 2.6 B-D). Cells or corresponding daughter cells in the streak domain experience interdigitation and the domain elongates along midline of the embryo while contracting perpendicular to that (Figure 2.6 B). It is also worth noting cells of this domain do not change their shape in an anisotropic manner while the domain is elongating. The anterior domain grows in size but the shape of the domain remains largely the same (Figure 2.6 C). The posterior domain elongates a small amount along the midline of the embryo, but not as much as the streak domain (Figure 2.6 D). Finally, the lateral domain experienced a similar deformation as the streak domain, but the deformation was not as pronounced as in the case of the streak domain (Figure 2.6 E).

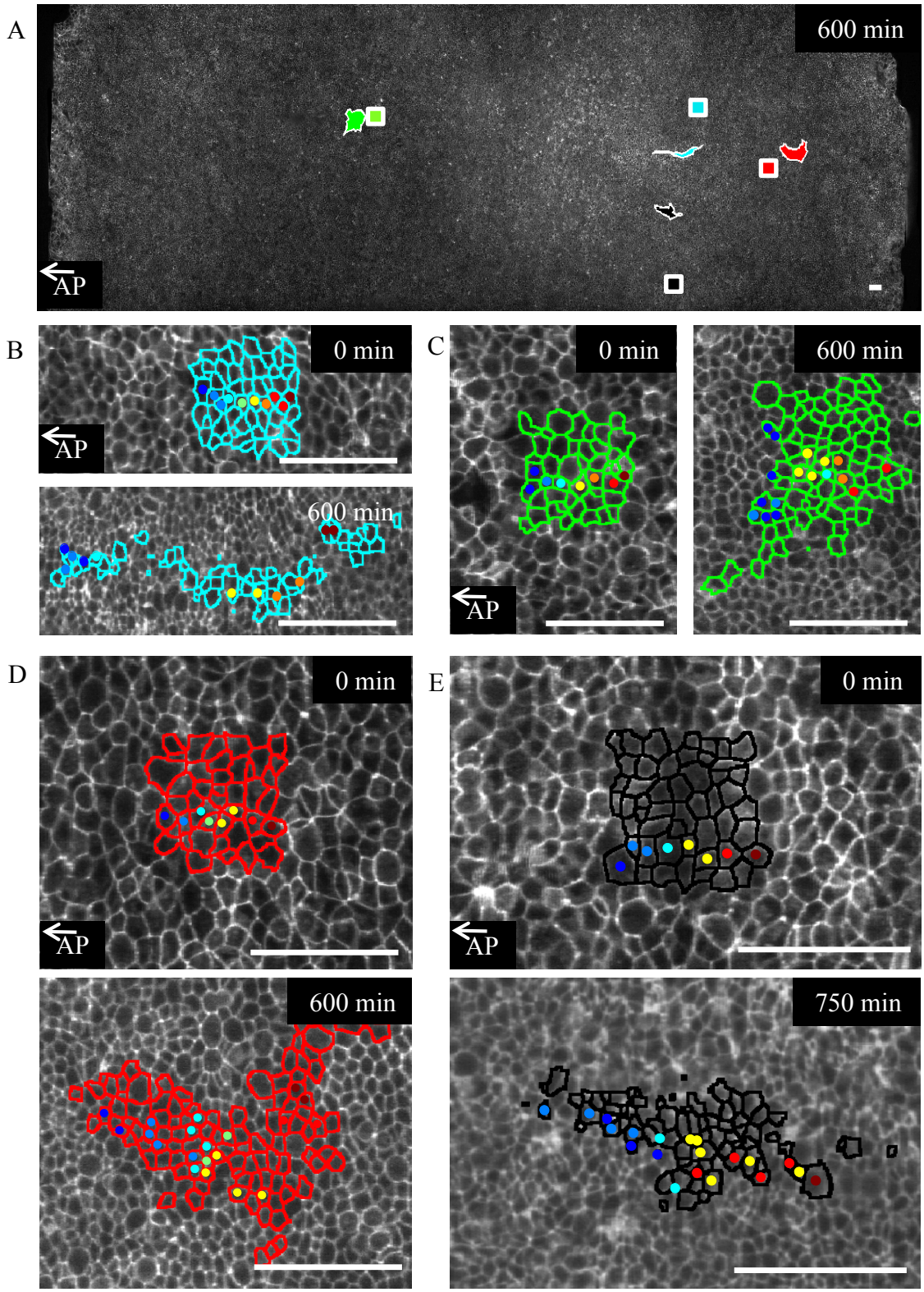

Figure 2.6 Result of semi-automatic tracking. A) Four different regions are tracked over time. Initial positions of the domains are shown as coloured squares. Final positions, 600 min later, are shown with coloured deformed polygons. **B-E)** Initial and final shapes of domains. The colours used for segmentation are same as in A. Coloured dots illustrate how individual cells and possible their daughter cells have moved over the tracking period. The white scale bars are 100 μm.

2.3 Validation and performance of the tracking algorithm

To validate correctness of the automatic tracking algorithm we performed automatic tracking of semi-automatically curated four domains described in the previous subsection. These automatically obtained cell tracks and segmentations were then compared to the semi-automatically validated tracks. All four semi-automatically annotated domains together contained 712 cell tracks. Distribution of lengths of these cell tracks were compared to the lengths of corresponding automatically obtained track lengths (Figure 2.7 A). The comparison was done from the beginning of each individual semi-automatically annotated track. For the comparison the automatic and semi-automatic track lengths were separated into bins of 30 min (Figure 2.7 A). The distributions look similar except for the first and for the second bin indicating that many tracks in the automatic segmentation are terminating prematurely briefly (within one hour) after initiation of the track. When comparing track lengths of automatically tracked cells and track lengths of the corresponding manually tracked cells it clear that many of the tracks have similar length (Figure 2.7 B). It can also be seen that some of the automatic tracks regardless to length seem to terminate prematurely (Figure 2.7 B).

Ratios between automatic track lengths and the corresponding semi-automatic track lengths were evaluated to determine what percentage of the tracks were correct (Figure 2.7 C). In this quantification track of a cell is considered to span between two consecutive cells divisions. The ratio value one was most frequent indicating that 50% of the tracks had desired length and thus the corresponding cells were correctly tracked throughout the experiment. On average, lengths of automatically obtained cell tracks were 69% from the corresponding semi-automatically annotated tracks.

Additionally, cell linkage accuracy was used to measure how correctly cell centroids between two consecutive time points were linked together. This was done separately for

all the four semi-automatically annotated domains (Figure 2.7 D). For the anterior and the posterior domains the linkage accuracy was close to the 98% throughout the time sequence. For the streak domain and the lateral domain the linkage accuracy was initially similar to the other two domains and was decreasing over time.

Finally, to measure correctness of segmentation of the automatic tracking algorithm a Dice similarity coefficient was computed between the corresponding automatic and semi-automatic segmentations [54, 82]. In this Dice measure all the time points and all the cells were compared independently. The measure was evaluated using sets of pixels of the automatic segment (pixels A) and sets of pixels of the semi-automatic segments (pixels B) in following way:

$$QS = \frac{2|A \cap B|}{|A| + |B|} \quad \textbf{(2.1)}$$

Where A and B are sets of pixels from the two segmentations. The dice coefficient ranges from perfect match (value one) to complete mismatch (zero)[82]. The similarity coefficient was evaluated for all the semi-automatically annotated domains over time (Figure 2.7 E). The Dice coefficient indicated more than 90% match for all the domains during first 300 min and after this the match between segments started to decrease over time. The anterior and posterior domains had Dice coefficient larger than 80% throughout the image sequence. In the other two domains (streak and lateral) the initially high Dice value decreased to close 60% towards the end of the sequence.

The correctness of cell division detection of the automatic tracking algorithm was verified by overlaying the detected cell division events over the image data used for the tracking automatic. This was done for regions 6000x2560 pixels in two distinct time points. One of the time points was selected prior to onset of cell flows and the other time point was selected from a time point where the cell flows had already started. Site

of the primitive streak was visible in these regions. To manually find all the cell divisions from these large regions the images were shared into small domains and three consecutive time points were viewed to the user in order to determine and annotate where cell divisions occurred. A total number of cell divisions annotated in this way were 1119. Similarly, the annotated regions contained 1140 automatically detected cell division events. The manually annotated cell divisions were then compared to the automatically detected cell divisions. The automatic tracking algorithm detected 67.4% of all the occurred cell divisions (754 out of 1119) (Figure 2.7 F). In addition, 66.1% of the automatically detected cell divisions were actual cell divisions (754 out of 1140) (Figure 2.7 F). This implies f-measure value of 0.667 used in literature to combine the detection rates thus indicating similar quality of cell division detection as achieved in case in Drosophila embryos[60].

The ingression events were validated in a different way than the cell division events due to difficulty of identifying all the ingression events from a large region of embryo. To validate the ingression detection the tracking data of the semi-automatically annotated domains were used (Figure 2.6). All the automatically obtained cell ingression events were overlaid with the semi-automatically identified ingression events and with the cell image data. These overlays were then used to determine which of the detected ingression events were correct and which were incorrect. The total number of ingression events occurring in the manually annotated domains was 92. Similarly, the total number of automatically detected ingression events was 103. Automatic tracking algorithm detected 21% of all the ingression events that occurred in the semi-automatically annotated domains (precision) (Figure 2.7 G). In addition, 18% of all the automatically detected ingression events were actual ingression events (recall) (Figure 2.7 G). This implies f-measure value of 0.19.

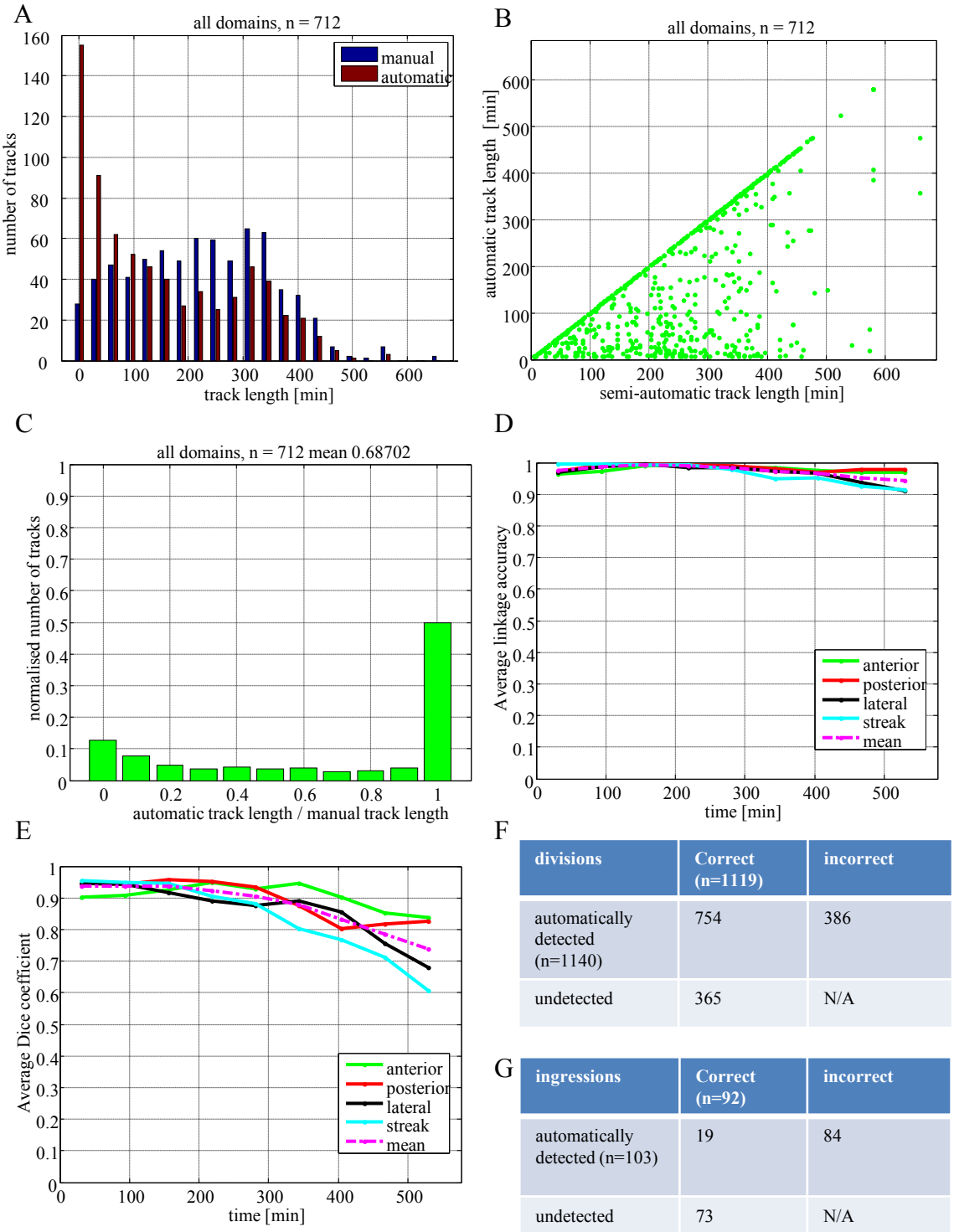

F

divisions	Correct (n=1119)	incorrect
automatically detected (n=1140)	754	386
undetected	365	N/A

G

ingressions	Correct (n=92)	incorrect
automatically detected (n=103)	19	84
undetected	73	N/A

Figure 2.7 Validation of tracking using semi-automatically annotated domains. A) Distribution of track lengths in all semi-automatically annotated domains (blue) and corresponding automatically tracked domains (red). Range of each bin is 30 min. **B)** Lengths of automatically obtained cell tracks compared to lengths of the corresponding semi-automatically obtained cell tracks. **C)** Distribution of track length ratios. Mean of the distribution is 0.687. **D)** Cell linkage accuracy in each of the four domains measured over time. **E)** Dice coefficient of cell segmentation measured in each of the four domains over time. **F)** Annotated cell divisions. **G)** Annotated ingression events.

A typical experiment consists of a 2D image sequence with resolution 8000x2560 pixels (5.2x1.7 mm) over 300 time points (16 h). The number of cells over such a region varies over time, but on average is around 60,000. The tracking algorithm requires typical around 72 h to process such a data set.

3 ANALYSIS OF TISSUE DEFORMATIONS AND CELL BEHAVIOURS DURING PRIMITIVE STREAK FORMATION IN CHICKEN EMBRYO

This chapter illustrates how the automatic tracking algorithm and the semi-automatic tracking algorithm were used to study cell behaviours during primitive streak formation in chick embryo. The main aim was to use statistical methods to quantify cell behaviours in order to answer to question which of the cell behaviours drive the vortical tissue flows and elongation of the primitive streak in the epiblast. In addition, we used PIV based methods to gain better understanding how tissue deforms and to have a different method to compare our results. We tracked epiblast cells during formation of the primitive streak and used this data to dissect various cell behaviours. This chapter starts by measuring the tissue deformation with four different methods (section 3.1). This is followed by quantification of various cell behaviours including: intercalation in section 3.2, cell size changes and cell shape changes in section 3.3, cell division in section 3.4 and finally, ingression in section 3.5. In addition, observations on super-cellular myosin cables are described in section 3.6.

3.1 Tissue deformation

We measured and analysed tissue deformation using two different methodologies (PIV and cell track based). Firstly, we used averaged PIV to compute tissue deformation and expansion (3.1.1). Secondly, PIV based velocity fields were used to compute tissue deformation strain rates (3.1.2). Thirdly, automatic cell tracking data were used evaluate cell based tissue strain rates (3.1.3). Finally, tissue strain rate was evaluated utilising the semi-automatically tracked cells (3.1.4).

3.1.1 Tissue deformation based on averaged tissue velocity fields

To quantify tissue deformation we used PIV based tissue velocity fields. A detailed description of PIV is given in computational methods chapter (4.4.1). We evaluated PIV velocity fields independently for nine different embryos. Development in these nine time lapse sequences started generally at different time points. Additionally, orientations and positions of primitive streaks were not generally same in these nine embryos. To average velocity fields we had to perform a spatiotemporal alignment of all the embryos. Temporal alignment was performed by finding a similar developmental stage from each embryo and aligning gastrulation sequences in time. For spatial alignment position and orientation of the primitive streak were used to translate and rotate each embryo into the same coordinate system. After all the embryos were spatio-temporally aligned an averaged velocity field was computed. The spatiotemporal alignment of embryos is described in detail in subsection 4.4.1.

The averaged velocity field was used to compute tissue contraction expansion map. In this method an initial square grid was overlaid over embryo. The deformation of each grid cell was computed over time using the averaged tissue velocity field. The area of each cell of the grid was at each time point compared to the initial area by computing ratio between current area and the initial area. Contraction and expansion relative to the initial time was calculated and visualised with red colour (expansion) or blue colour (contraction) (Figure 3.1). The contraction-expansion map shows that tissue in the midline of the embryo started to contract first. This region then got larger eventually spanning the whole mesendoderm. Simultaneously to the contraction, tissues anterior to the primitive streak started to compress in the direction of streak extension and elongate perpendicular to the streak. Meanwhile, tissues surrounding the contracting mesendoderm started to expand all around the forming primitive streak. Finally, only site of the primitive streak was contracting and all other regions were expanding. In

addition, the deformation map showed how tissue was moving towards the primitive streak from lateral positions. The fact that contraction in midline of the embryo was the first event shown by the deformation map suggests that cells in the midline are pulling cells from the lateral positions.

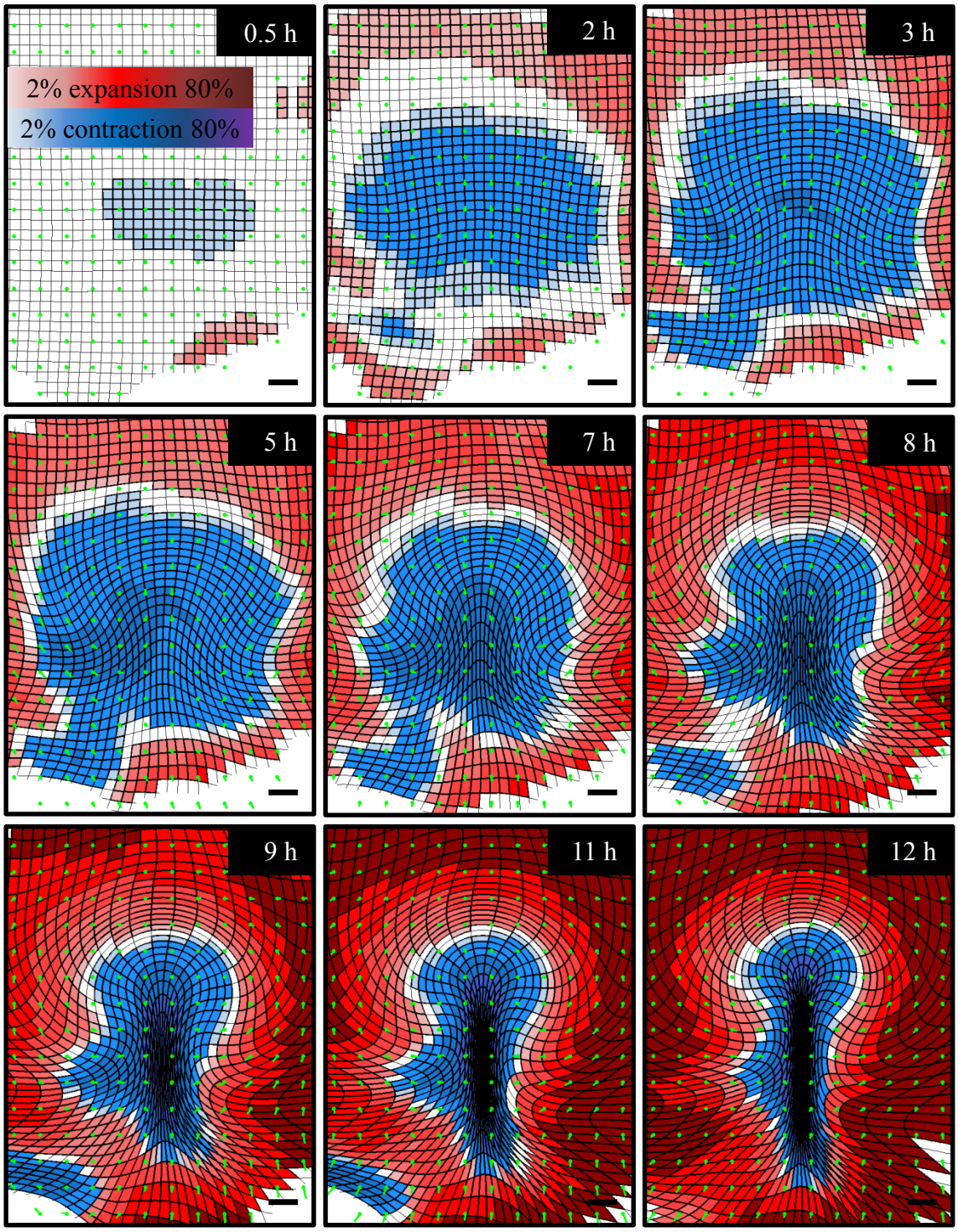

Figure 3.1 Tissue deformation of averaged tissue velocity fields. This is a contraction and expansion map computed from averaged tissue velocity fields from nine embryos. Contraction and expansion are annotated with blue and with red colour respectively. Spatiotemporal alignment between embryos was generated in a semi-automatic manner. The black scale bar is 200 μm.

3.1.2 PIV based tissue deformation strain rates

The tissue contraction expansion map described in previous subsection was considering deformation of the tissue relative to the start of the experiment. To better capture local tissue deformations we used PIV based tissue velocity fields to compute tissue deformation strain rates from the spatial gradients in the local velocity field. These strain rates were then averaged over spatiotemporal domains to visualise the strain rate field (Figure 3.2). The strain rate computation procedure is described in detail in computation methods chapter in subsection 4.4.3. Only the symmetric component of the strain rate field was visualised. The symmetric component was decomposed into anisotropic component and isotropic components. The anisotropic component was visualised as a blue line in direction of contraction, the perpendicular expansion component was not visualised. The isotropic component is shown as a circle, coloured red or blue in case of expansion or contraction, respectively.

The tissue deformation strain rate field evaluated and averaged in spatiotemporal domains revealed isotropic contraction at the site of streak formation (Figure 3.2). This site experienced contraction throughout the time sequence. The magnitude of the isotropic contraction increased over time. Regions around the site of primitive streak did not show any significant deformation initially. The surrounding regions started to isotropically expand towards the end of the time sequence. Simultaneous with the isotropic contraction an anisotropic contraction occurred in site of mesendoderm cells. This tissue was contracting in an orientation perpendicular to the midline of the embryo and expanding along the midline. The magnitude of this contraction increased over time and the region showing this type of behaviour expanded along the forming primitive streak and contracted in lateral direction. A down side of this PIV based analysis is that cell rearrangements are not captured in great detail and thus cell based methods are required as presented in following sections.

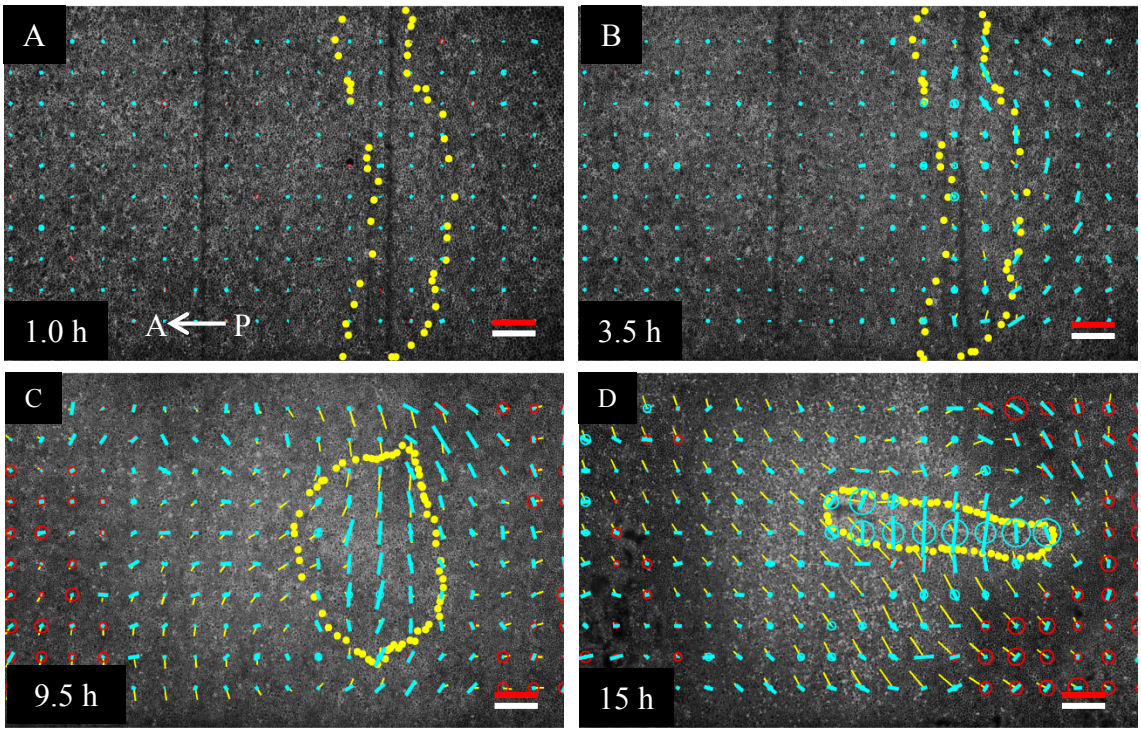

Figure 3.2 Tissue flow based tissue strain rates. A-D) Symmetric part of PIV based tissue deformation tensor during the primitive streak formation in chicken embryo. Isotropic component of the strain rate is visualised with blue circles and red circles for contraction and for expansion, respectively. The anisotropic component of the strain rate is shown with blue lines in direction of contraction. Yellow dots indicate the area that eventually collapses into the primitive streak. The tissue velocity field is shown with yellow lines where the open end indicates direction of the motion. The white scale bar is 200 μm long. Red scale bar indicates a strain rate of 10^{-4}/s and a tissue domain velocity of 4μm/min.

3.1.3 Tissue statistics based measure

The previous subsection described how the epiblast tissue is deforming. To dissect which individual cell behaviours reflect the observed tissue deformations we used automatic cell tracking data. A cell track based tissue deformation field was computed using the statistical methods explained in detail in computational method chapter (see section 4.8). The computed cell track based strain rate that corresponds to the PIV base deformation strain rate is known as the statistical symmetrized velocity gradient (V). This statistical measure quantifies how the cells are rearranging relative to each other over time. As in the previous subsection, only the symmetric strain rate component decomposed into an isotropic and anisotropic part was visualised. The anisotropic

component was visualised as a blue line in direction of contraction (Figure 3.3). The isotropic component was shown as red or blue coloured circles in case of expansion or contraction respectively.

Before the onset of tissue motion there were no appreciable deformations (Figure 3.3 A). Once the motion initiated, the mesendoderm cells started to rearrange causing the tissue to expand along the midline and contract perpendicular to that (Figure 3.3 B). The tissue at the site of streak formation started to contract isotropically. Similarly, the tissue anterior form the forming primitive streak started to contract isotropically. Four hours later similar deformation patterns were present (Figure 3.3 C). At this stage the magnitudes of both anisotropic and isotropic contraction had increased. Contractions were still occurring throughout the mesendoderm cell population that had now deformed to cover a larger area along the forming primitive streak. Four hours later the magnitudes of both types of contraction were still strong at site of the primitive streak (Figure 3.3 D), but the relative magnitude of the isotropic contraction had increased. Additionally, tissue anterior from the primitive streak was contracting. The magnitudes and spatiotemporal patterns of the isotropic and anisotropic strain rates calculated by both methods (cell and PIV based) were in a good agreement.

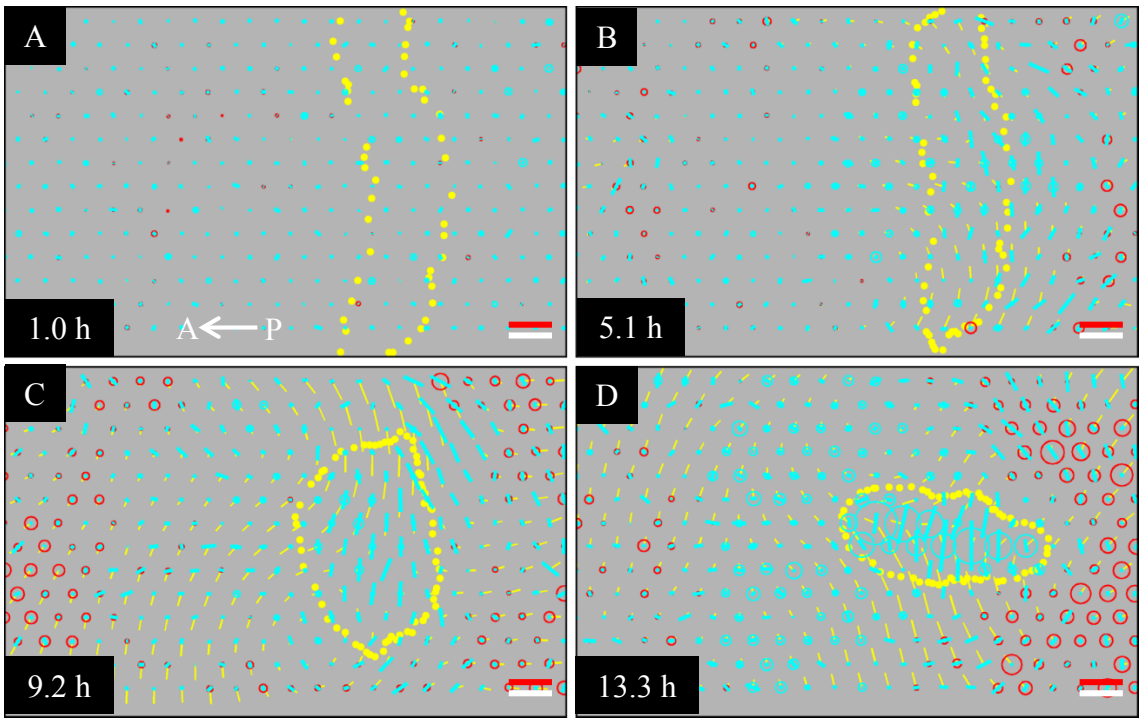

Figure 3.3 Tissue strain rate based on individual cells. A-D) Symmetric part of cell tracks based tissue deformation strain rate tensor during the primitive streak formation in chicken embryo. Isotropic component of the strain rate is visualised with blue circles and red circles for contraction and for expansion, respectively. Anisotropic component of the strain rate is shown with blue lines in direction of contraction (the positive component with the same magnitude is not shown). Yellow circles indicate the area that eventually collapses to the primitive streak. Tissue velocity field is shown with yellow lines where open ends of lines indicate direction of the motion. The white scale bar is 200 μm long. Red scale bar indicates a strain rate of 10^{-4}/s and a tissue domain velocity of 4μm/min.

3.1.4 Tissue tectonics based measure

To estimate tissue strain rates in the semi-automatically tracked domains we used a different statistical method than the one used in previous subsection. This method is called tissue tectonics and details of the method are given in computational methods chapter (section 4.9). The method computes a deformation strain rate for each cell in a domain and then averages all the deformations within domains. Principal components of the symmetric part of the strain rate are presented as blue line and red line in direction

contraction and in direction of expansion, respectively. A sample domain of tissue deformation strain rates of individual cells is presented in figure 3.4 A.

We analysed the four semi-automatically annotated domains presented in previous chapter (Figure 2.6). The tissue tectonics based deformation strain rates were computed in each domain in all time points. The strain rates of all the time points within each domain and were then pooled together into polar histograms (Figure 3.4 B-E). The value in each bin was the average of all the principal magnitudes falling into the bin. The bins were then coloured similarly as the strain rate lines in figure 3.4 A. The streak domain showed expansion along the primitive streak and contraction perpendicular to that (Figure 3.4 B). The magnitudes of the deformations were weaker in all the other three domains (Figure 3.4 C-E). Both the lateral and the posterior domains (Figure 3.4 C and E) showed similar patterns as the streak domain (Figure 3.4 B). The anterior domain did not show a clear pattern (Figure 3.4 D). All this is in good agreement with deformation tensor calculations of the previous section suggesting that the deformation is strongest at the site of the forming primitive streak.

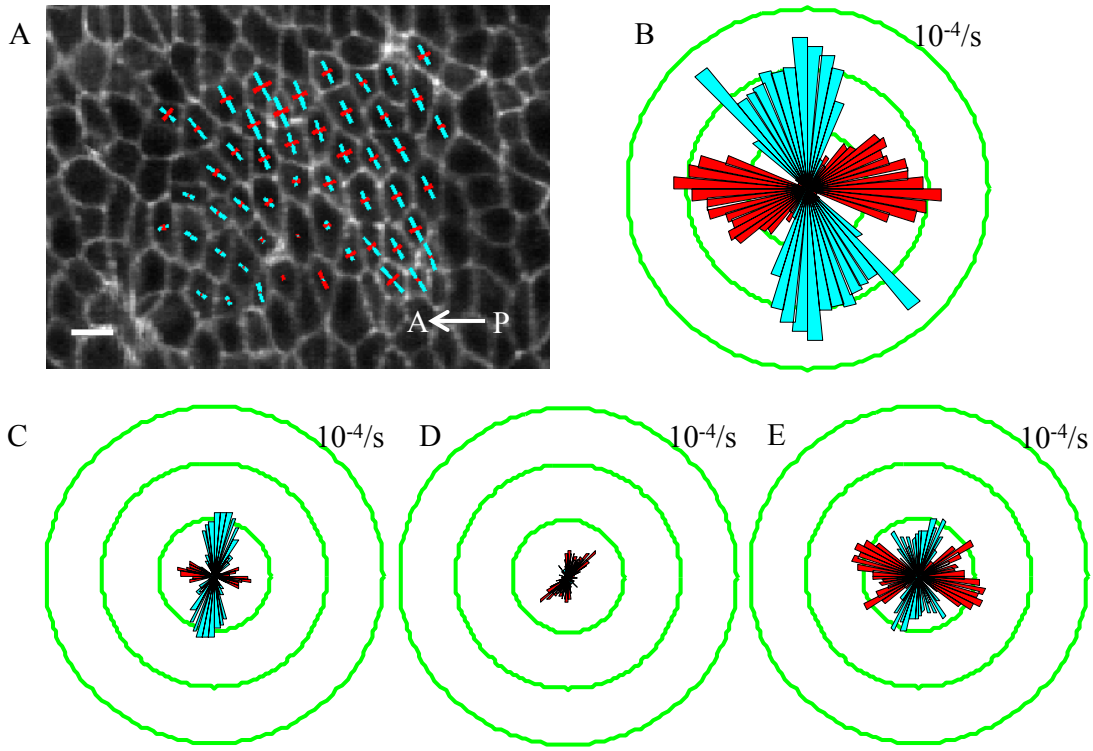

Figure 3.4 Tissue tectonics based average tissue strain rate in semi-automatically annotated domains. A) Symmetric component of tissue strain rate visualised for a time point. Blue line and red line indicate direction of contraction and expansion, respectively. **B)** Pooled, magnitude weighted polar histogram of all the strain rates of all the time points of the streak domain. **C-E)** Same as B for the lateral domain, for the anterior domain and for the posterior domain, respectively. The white scale bar is 10 μm and 10^{-4}/s.

3.2 Intercalation

3.2.1 Tissue statistics based measure

To dissect how much of the observed cell track based tissue deformation is due to cell-cell intercalation we used a statistical method. We evaluated this measure for the same automatic tracking data set as used deformation field evaluation in previous section. The measure we calculated is the statistical topological rearrangement rate (P). The method of calculation is described in detail in computational methods chapter (section 4.8). The resulting intercalation strain rate is visualised in a manner similar to the tissue deformation strain rate in the previous sections. In visualisations, blue colour and red colour correspond to contraction and expansion, respectively.

Prior to the onset of motion an alignment (perpendicular to the midline) of anisotropic components of the intercalation strain rates was visible on posterior side of the mesendoderm domain indicating a rearrangement of tissue (Figure 3.5 A). After the initiation of motion the alignment disappeared and a new weak alignment started to form indicating contraction of the mesendoderm (Figure 3.5 B). Four hours after the onset of motion the whole mesendoderm domain showed very clear alignment of the anisotropic intercalation strain rate components perpendicular to the forming primitive streak (Figure 3.5 C). Another 4 hours later the alignment had spread towards anterior as the developing primitive streak was extending (Figure 3.5 D). These findings clearly show that the cells in the mesendoderm intercalate, pulling tissue from lateral positions towards the midline of the embryo and that these tissues are pushed along the midline to induce extension of the primitive streak.

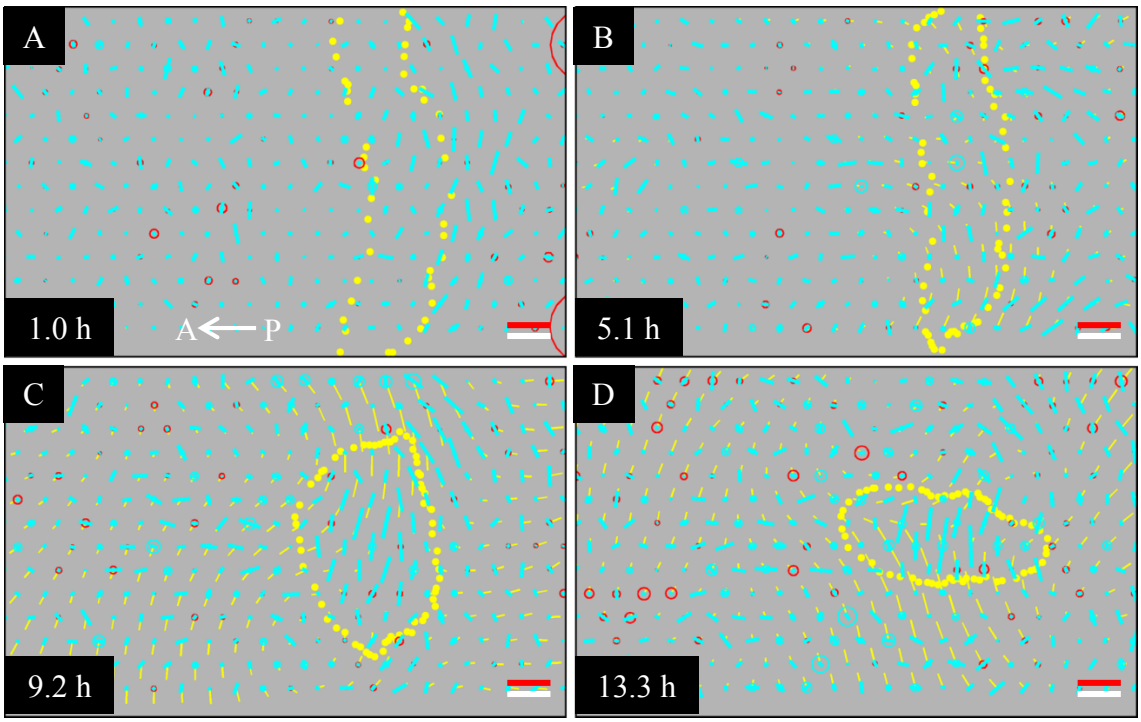

Figure 3.5 Cell based intercalation strain rate. A-D) Symmetric part of cell tracking based intercalation strain rate tensor during the primitive streak formation in chicken embryo. Isotropic component of the strain rate is visualised with blue circles and red circles for contraction and for expansion, respectively. Anisotropic component of the strain rate is shown with blue lines in direction of contraction (the positive component with the same magnitude is not shown). Yellow circles indicate the area that eventually collapses to the primitive streak. Tissue velocity field is shown with yellow lines where open end of lines indicate direction of the motion. The white scale bar is 200 μm long. Red scale bar indicates a strain rate of 10^{-4}/s and a tissue domain velocity of 4μm/min.

3.2.2 Semi automatically annotated domains

To estimate the intercalation rate in the semi-automatically tracked domains we used a tissue tectonics based measure. Details of the method are given in computational methods chapter (section 4.9). A sample domain of intercalation strain rates of individual cells is presented in figure 3.6 A.

We analysed the four semi-automatically annotated domains presented in previous chapter (Figure 2.6). The tissue tectonics based deformation strain rates were computed in each domain in all time points. The strain rates of all the time points within each

domain were then pooled together into polar histograms (3.6 B-E). The value in each bin was the average of all the principal magnitudes falling into the bin. Bins were then coloured similarly as the strain rate lines in figure 3.6 A. The streak domain showed expansion along the primitive streak and contraction perpendicular to that (Figure 3.6 B). Magnitudes of the deformation were weaker in all the other three domains (Figure 3.6 C-E). Both the lateral and the posterior domains (Figure 3.6 C and E) showed similar patterns as the streak domain (Figure 3.6 B). In the anterior domain magnitude of the intercalation was weak (Figure 3.6 D). This suggests that tissue at the site of the primitive streak is intercalating strongest and adjacent tissues intercalate also but less vigorously.

Other evidence of intercalation was the fact that cells in the semi-automatically annotated streak domain and lateral domain rearranged in a biased manner (Figure 2.6 B and E). In both of these domains cells were initially forming a square and a linearly organised set of cells was selected (coloured blobs). Over time the initial selection of cells expanded along the streak axis and contracted perpendicular to that. The cells marked with the blobs spread along the anterior-posterior axis. Cells of the posterior domain showed similar but weaker behaviours as those in the streak domain and the lateral domain. The posterior domain did not show contraction (Figure 2.6 D). The anterior domain stayed almost the same except for some small rearrangements of the cells in that domain (Figure 2.6 C).

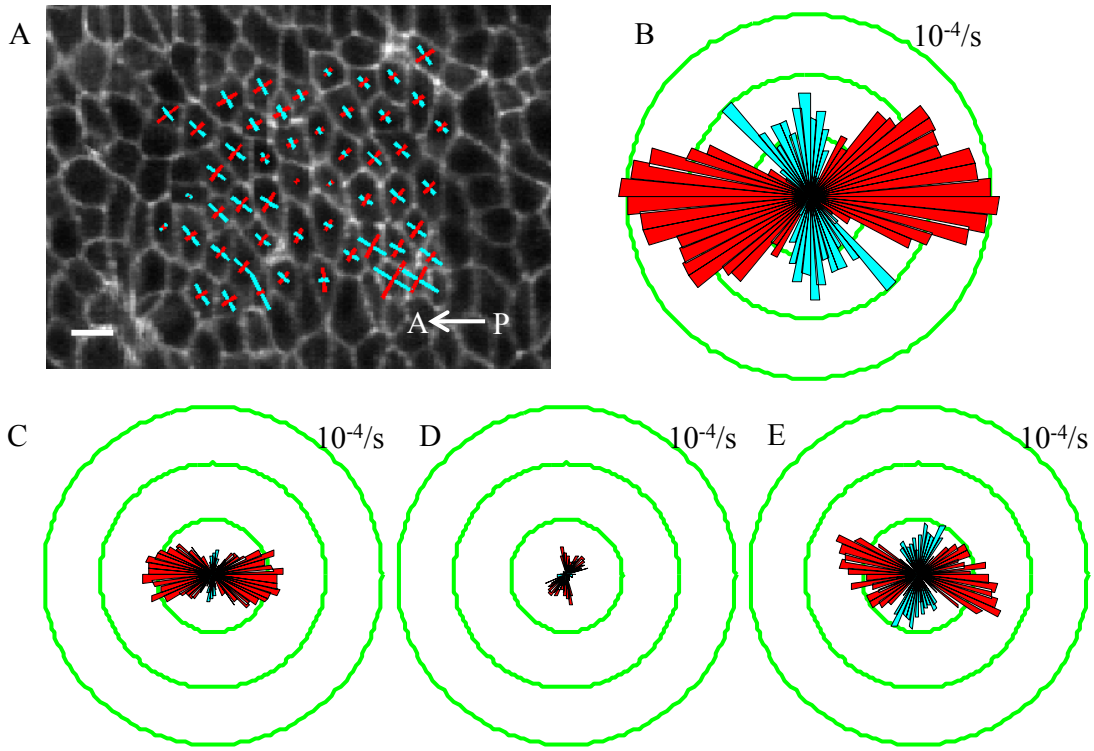

Figure 3.6 Tissue tectonics based average intercalation strain rate in semi-automatically annotated domains. A) Symmetric component of intercalation strain rate visualised for one time point. The blue and red lines indicate direction of contraction and expansion, respectively. **B)** Pooled, magnitude weighted polar histogram of all the strain rates of all the time points of the streak domain. **C-E)** Same as B for the lateral domain, for the anterior domain and for the posterior domain, respectively. The white scale bar is 10 μm and 10^{-4}/s.

3.3 Cell size and cells shapes changes

In addition to intercalation, cell shape changes are another important potential driver of the primitive streak formation. The average cross sectional area of cells is analysed in subsection 3.3.1. The cell shape changes are further analysed using statistical methods in subsections 3.3.2 and 3.3.3. Finally the alignment of cell shapes is analysed in last subsection (3.3.4).

3.3.1 Cross sectional area of cells

We used time independently segmented cells to quantify how averaged cross sectional area of cells is changing over time. To visualise cross sectional area changes the embryo was divided into small domains in each of which the average cross sectional area was

computed for each time point (Figure 3.7 A). These computations showed that a gradient in the average cross sectional area was already present prior to the onset of motion in the embryo (Figure 3.7 A first panel). The cell size was smallest at the site where primitive streak was going to form and the average cell size was radially increasing from this site. Starting from this initial time point the cross sectional area of cells was gradually decreasing over time (Figure 3.7 A second and third panel). The radial gradient was preserved over time.

Due to light scattering properties of the embryonic tissue it was not possible to image full length of mesendoderm cells in apical-basal direction. Thus a direct measurement of all the cell volumes was impossible. As a solution only volumes of cells just prior to the cytokinesis were measured, as these cells were rounding up and became nearly completely visible from the apical side of the epiblast. This method is described in detail in computational methods chapter (section 4.7). The cross sectional area of all the cells and cross sectional area of cells prior to cytokinesis was measured in two domains from the embryo (domains B and C in Figure 3.7 A). the relative cross sectional area of cells decreased significantly (by 40-65% depending on position) in both of the domains, whilst the cross sectional area of the dividing cells stayed nearly constant (Figure 3.7 B and C). This implies that cells are elongating along the apical-basal axis in preparation for ingression, resulting in the observed decrease in cross sectional area.

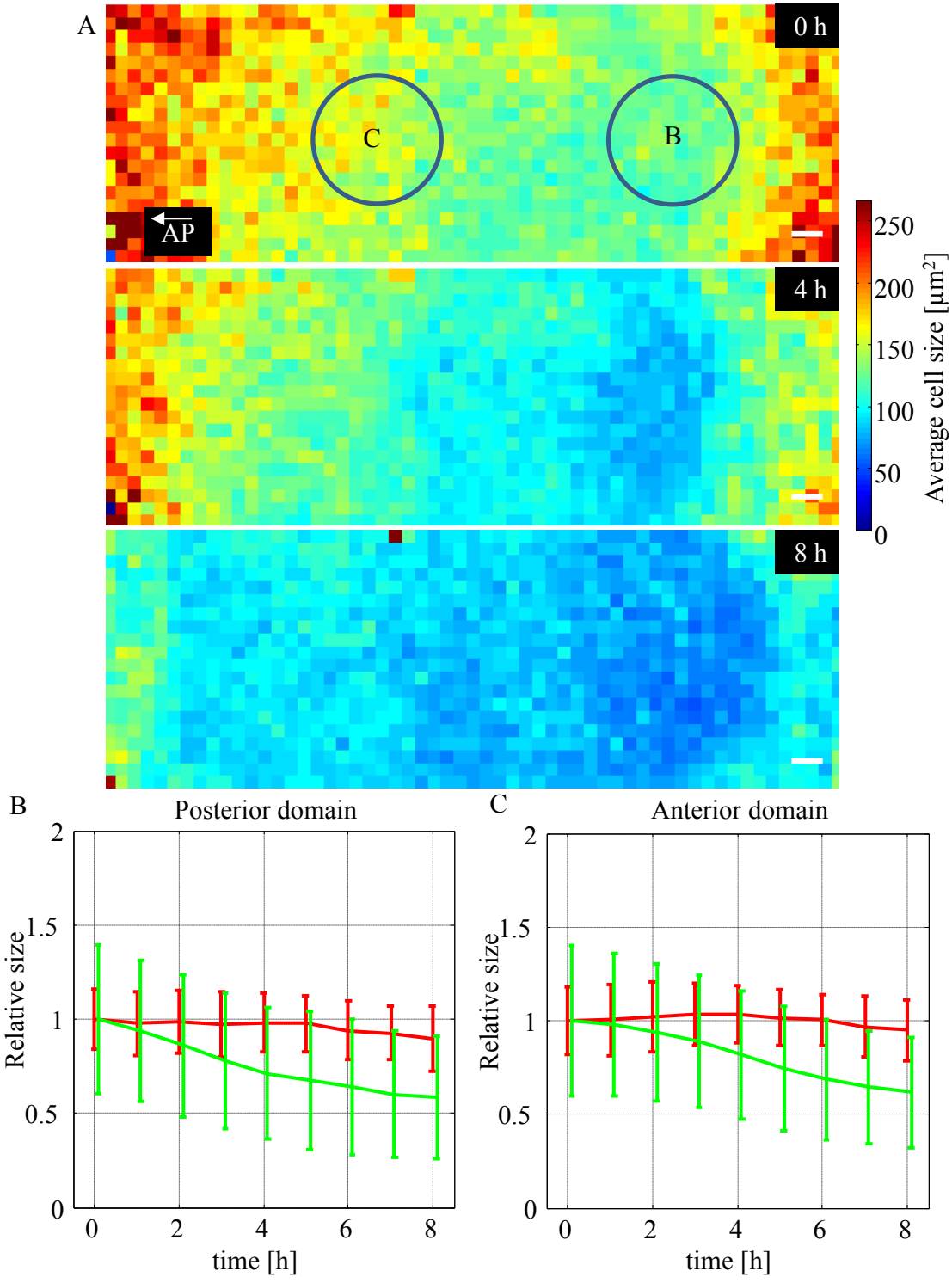

Figure 3.7 Changes in cell volume and cross sectional area during early development. A) Changes in cellular cross-sectional area over time. The average cell diameters were calculated from the segmented images in small domains and colour coded as indicated in the legend. Size of coloured squares is 6,600 µm^2. The white scale bar is 200 µm. **B)** Relative average cell volume of spherical cells prior to cytokinesis (red line) and relative average apical cell diameter (green line) in the posterior domain (marked with B in panel A). **C)** Same volume and cross-sectional area measurements for the anterior domain (marked with C in panel A).

In addition, change in cross sectional area of cells of semi-automatically annotated domains was quantified. The domains are shown in Figure 2.6. The average cross sectional area of cells was decreasing at a similar rate in all of the four domains (Figure 3.8). The streak domain and the lateral domain ended up having the smallest cross sectional area. The average cross sectional area of the lateral domain was initially at the level of the anterior domain and the posterior domain but decreased to the level of the streak domain. This suggests that all mesendoderm cells significantly contract their apical cross section, presumably in preparation for ingression (Figure 3.8 and Figure 2.6 A).

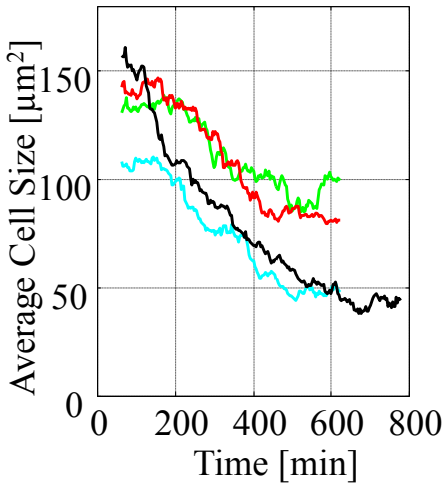

Figure 3.8 Average cross sectional area cells in each of semi-automatically annotated domain. The streak domain is blue, the lateral domain is black, the anterior domain is green and the posterior domain is red.

3.3.2 Tissue statistics based measures

To quantify cell shapes and cell sizes we used a similar statistical method as was used for quantification of tissue deformation and cell intercalation. Here we used tissue texture tensor. This method is described in detail in computational methods chapter (section 4.8). The tensor quantifies the magnitude and directional orientation of cell shapes. The magnitudes of both principal components of the texture tensor, reflecting

average cross sectional areas of cells, are visualised with red lines in corresponding principal directions. Prior to the onset of motion mesendoderm cells are aligned in a direction perpendicular to the midline of the embryo (Figure 3.9 A). After the motion has started the alignment of the mesendoderm cells got stronger (Figure 3.9 B). Additionally, the cross sectional area of cells decreased throughout the embryo. The alignment was no longer detectable four hours later and did not reappear (Figure 3.9 C and D). The computed decrease in the cross sectional area of cells is in good agreement with the measure presented in the previous subsection.

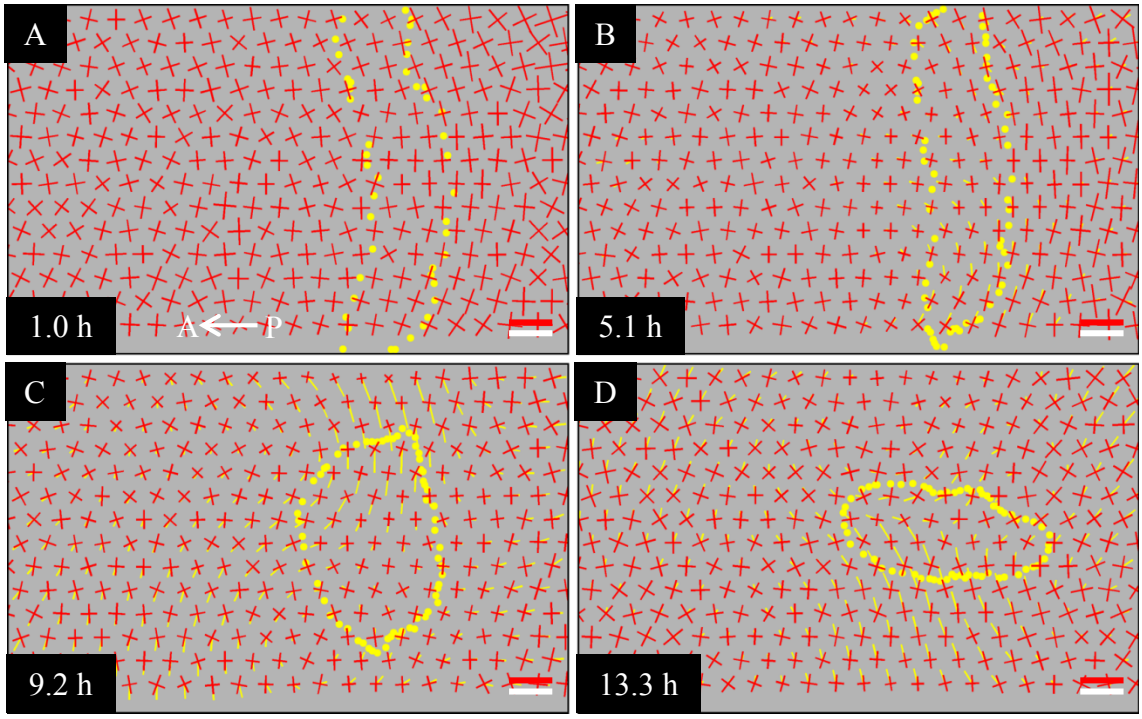

Figure 3.9 Cell based tissue texture tensor. A-D) Symmetric part of cell tracking based tissue texture tensor during the primitive streak formation in chicken embryo. Both principle components of the tensor are shown with red lines. Yellow circles indicate the area that eventually collapses into the primitive streak. Tissue velocity field is shown with yellow lines where the open end indicates direction of the motion. The white scale bar is 200 μm long. Red scale bar indicates a tensor magnitude of 200 μm^2 and a tissue domain velocity of 4μm/min.

To further quantify how the cross sectional area of cells and cell shapes are changing over time the temporal change of the tissue texture tensor was computed. This measure is called the statistical internal strain rate and details are given in the computational methods chapter (section 4.8). This statistical cell shape change strain rate is visualised similarly to the tissue deformation strain rate and to the intercalation strain rate illustrated in two previous subsections. Red colour and blue colour correspond to the expansion and contraction, respectively. Before the onset of motion the anisotropic component of the symmetric part of the tensor showed contraction along to the midline for the mesendoderm cells (Figure 3.10 A). This indicated an elongation of the shapes of the mesendoderm cells in direction perpendicular to the midline. After the motion started an anisotropic contraction indicated counteracting the occurred elongation of the mesendoderm cells (Figure 3.10 B). Anisotropic components started to become stronger at the site of the forming primitive streak towards the end of the time sequence (Figure 3.10 D).

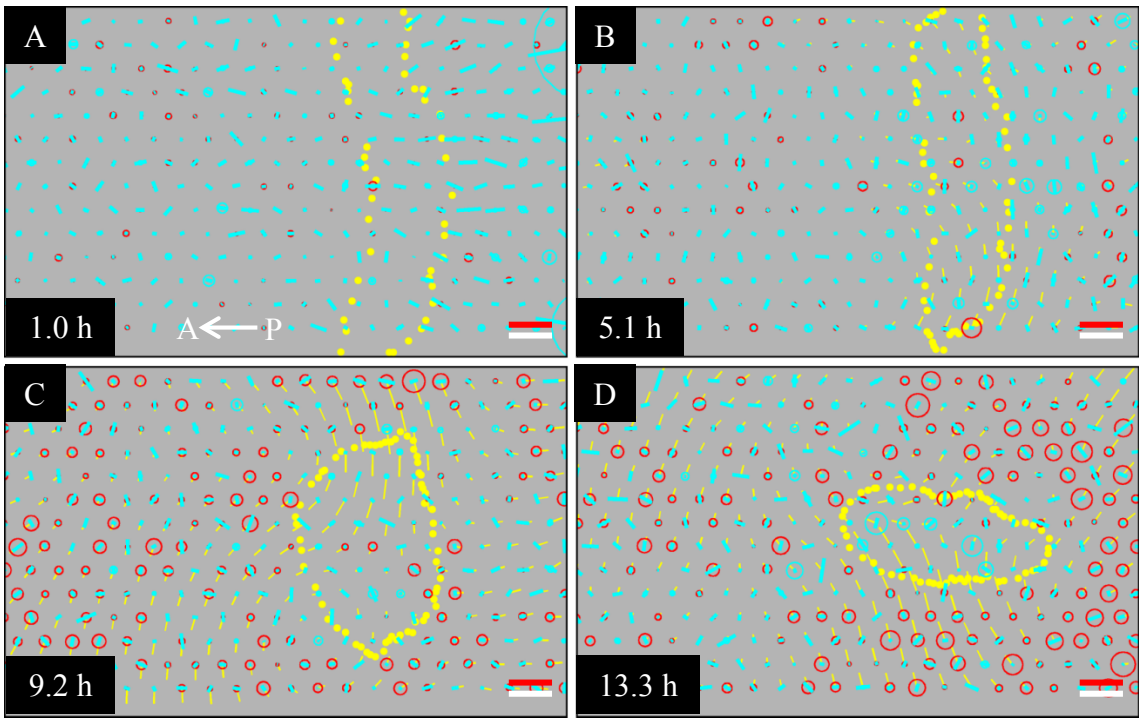

Figure 3.10 Cell shape strain rate based on cell tracking. A-D) Symmetric part of cell tracking based cell shape strain rate tensor during the primitive streak formation in chicken embryo. Isotropic component of the strain rate is visualised with blue circles and red circles for contraction and for expansion, respectively. Anisotropic component of the strain rate is shown with blue lines in direction of contraction (the positive component with the same magnitude is not shown). Yellow circles indicate the area that eventually collapses into the primitive streak. Tissue velocity field is shown with yellow lines where the open end of lines indicates direction of the motion. The white scale bar is 200 µm long. Red scale bar indicates a strain rate of 10^{-4}/s and a tissue domain velocity of 4µm/min.

To compare the relative magnitudes of the intercalation strain rate and the cell shape change strain rate we overlaid the anisotropic components of these tensors. Intercalation and cell shape change were quantified with blue and green colour, respectively. Prior to the onset of motion these to anisotropic components had opposite directions with similar magnitudes (Figure 3.11 A). This suggests that local intercalations and shape changes occur, due to a balancing of the effects of shape change and intercalation and that no tissue deformations occur at this stage of development.

This is also confirmed by statistical tissue deformation strain rate prior the motion onset (Figure 3.3 A). After the motion onset only few spatially scattered motif pairs showed opposite directions (Figure 3.11 B-D). In addition, magnitudes of the intercalation grew stronger than the magnitudes of the cell shape changes, showing that intercalation became a dominant factor.

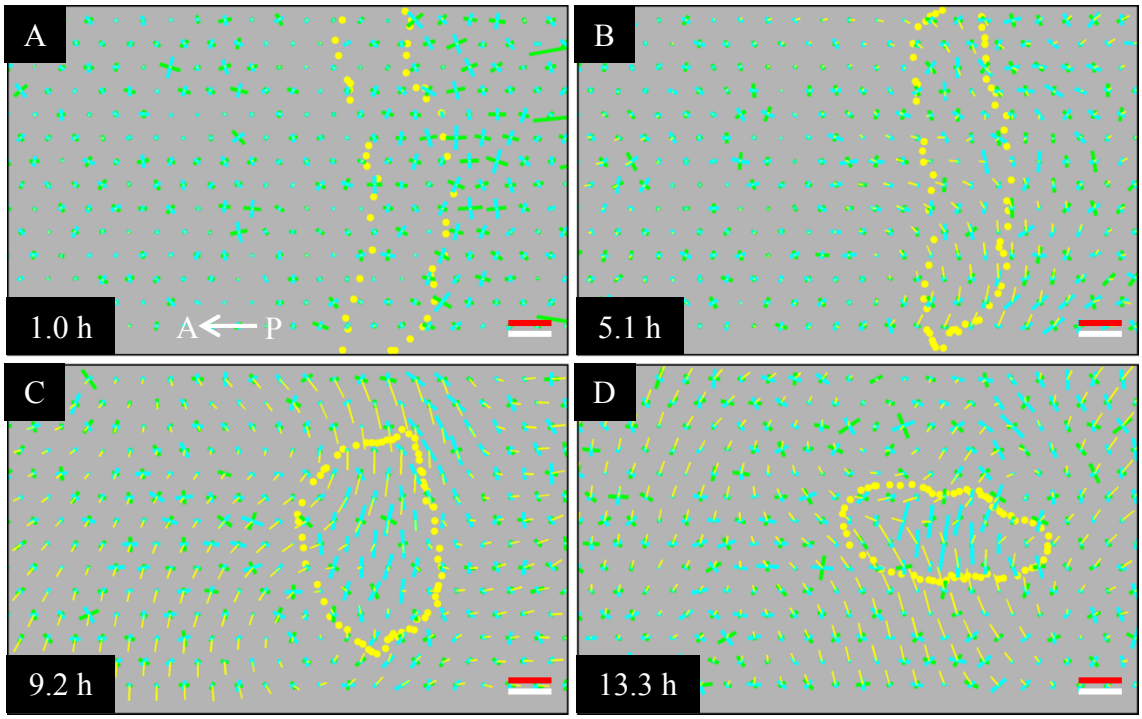

Figure 3.11 Anisotropic components of cell shape strain rate and intercalation strain rate. A-D) Anisotropic components of symmetric part of cell tracking based intercalation strain rate tensors during the primitive streak formation in chicken embryo. The anisotropic component of the intercalation strain rate is shown with blue lines in direction of contraction (the positive component with the same magnitude is not shown). Similarly, the anisotropic component of the cell shape strain rate is shown with green lines. Yellow circles indicate the area that eventually collapses into the primitive streak. Tissue velocity field is shown with yellow lines where the open end indicates direction of the motion. The white scale bar is 200 μm long. Red scale bar indicates a strain rate of 10^{-4}/s and a tissue domain velocity of 4μm/min.

3.3.3 Tissue tectonics based measure

To quantify cell shape change in the semi-automatically annotated domains a tissue tectonics based measure was used. Details of this method are given computational

methods chapter (section 4.9). This measure evaluated a cell shape change strain rate for each cell within each domain for each time point (Figure 3.12 A). Red and blue colours correspond to expansion and contraction, respectively. The measure was evaluated for the semi-automatically annotated domain illustrated in previous chapter (Figure 2.6). Both the streak domain and the lateral domain showed nearly uniform contraction (Figure 3.12 B and C). The anterior domain and the posterior domain did not show any deformation (Figure 3.12 D and E). This again is in a good agreement with the quantification of the average cross sectional areas of cells. This also suggests that mesendoderm cells are actively contracting whilst cells in other regions might get smaller due to cell divisions.

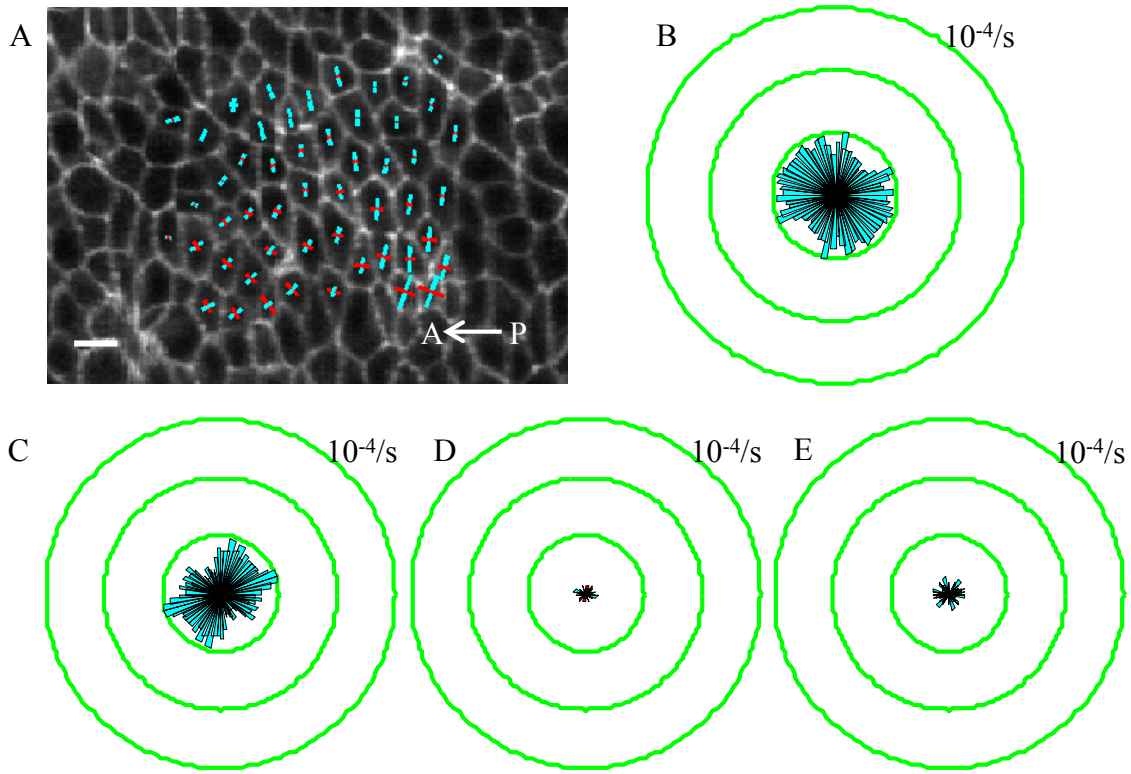

Figure 3.12 Tissue tectonics based average cell shape strain rate in semi-automatically annotated domains. A) Symmetric component of cell shape strain rate visualised for a time point. Blue line and red line indicate direction of contraction and expansion, respectively. **B)** Pooled, magnitude weighted polar histogram of all the strain rates of all the time points of the streak domain. **C-E)** Same as B for the lateral domain, for the anterior domain and for the posterior domain, respectively. The white scale bar is 10 μm and 10^{-4}/s.

3.3.4 Alignment of cell shapes

To quantify the alignment of the cells, the automatically tracked and segmented cell outlines were used. An ellipse was fitted to the shape of each cell in each time point. This was done using the normalized second-order central moments of pixels of the segment[83]. This was done independently for each cell and each time point of time lapse sequence. The orientation of the major axis of the fitted ellipse was then considered to represent the orientation of the corresponding cell. A cell was considered to be polarised if the eccentricity of the fitted ellipse was greater than 0.87. To visualise spatio-temporal patterns of cell alignment the embryo was divided into square domains (Figure

3.13). To quantify the average polarity in each domain a polar histogram was constructed from the orientations of polarised cells.

This measure showed a clear pattern amongst the mesendoderm cells prior to the motion onset (Figure 3.13 A). These cells were polarised along the in direction perpendicular to the midline of the embryo. After the motion initiated the polarity increased (Figure 3.13 B). During the following three hours the alignment was lost completely (Figure 3.13 C). This observed bias and alignment in shapes of cells is also observed the tissue texture tensor measure (Figure 3.9). The initially forming polarity of cells might facilitate intercalation and formation of the observed myosin chains (see section 3.6). The cell polarity could be cellular mechanism or rise from the physical properties of the epiblast. Further studies are required to establish how the polarity rises.

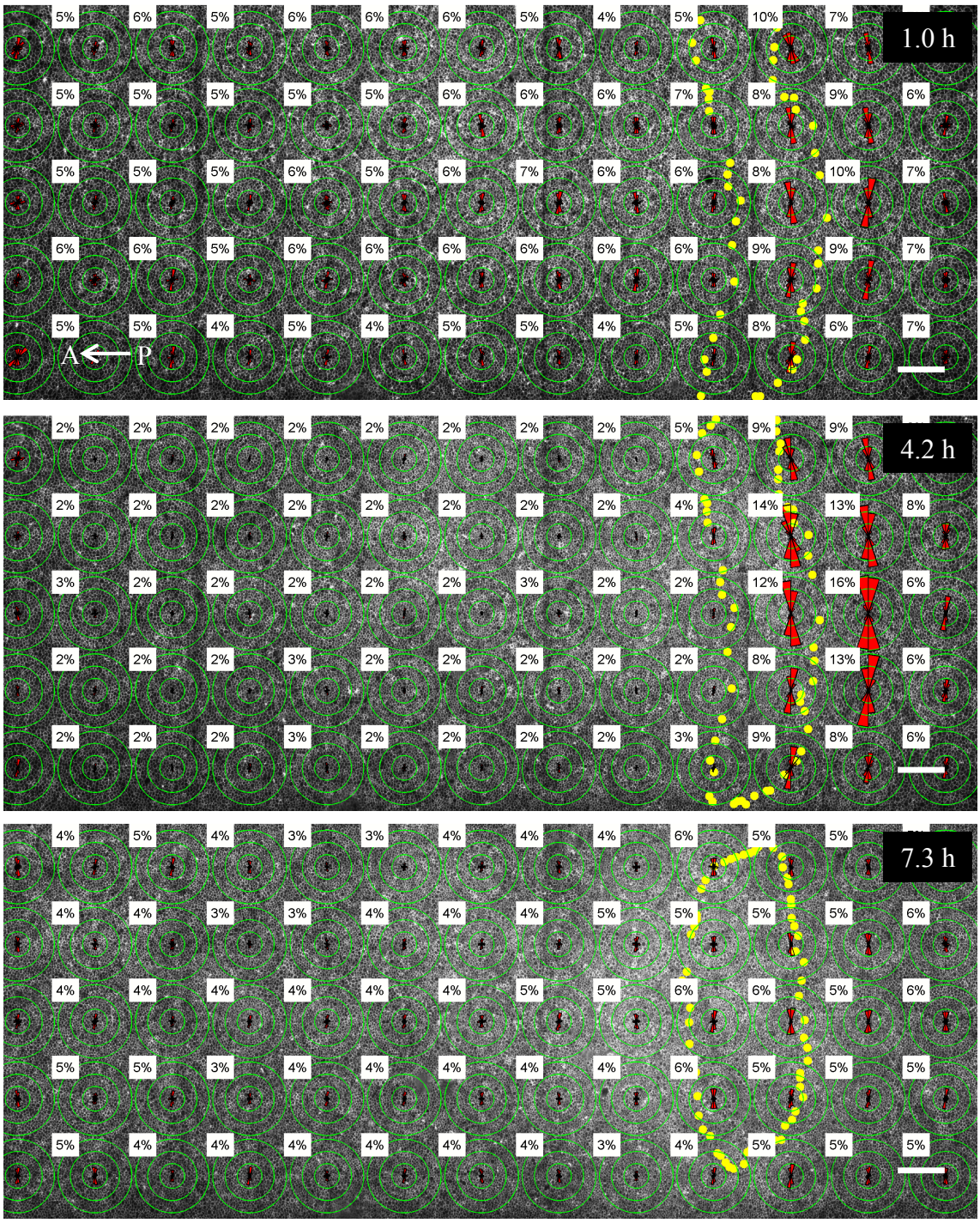

Figure 3.13 Alignment of cell shapes. An ellipse is fitted to shape of each individual cell. Only cells with ellipse eccentricity of >0.87 are considered. Orientations of the ellipses with eccentricity greater than 0.87 are used to form polar histograms in several individual domains. Percentage point numbers show how many percent of cells are considered in each domain. Scale bar in each panel is 200 μm.

3.4 Cell divisions

3.4.1 Frequency of cell divisions

The frequency of cell divisions was measured from both the automatically tracked cell data sets and from the semi-automatically tracked data sets. We observed that cells were dividing on average once in 6 hours, but that rates of cell divisions were not constant over time in the semi-automatically annotated domains (Figure 3.14 A). The same was true for the automatically tracked domains (Figure 3.14 B). This suggests most likely a partial synchrony but the implications of this are currently unknown.

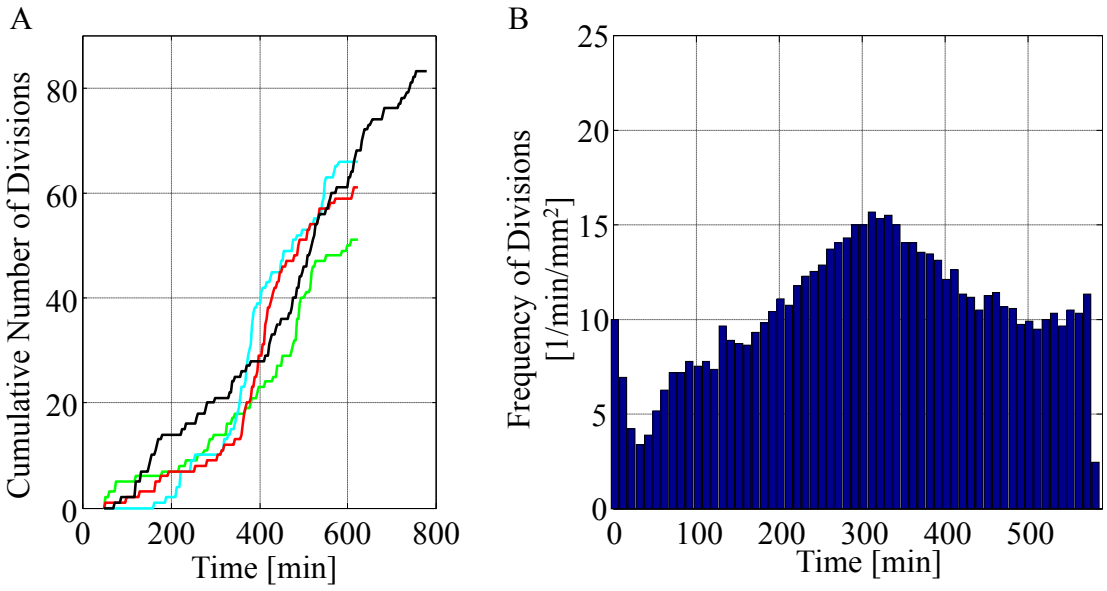

Figure 3.14 Frequency of cell divisions. A) Cumulative number of cell division events in each of semi-automatically annotated domain. The streak domain is blue, the lateral domain is black, the anterior domain is green and the posterior domain is red. **B)** Number of cell divisions over time in the embryo shown in figure 3.15.

3.4.2 Orientation of cell divisions

The orientation of cell divisions in different regions in the embryo was quantified from the automatically tracked cell data sets. The orientation of a division was measured by quantifying the orientation between two daughter cells immediately after the cytokinesis relative to the anterior-posterior axis of the embryo. To visualise average orientation of

the cell divisions the embryo was divided into square domains. Then a polar histogram was constructed for each domain by pooling the orientations of cell divisions within the domain over a period of two hours (Figure 3.15).

Prior to onset of motion cell divisions were polarised in the direction perpendicular to the midline of the embryo within mesendoderm area (Figure 3.15 A). After the start of motion the divisions became less polarised (Figure 3.15 B) until two hours later the polarity was almost completely lost (Figure 3.15 C). The polarity of the cells coincides with alignment of the cell shapes (Figure 3.13). This suggests these two events are likely related. It is a possibility that biased cell shapes are biasing orientations of cell divisions, alternatively it is possible that the same mechanism that biased cell orientation (tension) also biases the direction of cell division. Furthermore, as cell divisions are preferably occurring in direction perpendicular to the forming primitive streak it is unlikely that cell divisions are driving elongation of the primitive streak.

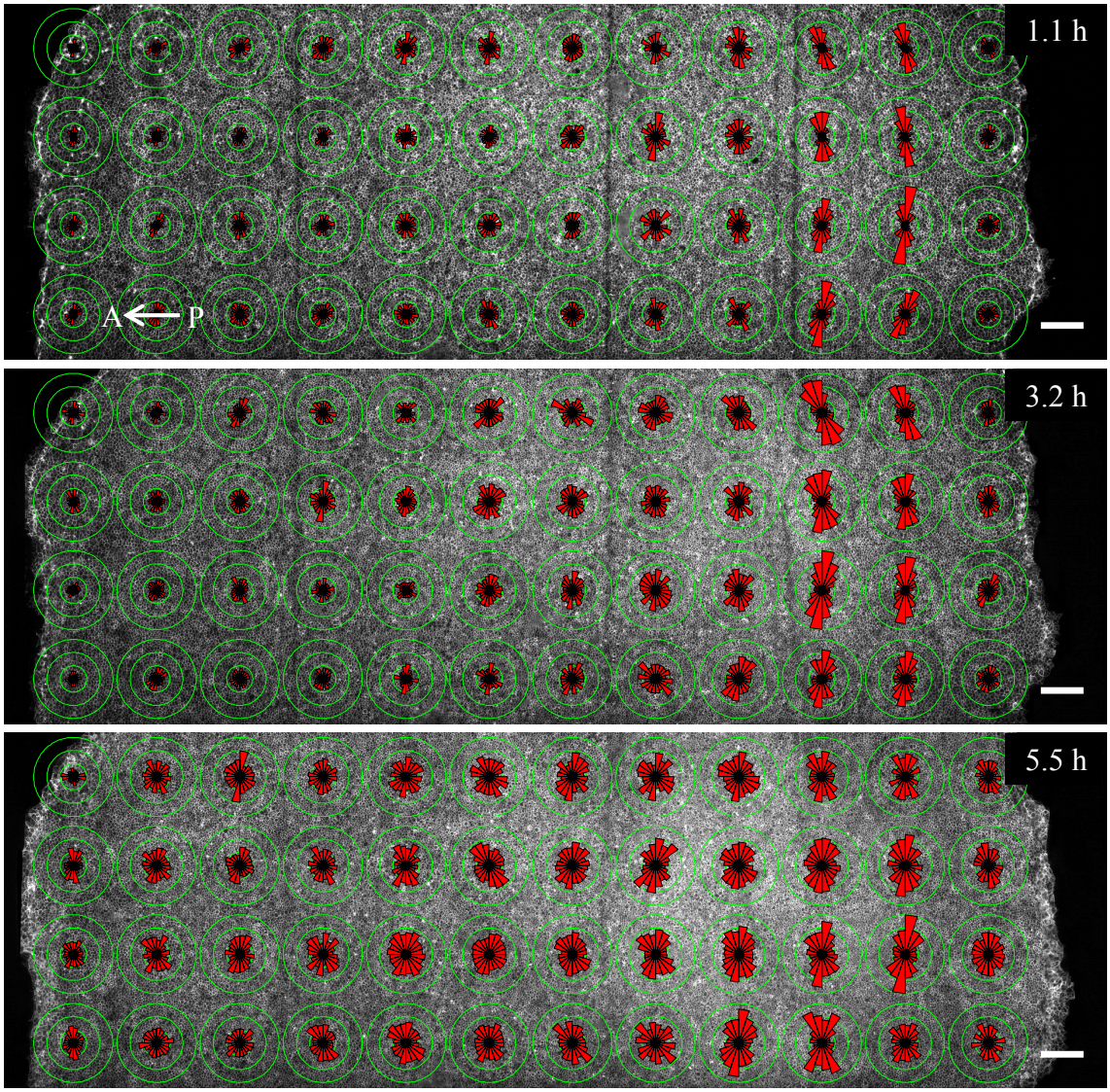

Figure 3.15 Polar histograms showing the distributions of the cell division axes in domains in different parts of the embryo. Each domain contains the all the cell divisions occurring over a 2.1 h period. Scale bar is 200 μm.

3.5 Ingression

3.5.1 Semi-automatically annotated domains

Cell ingressions were quantified from the semi-automatically tracked domains illustrated in previous chapter (Figure 2.6). For the first 6 hours not many ingression events occur in any of the domains (Figure 3.16). After this number of ingression events starts to rapidly increase in the streak domain. Similarly, 3.5 hours after this the number of ingressions starts to increase in the lateral domain (Figure 3.16). The number of

ingressions stays at much lower levels in both anterior domain and posterior domains. All this suggests is in agreement that mostly mesendoderm cells are ingressing and that ingressions occur only whilst the primitive streak is already forming. It seems that initial decrease of the cross sectional area of the mesendoderm cells culminates into ingression.

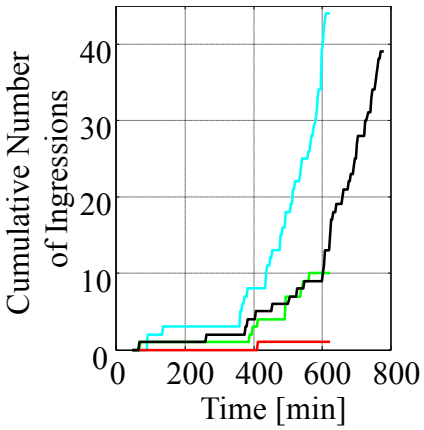

Figure 3.16 Cumulative number of ingression events in each of the semi-automatically annotated domains. The streak domain is blue, the lateral domain is black, the anterior domain is green and the posterior domain is red.

3.5.2 Automatically tracked cells

To quantify spatiotemporal occurrence of ingression events from whole embryo automatically tracked cell data were used. There was no clear initial pattern in occurrence of ingression events (Figure 3.17 first panel). Later a pattern started to emerge highlighting the site of the forming primitive streak as a site for the ingression events (Figure 3.17 second and third panels).

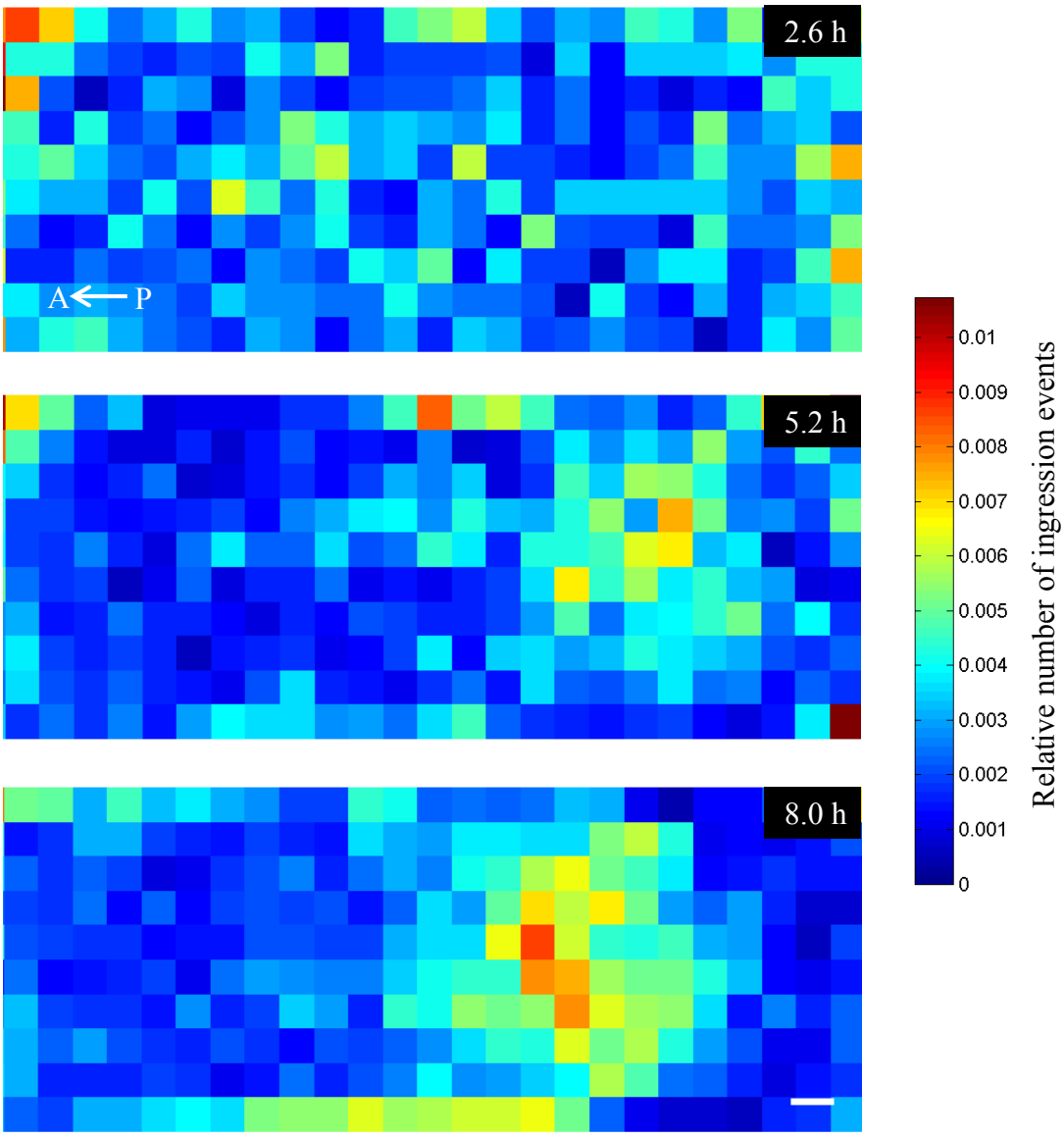

Figure 3.17 Number of ingression events. Blue colour and red colour correspond to less frequent and more frequent cell division event, respectively. The embryo is same as in figure 3.15. Scale bar is 200 µm.

3.6 Role of myosin cables during primitive streak formation

We investigated role of myosin II in the primitive streak formation utilising phosphorylation of myosin light chain[84]. We found that myosin localises into the cell junctions in an organised manner in the posterior area pellucida. The myosin localised into the aligned junctions spanning 2-8 cell diameters and thus forming cables (Figure 3.18 A). The cables were not present in the posterior area pellucida. These cables appear

when the mesendoderm starts to contract and the lateral cell flows initiate[85]. These experiments were carried out by Dr Manli Chuai.

To investigate involvement of myosin I family to the formation of the observed cables we used an inhibitor called pentachloropseudilin (PCP). This chemical inhibited formation of the observed myosin cables in posterior area pellucida (Figure 3.18 B). Interestingly the normal tissue motions and thus the formation of the primitive streak were completely blocked after addition of the PCP (Figure 3.19). Prior to the addition the inhibitor the cell based tissue strain rates were seemingly normal but after the addition of the inhibitor all tissue deformations stopped rapidly (Figure 3.19 A). Similarly, both the intercalation and cell shape change strain rate components indicated absence of these processes within the tissue after application the PCP (Figure 3.19 B). This suggests that the myosin I is required for the formation of the phosphorylated myosin light chain cables and that these cables are required for the formation of the primitive streak.

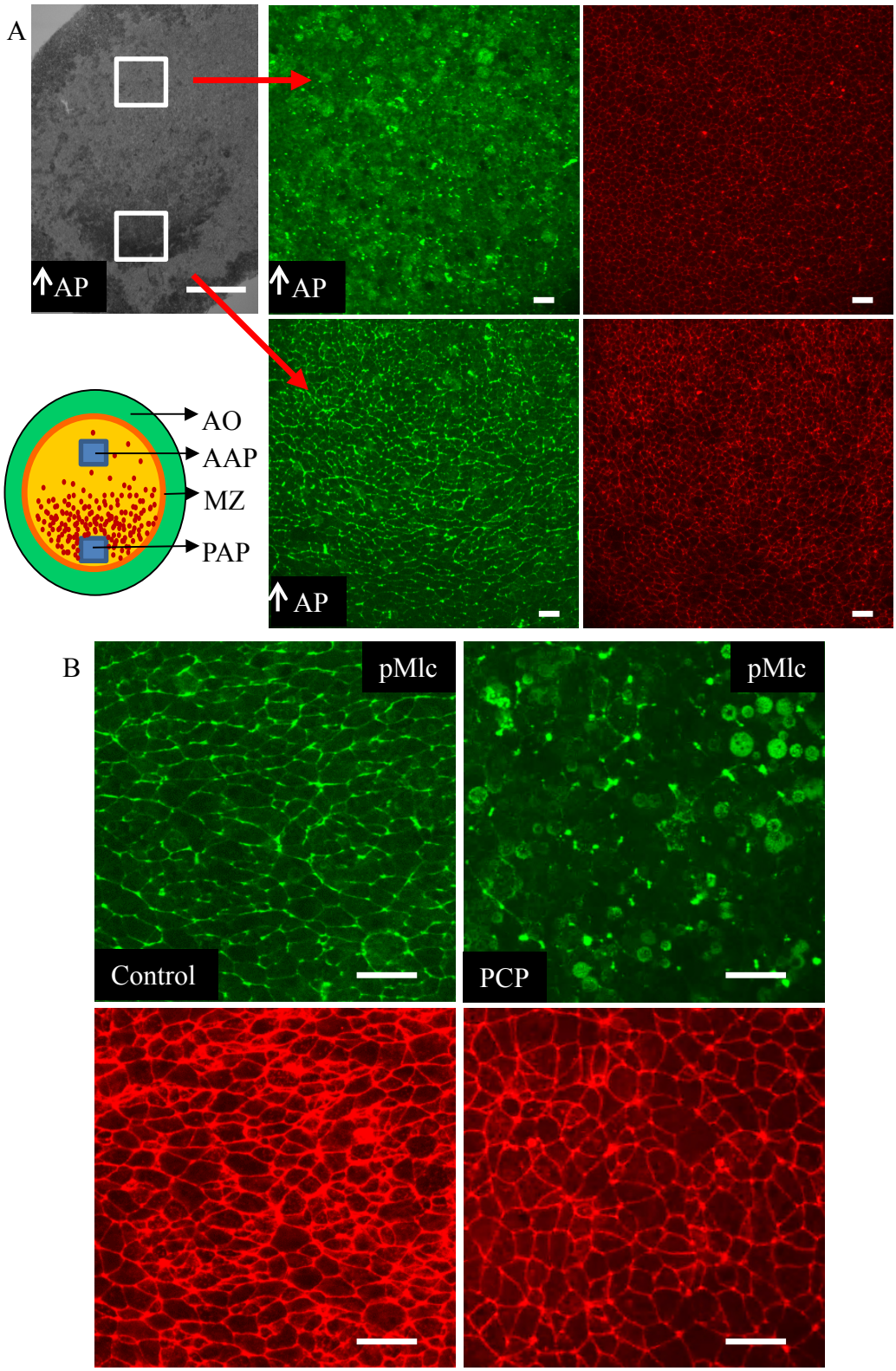

Figure 3.18 Localisation of super cellular phosphorylated Myosin light chain cables (pMlc). A) pMlc (green) organises into super cellular cables in the posterior area pellucida (PAP) (lower row). Actin is stained with red. The cables are not present in the anterior area pellucida (AAP) (top row). **B)** The pMlc cables are not present in posterior area pellucida 2 hours after addition of PCP. Scale bar in first panel is 1 mm and other scale bars are 25 µm.

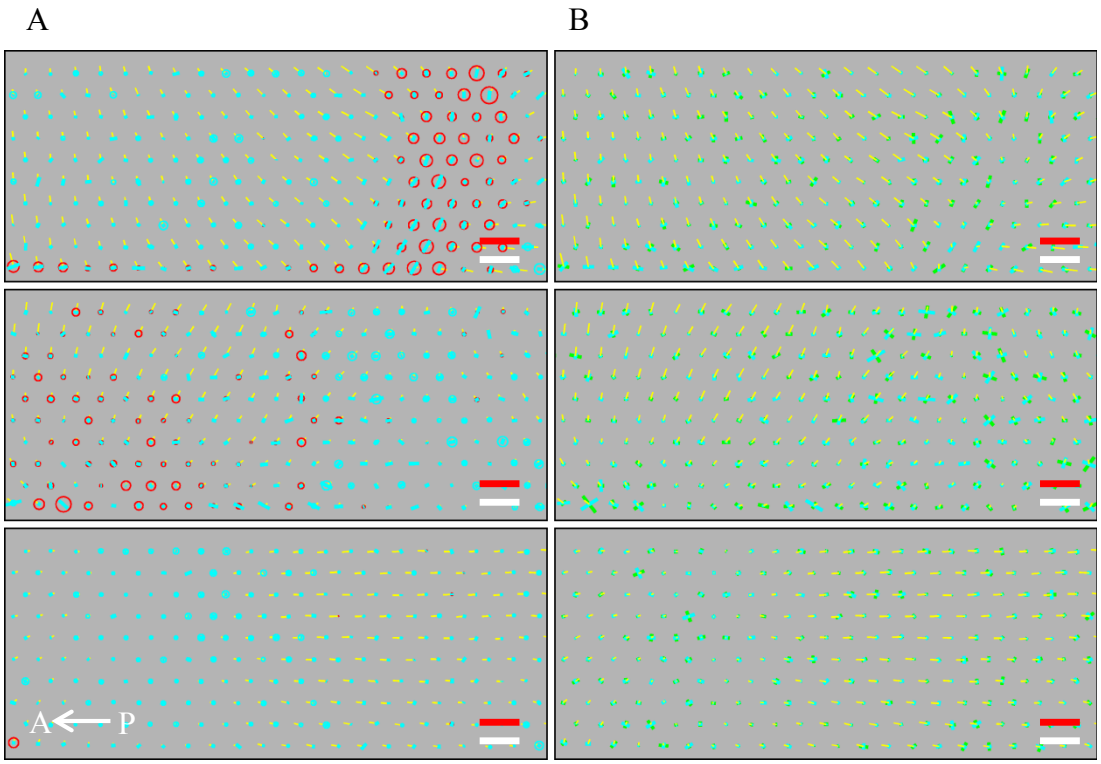

Figure 3.19 Inhibition of Myosin analysed with statistical strain rate analysis. A) Tissue strain rate based on individual cells 5 h before addition (top panel), 30 min after addition (middle panel) and 5 hours after addition (bottom panel). Symmetric part of cell tracks based tissue deformation strain rate tensor. Isotropic component of the strain rate is visualised with blue circles and red circles for contraction and for expansion, respectively. Anisotropic component of the strain rate is shown with blue lines in direction of contraction (the positive component with the same magnitude is not shown). **B)** Anisotropic components of cell shape strain rate and intercalation strain rate. The anisotropic component of the intercalation strain rate is shown with blue lines in direction of contraction (the positive component with the same magnitude is not shown). Similarly, the anisotropic component of the cell shape strain rate is shown with green lines. The white scale bar is 200 µm long. Red scale bar indicates a strain rate of 10^{-4}/s and a tissue domain velocity of 4µm/min.

4 COMPUTATIONAL METHODS

This chapter describes the computational methods used and developed in this work. The first section of this chapter illustrates details of the light sheet microscope used in this study (4.1). The second section shows details of used surface projection algorithm (4.2). The third section explains in detail how embryos imaged in two halves are stitched together. This is followed by detailed description of particle image velocimetry (4.4). Sections 4.5 and 4.6 explain how ImageJ and Matlab have been used, respectively. The next section describes how volumes of dividing cells were estimated (4.7). Sections 4.8 and 4.9 describe two alternative methods for computing cell track and cell outline based tissue statistics. Finally, an automatic drift compensation algorithm for confocal microscopy is described (4.10).

4.1 Light sheet fluorescence microscope used in this study

We used light sheet fluorescence microscope to image cell membranes from chick embryos. The membranes were tagged with Myr-EGFP. The fluorescent chicken strain is explained in detail in our publication[85]. The culture conditions and culture chambers used are described in Nature protocol exchange[86]. Light sheet microscopy is ideal for this study as it enables imaging of whole chick embryo at a resolution at which individual cells are clearly visible. Additionally, light sheet microscopy is well suited for 3D imaging due to low levels of photobleaching and phototoxicity. The setup of our light sheet microscope follows closely the design of a standard scanned fluorescent light sheet microscope[38]. The main difference of our system to the standard one is that both illumination and imaging objectives are oriented at 45° degree angle relative to the horizontal surface of the flat chick embryo. Our light sheet microscope system consists of CMOS camera, a 3-axis stage, a 2-axis scanner and a 488nm solid state laser[85]. Both illumination and imaging objectives are Nikon 10x water immersion objectives.

Embryos are kept in a heated chamber at 37 °C. Several millimetre wide samples are imaged at a 1.84 μm interval. Imaging one time point typically takes 2-3 minutes. To compensate for height variations in the surface of the embryo an automatic height adjustment is performed along the z-axis of the stage (this is described in detail in subsection 4.1.4). In addition, features like the primitive streak might not stay in field of view of the microscope throughout the time sequence. This is compensated using automatic drift compensation (for details see subsection 4.1.5). As a result of imaging, typically, 3000 images (2560x400 pixels) are collected per time point. The amount of image data per time point is then typically 1 TB over period of 15 h. The light sheet microscope is controlled by a dedicated C++ acquisition program and a light sheet microscope program. These two program packages are run parallel on two independent computers and the details are given in following two subsections.

4.1.1 Acquisition program

The acquisition program is responsible for controlling the camera, processing of collected images to perform height adjustment, processing of collected images for drift compensation and for storing the acquired image data on a fast raid system. The acquisition program collects frames at each time point sequentially. The flowchart of the acquisition program is shown in panel A of figure 4.1. The acquisition program keeps track of the time point and current frame being imaged. After initialisation the acquisition program waits for the software library of the camera to send a software trigger signal indicating that the camera has acquired an image. After the signal is received the newly acquired image is read in by the acquisition program. After this the acquisition program checks if a desired number of images have been collected for the current time point. If the desired number is not yet reached the process is repeated. The automatic height adjustment displacement to be applied in the next scan is computed after acquisition of the frame (this process is detailed in subsection 4.1.4).

Once the desired number of images has been collected by the acquisition program the calculated height profile is sent to the light sheet microscope program. This is followed by computation of the automatic drift compensation in case user has enabled this feature (see subsection 4.1.5 for details). The automatic drift compensation keeps the desired feature of the embryo in a selected, fixed position of the field of view. This enables user to image the same feature throughout the experiment. The drift compensation information is sent to the light sheet microscope program. After this the acquired time point is saved to the hard disk. Finally the acquisition program waits for the desired number of time points to be acquired, if yes then the program stops. Otherwise the program proceeds to wait for the first image of the next time point to arrive.

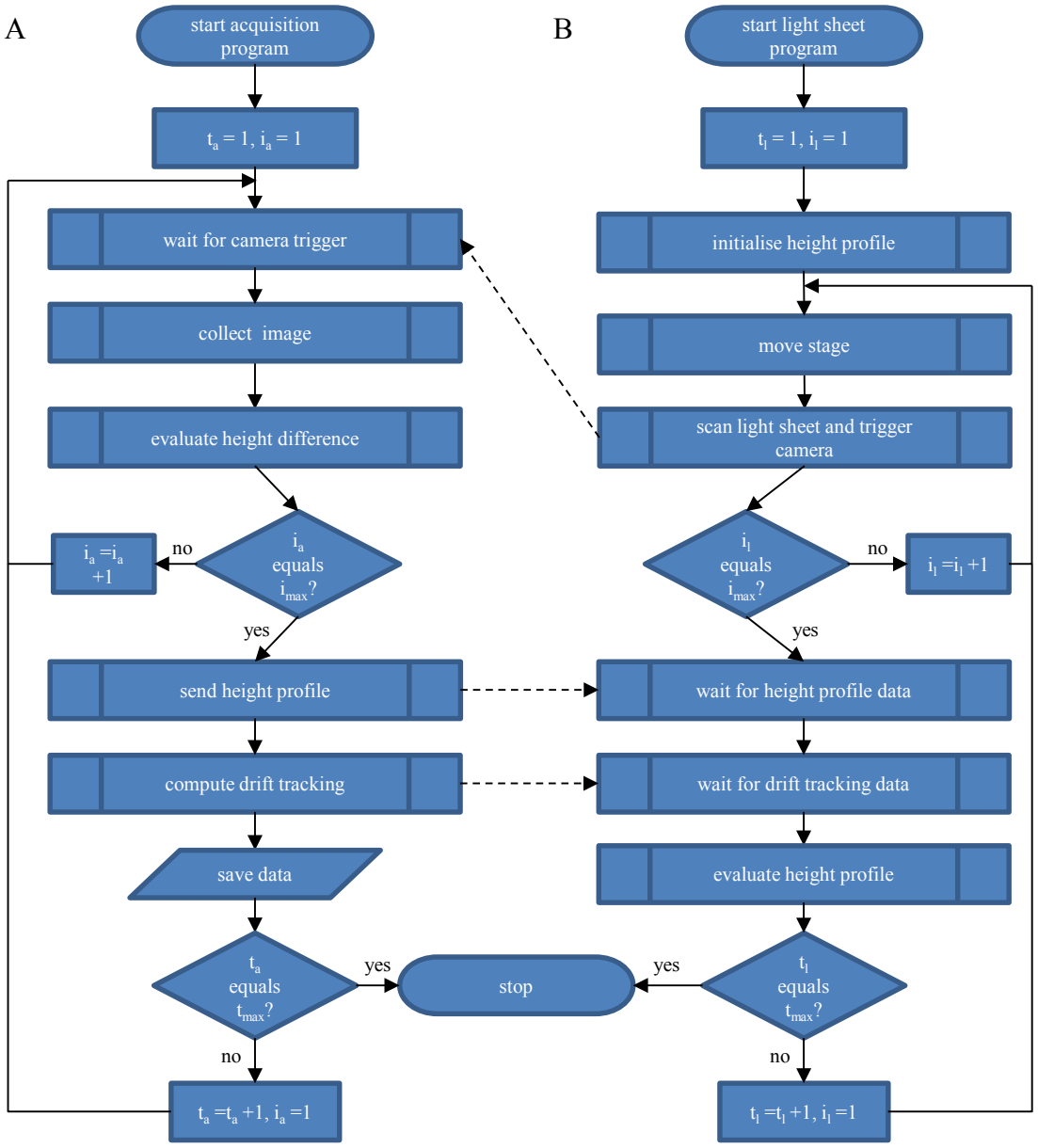

Figure 4.1 Outline of two programs driving light sheet microscope. A) Acquisition program is responsible of collection and storing of images. The acquisition program also evaluates height profiles used for automatic height adjustment. In addition, automatic drift compensation is computed in the acquisition program. **B)** Light sheet microscope program controls all the other hardware devices (laser, scanner and stage). The light sheet microscope program runs parallel with the acquisition program. The light sheet microscope program sends a hardware trigger signal to the camera while light sheet is being scanned. After all the images of a time point have been scanned the light sheet microscope program waits to get height profiles and drift compensation information from the acquisition program.

4.1.2 Light sheet microscope program

Light sheet microscope program is responsible for controlling the laser, the AOTF, the scanner and the stages of the microscope. This program triggers the collection of frames

and time points sequentially. The light sheet microscope program starts by initialising the height profile used by the stages for the collection of the current time point (Figure 4.1). This height profile typically consists of five spatial points used for approximating the surface of the embryo. The user selects these points by visual inspection of the sample for the first time point. Intervals between these five sequential points are linearly interpolated using 1.84 μm steps in x-direction. After initialisation of the height profile the stage is moved to the first position of the profile. This is followed by scanning of the light sheet using the scanner. The scanner triggers the CMOS camera of the microscope using a hardware trigger. After this the stage program checks if the desired number of frames has been collected for the current time point. If the end has not been reached the program repeats the procedure using the next stage position from the height profile.

Once the collection of the current time point is finished the light sheet microscope program waits to receive the surface position information and drift compensation data from the acquisition program. After both have been received the light sheet microscope program calculates a new height profile that is used for acquisition of next time point. The surface position data are used to update the z-coordinates of the height profile in order to drive the surface of the embryo to the desired position for each of the five xz-points separately (see details from subsection 4.1.4). The automatic drift compensation data are used to update the x-coordinates of the five surface profile points. The y-coordinate of all the five profile points is altered using the automatic drift compensation data. Once the new height profile is generated the light sheet microscope program proceeds to the acquisition of the next time point in case desired number of time points has not yet been reached. The program stores the absolute positions of stages for each acquired frame for each time point.

4.1.3 Communication between the two programs

As briefly mentioned in two previous subsections there are three different communications between the two programs. These communications guarantee synchrony between the two programs. The first communication is a hardware signal between the scanner and the camera. This guarantees that an image is acquired every time after the stage has been moved to the desired new position and the scanner is started by the program. An assumption here is that the acquisition program is always ready to receive an image after camera receives the trigger from the light sheet microscope program. Thus it is important for the acquisition program to process the acquired image fast enough.

The second point of communication between the two programs occurs when the light sheet microscope program waits for the acquisition program to send the height profile data. This data is written to a file to the hard disk to a shared folder, which both programs can access. This text file contains an integer number on each row of the file. Each number is then a difference between measured surface position and desired surface position in pixels.

The final point of communication between the acquisition and the light sheet microscope program is the transfer of automatic drift compensation data. This information is written to a file that both programs can access. The (text) file contains two integers representing the displacement vector in pixels that the light sheet microscope program applies to the stage position. Once the acquisition program has written both of these files the acquisition program saves the image data and proceeds to wait the light sheet microscope program to start a new time point.

4.1.4 Automatic height adjustment

The automatic height adjustment is part of the two programs of the light sheet microscope (Figure 4.1). The purpose of the automatic height adjustment is to keep the surface of the embryo as close in the focal plane of the light sheet during scanning as possible. This enables the best possible focus throughout the sample and this also compensates for drifts of the embryo along the z-axis. Another benefit is that the height of the acquired frames can be reduced as surface of the sample is guaranteed to stay in middle of the field of view.

The first step in the automatic height adjustment algorithm is to compute for each acquired frame the difference between the surface of the embryo and a desired height to which surface should be adjusted (Figure 4.2 A). This has to be done for each frame. The desired height is normally in the middle of a frame. To compute the surface position in a frame the central 25% of the image is used to calculate the height (interval between vertical blue lines in figure 4.2 A). To determine the position of the surface the variance of intensities is computed for each row of pixels within the 25% horizontal interval. The row with the highest variance is selected to represent the surface of the embryo (solid red line in figure 4.2 A). The difference between the detected surface and desired position of the surface (dashed red line in figure 4.2 A) is computed for each frame of the point. These computations are performed in the acquisition program immediately after each frame has arrived from the camera.

The computed height difference values are used in the light sheet microscope program to evaluate z-coordinates of the surface profile of the next time point. This is done by adding the difference between current position and the desired position to z-coordinates of each of the points used for controlling profile of the stage positions (points X_i in figure 4.2 B). Old position and new positions are presented with a solid line and with a

dashed line in figure 4.2 B, respectively. To obtain the height difference at point X_i all the height differences on interval $[(X_{i-1}+X_i)/2\ (X_i+X_i+1)/2]$ are averaged.

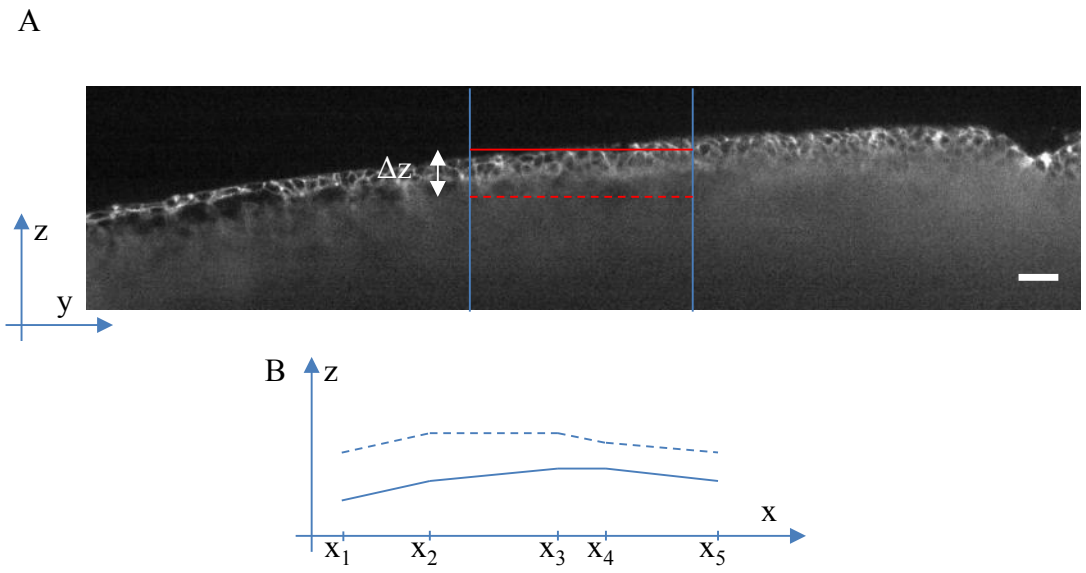

Figure 4.2 Automatic height adjustment. A) Z-coordinate of surface of embryo is estimated by the acquisition program (solid red line). Difference between the detected surface position and desired surface position (dashed red line) is evaluated for each acquired frame and sent to the light sheet microscope program. The image represents a slice through embryo in 45° angle. **B)** Height profile used by stage of the microscope (solid blue line). The previously used height profile is modified in the light sheet microscope program according to the height differences computed in the acquisition program. The white scale bar is 50 µm.

4.1.5 Automatic drift compensation

The automatic drift compensation is part of the two programs controlling the light sheet microscope. The purpose of this algorithm is to allow user to choose a feature from the embryo and then to keep this feature in fixed position in the field of view of the microscope. This type of compensation is useful if one wants to follow for example the primitive streak throughout the time sequence, especially when imaged at higher magnification.

The automatic drift compensation algorithm has to counteract the drifts occurring in the tissue in stage coordinate system (vector $\bar{m}(t)$ in figure 4.3). First the acquisition

program estimates the displacement between images of two consecutive time points using a PIV based method that is implemented in CUDA. This method provides the acquisition program with a vector indicating the magnitude and direction of tissue displacement between two consecutive time points in the image coordinate system (vector $\bar{v}(t)$ between two green dots). The vector is an average vector over local neighbourhood of tissue (200 µm by 200 µm). The vector $\bar{v}(t)$ is measured in pixels and is transformed into the stage coordinate system to obtain vector $\bar{u}(t)$. Finally, the stage motion of in the stage coordinate system between the two time points is denoted with $\bar{s}(t)$. In all these vectors the argument t denotes time interval from time point t-1 to time point t. Using this we can write following

$$\bar{u}(t) = \bar{s}(t) + \bar{m}(t) \tag{4.1}$$

To compensate for the drift of the tissue position the stage needs to be adjusted as follows:

$$\bar{s}(t+1) = -\bar{m}(t) \tag{4.2}$$

When $\bar{m}(t)$ from the first equation is substituted to this the desired form is obtained

$$\bar{s}(t+1) = \bar{s}(t) - \bar{u}(t) \tag{4.3}$$

This formula is applied to achieve continuous stage adjustment that keeps a desired feature of the embryo in a fixed position in the field of view.

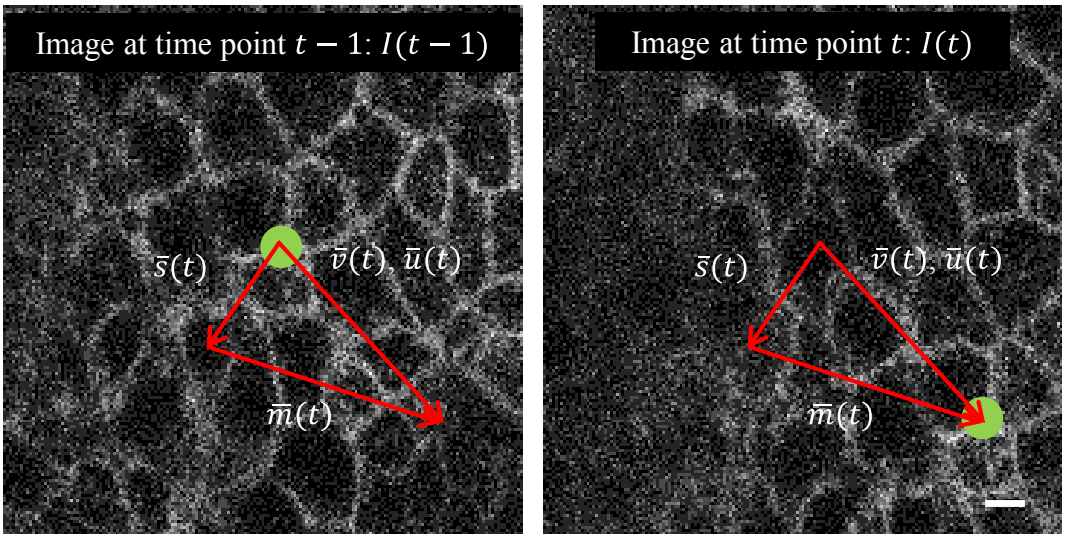

Figure 4.3 Principle of automatic drift compensation. u(t) is a drift of a feature (green dot) in image coordinate system between two consecutive images I(t-1) and I(t). v(t) is the corresponding shift in stage coordinate system. The vector v(t) can be seen as a sum of stage shift between the two consecutive time points and actual drift of the feature in embryos coordinate system. The white scale bar is 5 µm.

An example of automatic tissue drift compensation is illustrated in figure 4.4. The user selects a desired feature (red square close to the primitive streak) from first image using the GUI of the acquisition program (Figure 4.4 A). The algorithm takes the tissue drift into account and preserves the relative position of the primitive streak in the field of view over period of 8.2 h (Figure 4.4 B). During this time interval the embryo drifted over 1 mm both in x-direction and in y-direction (Figure 4.4 C). Initially, the primitive streak is 0.8 mm away from the boundary of the image in in y-direction. If the drift of the embryo was not compensated the primitive streak would had moved out of the field of view of the microscope. The drift of the embryo is not necessarily uniform or linear over time (Figure 4.4 D). In this example the embryo is first drifting slowly for 1 hour. The magnitude of drift then increases rapidly and starts immediately decrease slowly.

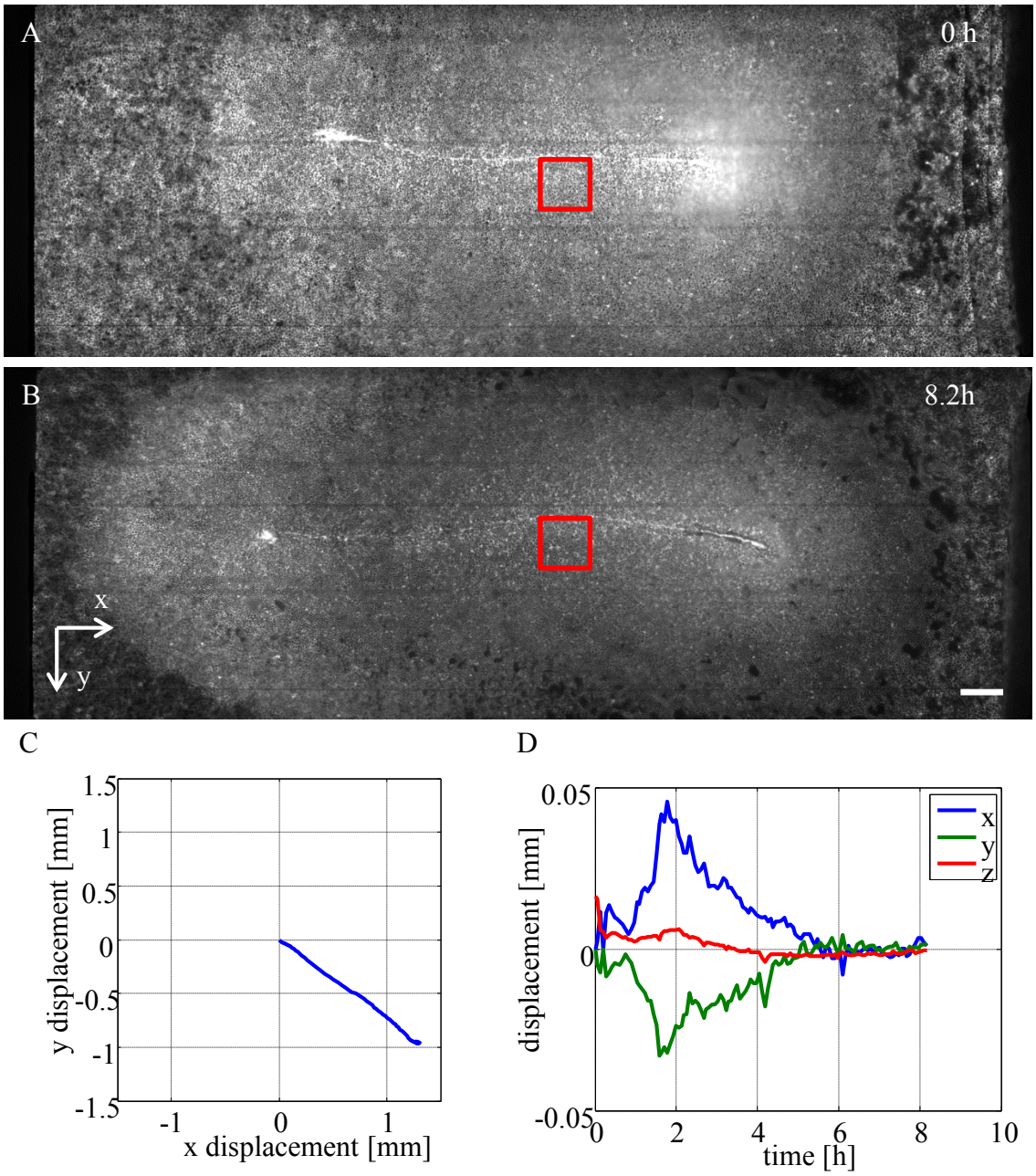

Figure 4.4 Live tissue tracking allows consistent imaging of primitive streak while tissue is drifting. A) In the beginning of experiment microscope's field of view is chosen in a way that primitive streak is middle of the image. In addition, Region Of Interest (ROI) is chosen (red square). The tissue tracking algorithm adjusts automatically stage of the microscope in a way that same part of the embryo is followed by the ROI. **B)** After 8.2 h the primitive streak has elongated and relative location of the primitive streak to ROI is same is in panel A. Scale bar is 200 µm long. **C)** XY Position of the embryo over period of 8.2 h. Initial position is in the origin of the graph. The primitive streak would not be visible in panel B if drift of the tissue had not been compensated. **D)** Adjustments applied to the position of the embryo between consecutive time points. In addition to the X and Y coordinates also height is adjusted (Z coordinate).

4.2 Surface projection algorithm

The surface projection algorithm is used to project an uneven surface of the embryo onto a 2D plane. The algorithm uses the volumetric images collected by the light sheet microscope as input data. The flow diagram of the algorithm is shown in figure 4.5. The 3D images saved by the acquisition program are stored into files that hold the acquired frames in chronological order. The surface projection algorithm reads in these frames and stores them into memory in a rectangular coordinate system in a way that pixels along any coordinate axis are easily accessible.

The surface projection algorithm processes each time point independently, therefore only one time point worth of image data is read into memory. As part of the initialisation each z-plane of the rectangular 3D image is divided into square interrogation windows (64x64 pixels). The algorithm then proceeds to compute surface height independently in each of the interrogation windows. To speed up the computation the algorithm it first considers only every second z-slice within an interrogation window. The algorithm computes for each z-slice how many 2D DFT power spectrum components exceed a certain threshold (here 665). In addition, the average pixel intensity is evaluated for each z-slice. As a next step both sets of values are independently normalised in a range from zero to one. Finally, the normalised number of DFT coefficients is added to the normalised number of average pixel intensities by weighting the latter two times more compared to the first one. Then a z-slice having a maximum sum is taken as an initial estimate of surface height.

This height is then refined by considering z-slices from the interval ranging from four slices above the detected height to four slices below the detected height. Power spectrums of 2D DFTs are evaluated for all the nine z-slices. All the nine power spectrums are then normalised to range from zeros to one using maximum value from

all the nine spectrums. Then the algorithm computes for each z-slice how many normalised components exceed a certain threshold (here 0.74). Finally, the z-slice having maximum number of components exceeding the threshold is considered a surface height for the interrogation window.

Once the surface height is evaluated for each interrogation window the obtained combined surface is smoothened spatially using 3x3 median filter. Finally, the smooth surface is used to interpolate a height map that has a height for each xy pixel. The height map is then used to select which pixels of the rectangular 3D image are used in projected 2D plane. The rectangular 3D image is obtained from the acquired 2D images by interpolating the image volume. For each interpolated pixel the new value is average of two closest pixels (Figure 4.6). The surface projection algorithm is performed independently for all the time points of the time lapse sequence.

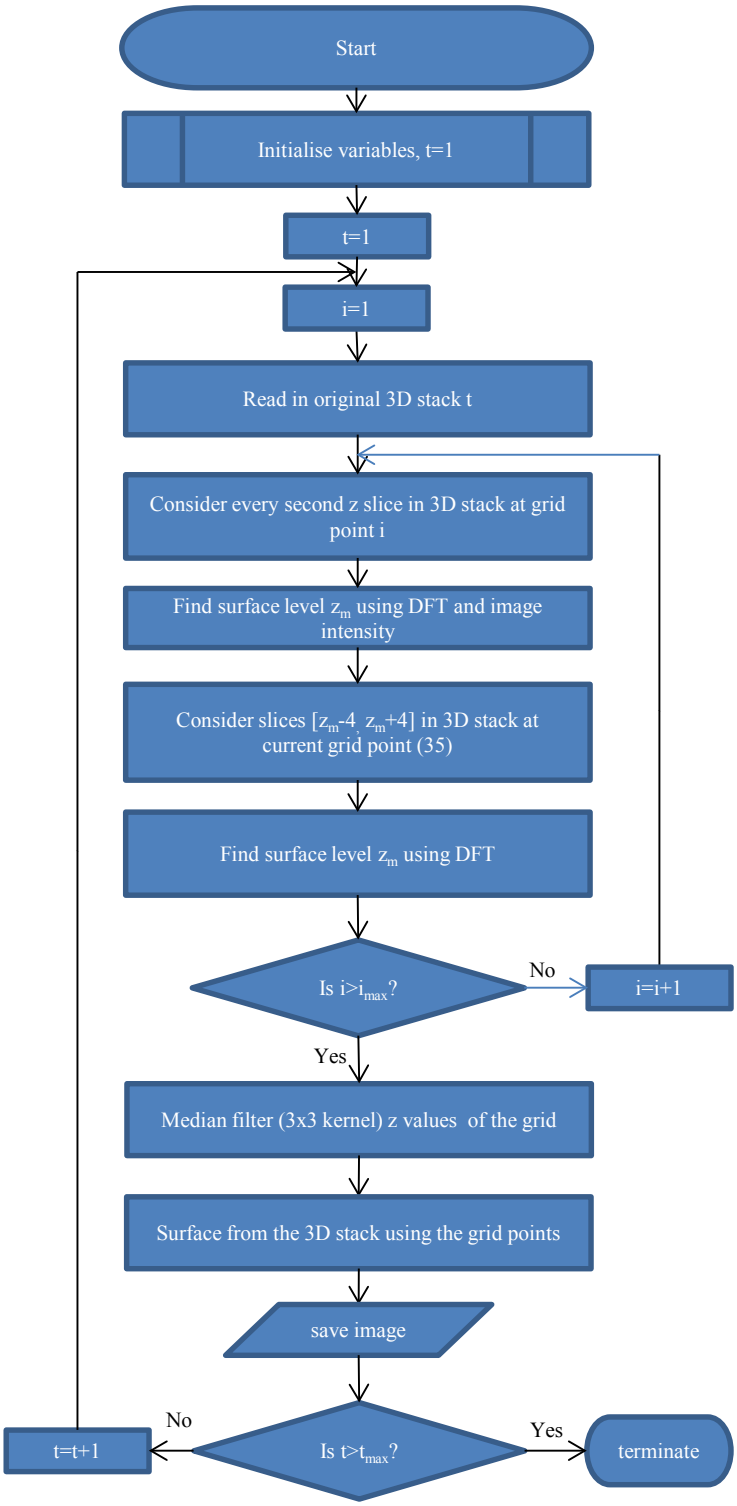

Figure 4.5 Outline of the surface projection algorithm. This algorithm processes raw 3D time sequence and extracts surface of embryo from each time point independently. First raw data of a time point is read in. After this the whole field of view is divided into in a square grid in the xy-plane. Then the algorithm finds surface height in each of these grid squares independently. This is done using DFTs and absolute image intensity. After all the grid points are processed the obtained surface is smoothed spatially. Finally, the smoothened surface is used to extract surface of the embryo into a projected 2D image.

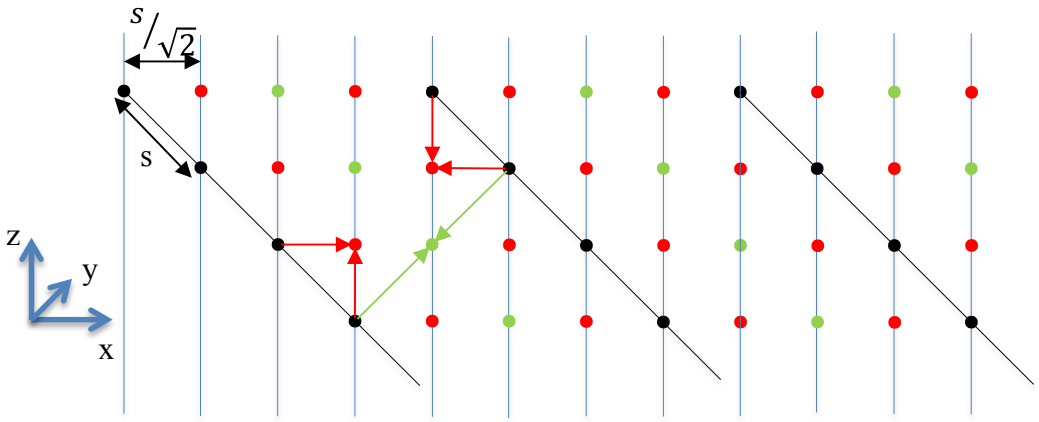

Figure 4.6 Interpolation of volumetric images. Black dots and lines represent original images acquired at 45° angle to the horizontal direction (x-axis). Only one dimension of the acquired images is shown (the other dimension runs along the y-axis). Images are collected with spacing $4s/\sqrt{2}$ where s is the pixel size of the camera. This yields geometry where only every "fourth" image is collected. Pixels of the missing images are represented with red and green pixels. The missing pixels are interpolated from the two closest pixels by taking an average intensity. The missing pixels adjacent to the acquired images (red dots) are interpolated as shown with red arrows (notice that the red planes are not identical but are interpolated in a mutually similar manner). The missing pixels between the acquired images (green dots) are interpolated as shown with green arrows.

4.3 Stitching two halves of embryo

In some of the acquired image sequences two halves of a same embryo were collected sequentially. This resulted in an image sequence with a time difference (typically 3 min) on the boundary between two halves of an embryo (Figure 4.7A). These two halves had to be stitched together to enable accurate PIV velocity field computations and correct tracking of cells. Before stitching the halves the both were independently processed using the surface projection algorithm described in the previous section. To guarantee that no information was lost the halves were acquired so that images overlapped at the boundary (typically 160 pixels).

The easiest procedure for stitching would be to overlap images from both halves and compute average pixel value over these two images. This did not provide good enough results as illustrated in figure 4.7B. To perform better stitching at the interface between

two halves of the embryo PIV based tissue velocity fields were utilised (see details from section 4.4). The velocity field was used to find matching regions between the two halves and this matching information was interpolated to find pixel pairs over the interface. Pixel values of the matching pairs were then averaged over the interface and the new pixel value was placed in middle of the line between two initial pixel positions. After this some pixel values from the interface were possibly missing. These values were filled in using median filter (5x5 kernel size). The described procedure was performed independently for all the time points of the image sequence. This type of stitching provided consistent image over the interface between two halves of the embryo (Figure 4.7C).

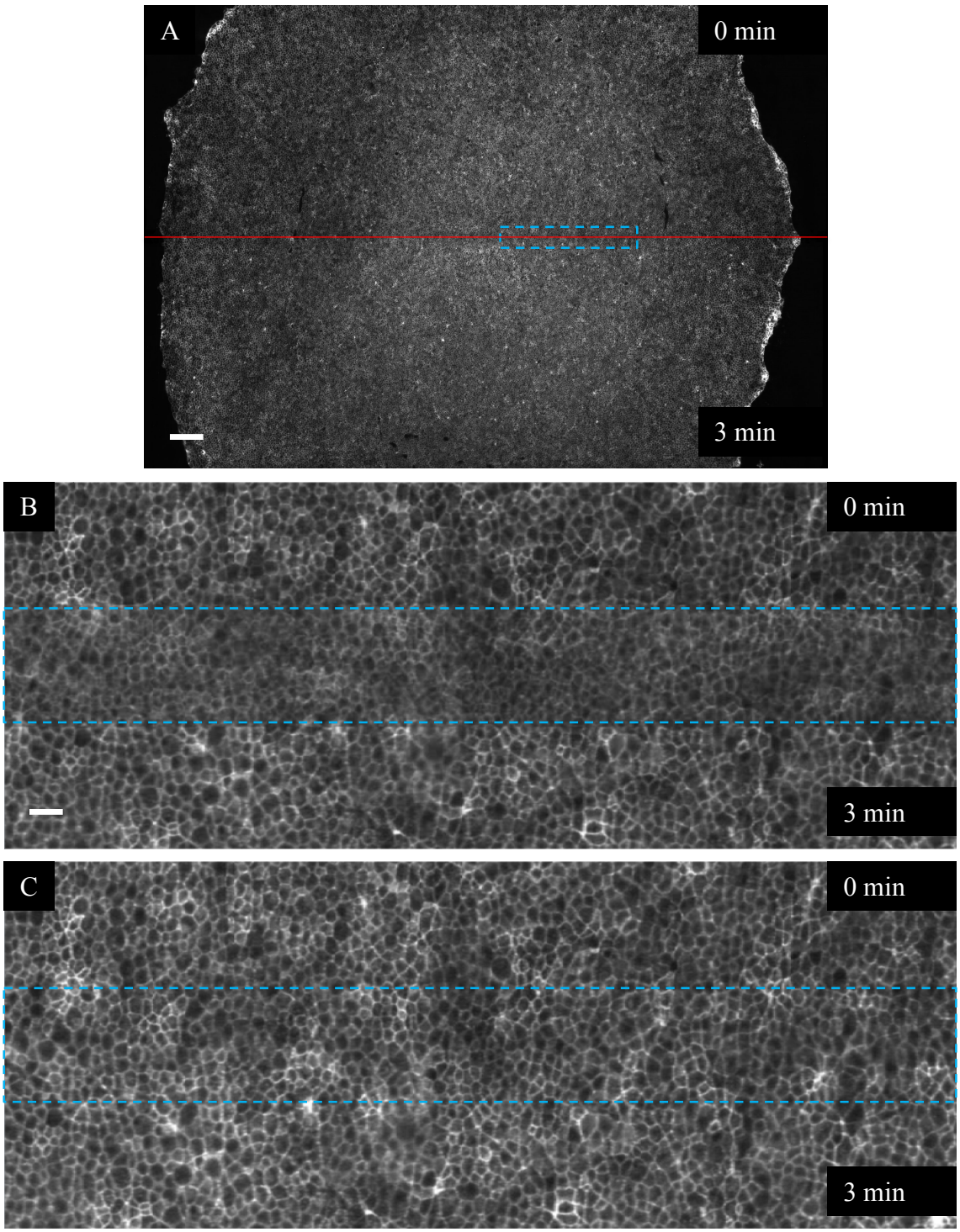

Figure 4.7 Stitching of two halves of embryo. A) The embryo is imaged in two parts, first upper half and then lower half (halves are separated with the red line). The two halves are three minutes apart. The white scale bar is 200 μm. **B)** The two halves are overlapping on the boundary and in this panel the overlapping region (cyan box) is average of the two halves. **C)** In contrast to the panel B the overlapping boundary region is averaged by utilising the PIV to find similar parts of the images from both halves. The white scale bar in B and C is 50 μm.

4.4 Digital particle image velocimetry

Digital particle image velocimetry is a technique used for finding a non-rigid registration between two images. In our case this is a mapping between two consecutive images of a time lapse sequence that shows approximately where each pixel of the first image is located in the second image. To approximate this mapping we are using a Matlab toolbox called PIVLab (version 1.32)[87]. This toolbox performs digital PIV between consecutive pairs of images of an image sequence. We were using piv_FFTmulti.m function of the toolbox that computes the PIV using DFTs to speed up computations. The function also supports using multiple passes for the PIV evaluations. We used interrogation window size of 64x64 pixels for the first pass and 32x32 pixels for the second pass. The overlap between the interrogation areas was chosen to be 50%. The function also uses sub-pixel peak finding and post-processing of the obtained displacement vector between passes to achieve better results[87].

Normally this process is run from the GUI of PIVLab, the toolbox uses only one Matlab process. To speedup this I used parallel computing toolbox to run up to 12 Matlab processes simultaneously to compute different time point intervals of the image sequence. The output of the PIV algorithm is a tissue velocity field where we have a vector for every 16 pixels both in x and y direction representing the displacement of the image region between two consecutive time points. Often for visualisation purposes it is required to perform a spatial or temporal averaging (or both) to visualise the tissue velocity field smoothly (Figure 1.3).

4.4.1 Averaging tissue velocity fields and contraction expansion maps

I have developed an algorithm which allows us to overlay and subsequently, to average the PIV velocity fields from several embryos (Figure 4.8). First, I annotated a point from both anterior and posterior end of primitive streak, separately for each time point

and for each experiment. In addition, I estimated time of onset of motion from each experiment. The annotated points were then used to translate centre point of primitive streak into origin of generalised coordinate system (Figure 4.8A-A'). This was done separately for each embryo and for each time point. This was followed by a rotation of each experiment in order to align all primitive streaks in all time points (Fig 2A'-A''). The time of motion onset was used for temporal alignment of the different experimental time sequences. The same spatial alignment, rotation and temporal alignment was used for corresponding velocity fields.

I used the described algorithm to align 9 different experiments. Outlines of these 9 experiments at three distinct time points are shown 4.8B-B''. Furthermore, taking average of overlaid images verifies that primitive streaks are aligned (Figure 4.8C-C''). Primitive streaks are not yet formed at 0 h (Figure 4.8C). 6 h after the beginning primitive streaks start to be visible as a vertical bright line in middle of the image and finally at 12 h streaks are well visible (Figure 4.8C'-C'').

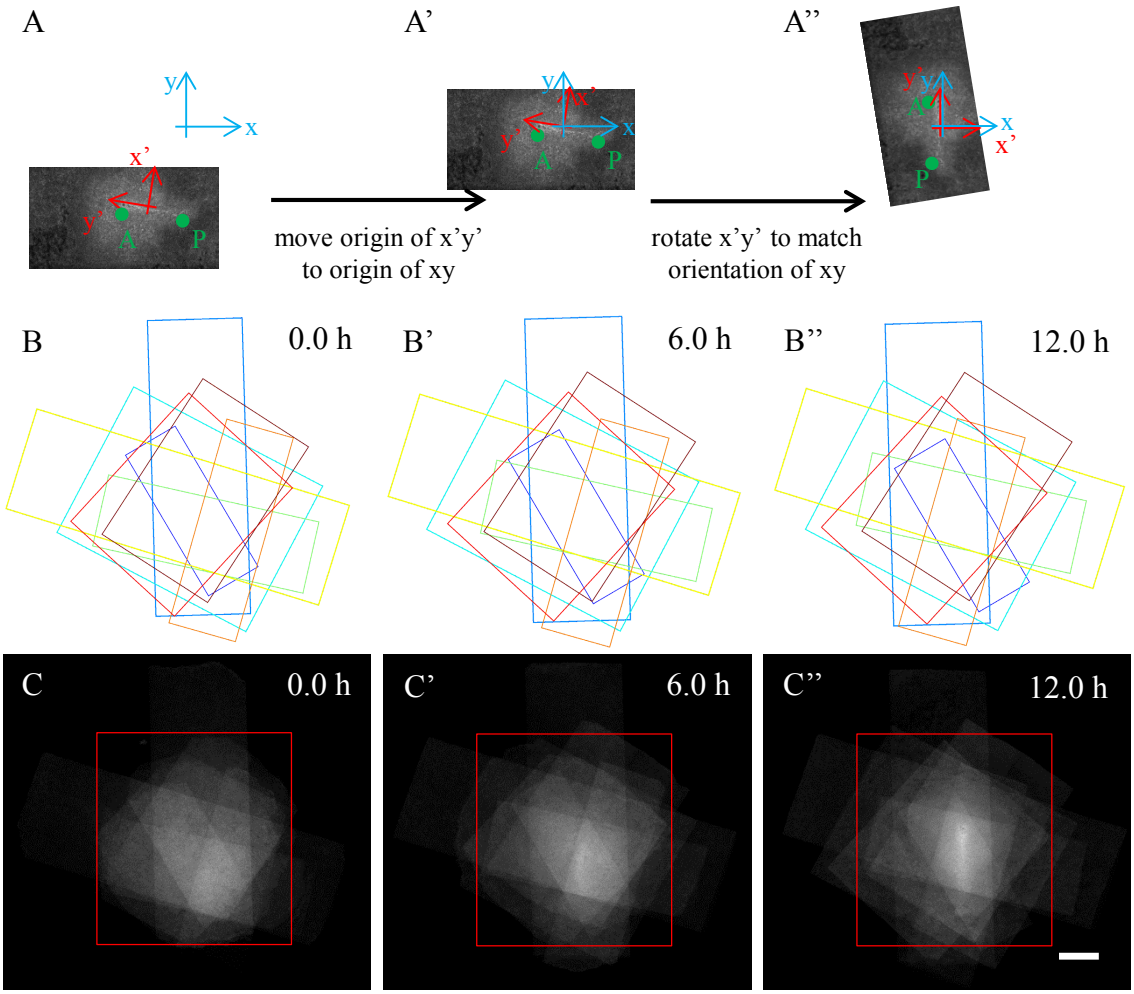

Figure 4.8 Averaging of PIV tissue velocity fields. A) In each experiment and in each time point, location of central point of primitive streak (origin of coordinate system x'y') and orientation of the primitive streak (y' axis points to anterior direction) is different. **A-A')** To take this into account in time sequences the centre point of the primitive streak (origin of the x'y') is moved into origin of general coordinate system xy individually for each time point and for each experiment. **A'-A'')** To correct for the orientation of the primitive streak the y' axis is rotated to point in same direction with the coordinate general coordinate axis y independently for each time point and for each experiment. Anterior and posterior ends of the primitive streak are shown with green blobs (A-A''). **B-B'')** Coloured rectangles represent outlines of nine different experiments in three distinct time points over period of 12 h. **C-C'')** Average intensity of nine overlaid embryos in same spatial and temporal positions as in B-B''. At 12 h the primitive streak is well visible as a vertical line. The white scale bar is 1 mm.

4.4.2 PIV tracking of a region of interest

A desired initial field of view is chosen by defining coordinates of a rectangular image region. The image region is then followed over desired number of time points using a tissue velocity fields. In order to decide how the rectangular image region is moving

between two consecutive time points the tissue velocity field is averaged over the selected rectangular region. The resulting vector is then used to displace each of the corner coordinates of the rectangular region. The procedure is then repeated for a desired number of time points. In each time point, the corner coordinates are used to crop part of the image in order to obtain a stack of images in which the desired part of the tissue appears to be stationary. Due to non-uniform and non-linear flows not all of the initially selected cells are staying in the field of view of the cropped image sequence. A large enough region should be selected to be able to follow cells in the middle of the region throughout the time sequence.

4.4.3 PIV strain rates

We evaluated tissue strain rates using following using spatial gradient of the tissue velocity fields. The velocity field tensor

$$L = \begin{pmatrix} \frac{\partial v_x}{\partial x} & \frac{\partial v_x}{\partial y} \\ \frac{\partial v_y}{\partial x} & \frac{\partial v_y}{\partial y} \end{pmatrix} \tag{4.4}$$

was decomposed in a symmetric part and rotational part. The symmetric part is

$$\xi = \frac{1}{2}(L + L^T) \tag{4.5}$$

Substituting equation (4.4) into equation (4.5) following for is obtained:

$$\xi = \begin{pmatrix} \frac{\partial v_x}{\partial x} & \frac{1}{2}\left(\frac{\partial v_x}{\partial y} + \frac{\partial v_y}{\partial x}\right) \\ \frac{1}{2}\left(\frac{\partial v_x}{\partial y} + \frac{\partial v_y}{\partial x}\right) & \frac{\partial v_y}{\partial y} \end{pmatrix} \tag{4.6}$$

The strain rate tensor of equation (4.6) was then further decomposed into an isotropic expansion contraction term and into an anisotropic shear term as follows:

$$\xi = \frac{1}{2}\begin{pmatrix} \frac{\partial v_x}{\partial x} + \frac{\partial v_y}{\partial y} & 0 \\ 0 & \frac{\partial v_x}{\partial x} + \frac{\partial v_y}{\partial y} \end{pmatrix} + \frac{1}{2}\begin{pmatrix} \frac{\partial v_x}{\partial x} - \frac{\partial v_y}{\partial y} & \left(\frac{\partial v_x}{\partial y} + \frac{\partial v_y}{\partial x}\right) \\ \left(\frac{\partial v_x}{\partial y} + \frac{\partial v_y}{\partial x}\right) & -\frac{\partial v_x}{\partial x} + \frac{\partial v_y}{\partial y} \end{pmatrix} \quad \textbf{(4.7)}$$

In the visualisations the isotropic term was visualised as a blue or red circle for contraction or for expansion, respectively. The anisotropic term was visualised as blue line in direction of contraction (direction of the eigenvector that had negative eigenvalue). The velocity field gradients for the matrix L were estimated using central differences over intervals of 32 pixels. For visualisation the computed strain rate fields were averaged over 10 time points (~ 30 min) and over 13 spatial points (~200 pixels) along both spatial dimensions.

4.5 Image processing in Matlab

Most of the image analysis, cell tracking and analysis of all the tracking data were done using Matlab language and software[88]. The Interp2 function of Matlab was used for linear interpolation of the tissue velocity fields where necessary. In addition, to the core functionality of the Matlab, Image Processing toolbox was used for achieving segmentation. To impose segmentation seed points imhmin function of Matlab was used. After this watershed command of Matlab was utilised to segment the seed pointed image. Watershed algorithm uses the idea that image can be divided into segments by applying idea of basin-like landforms to image pixel intensity landscape[57].

Additionally, the Parallel Computing toolbox of Matlab was used to speed computations where multiple independent instances of loops could be evaluated parallel. This was used to speed up computations of PIV based tissue velocity fields as well as generation of surface projection images for the acquired time lapse sequences.

4.6 Image processing in ImageJ

ImageJ is a software for scientific image analysis[89]. The software is controlled using graphical user interface but can be also controlled using build in macro language for executing the commands. Furthermore, ImageJ can be accessed from the command line without starting the graphical user interface and like this ImageJ may be used completely independently from the user. I utilised this mode of operation to write a Matlab function that can first start ImageJ session on the background and then automatically runs ImageJ macro code from an automatically pointed file. The hard drive of the computer was used to pass image data from the Matlab to the ImageJ and vice versa. With this implemented function ImageJ was used to perform pre-processing of images prior to cell segmentation.

4.7 Quantification of cell volume

In most of the spatio-temporal regions of the embryo it is not possible see the basal side of the epithelial cells when imaging from apical side. This makes the direct cell volume measurements impossible. To solve this problem I measure volumes of cells prior to cell division. Cells prior to cytokinesis round up into spherical shape and are often close to the apical surface of epiblast, which enables measuring the full volume of these cells (Figure 4.9 A shows an example of cell volume prior to a cell division). The volume of a cell prior to cell division can be estimated by using a automatically detected cell centroid (in apical plane) and by maximising mean intensity of volumetric image on a sphere by varying radius of the sphere and depth coordinate of the sphere (Figure 4.9 B). The outline of the optimal sphere is shown in figure 4.9 A as a blue circle.

Figure 4.9 C-E shows the spatial and temporal distribution of cell radii prior to cell divisions. The means of the distributions are decreasing only slightly over time and there are no significant spatial differences in the means. In later time points the

distributions show that smaller cell radii are likely as well (Figure 4.9 E). This is possible due to errors in cell tracking and automated cell division detection. Results in the figure 4.9 suggest that cell volumes are essentially conserved throughout the experiment. A notable temporal difference is that at time interval 4.9-7.3 h the absolute number of cell divisions is higher compared to the earlier or later time points.

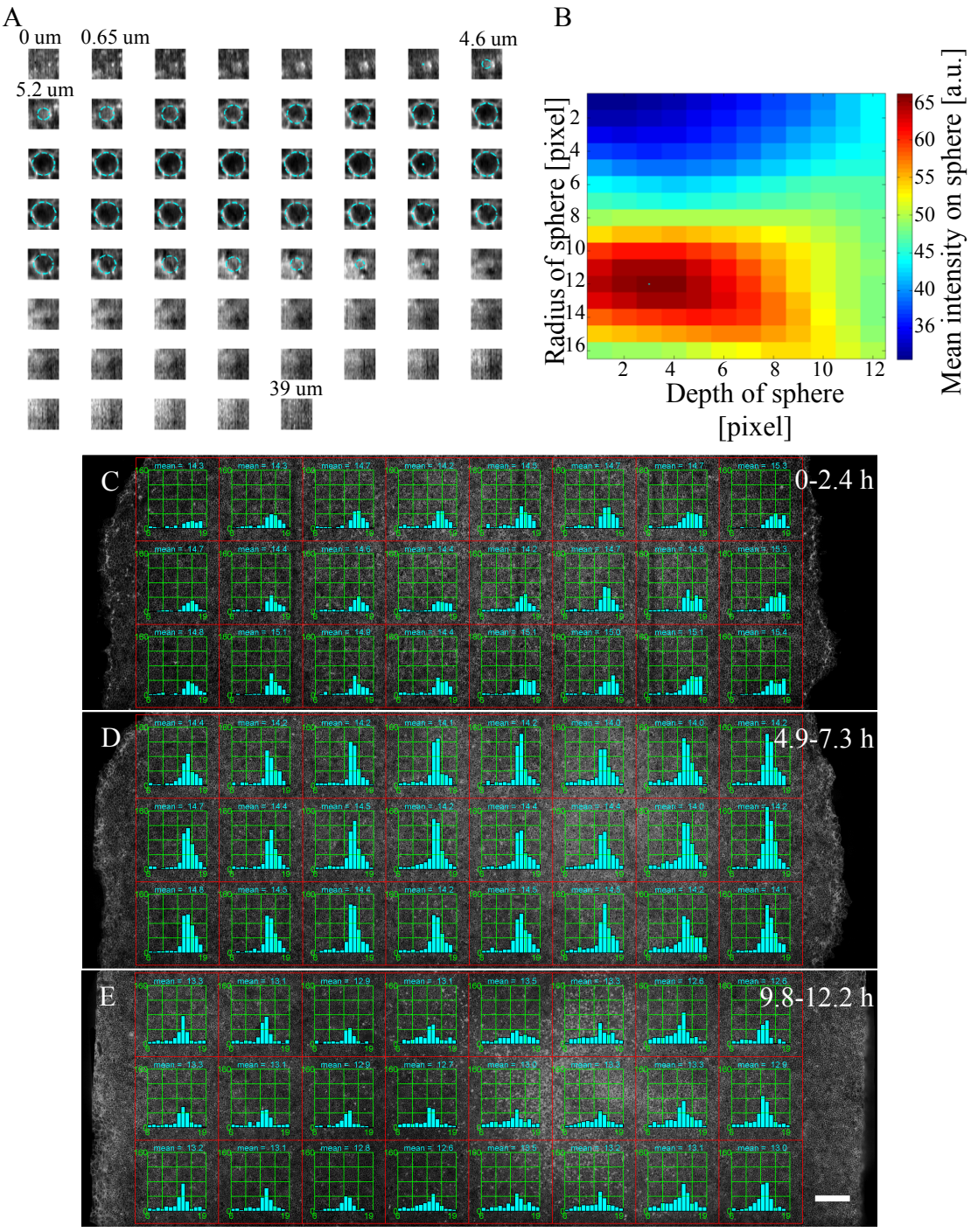

Figure 4.9 Estimation of radius of cell prior to cytokinesis. A) Cross sections of a cell prior to cell division at different heights. The first image (0 um) is from apical side and the last image (39 um) is from basal side. Blue circle in the images represent a sphere approximating outlines of the dividing cell. **B)** The blue line in the panel A is found by maximising intensity of sphere when varying depth of centroid of sphere and radius of the sphere. This panel shows the maximisation landscape. This procedure of is repeated for all the dividing cells in the whole embryo. **C-E)** Distribution of radii of dividing cells in several spatial and temporal regions (means of each distribution are indicated in graphs). There is no strong spatial dependence in the average cell radius, but the average cell radius is decreasing slightly over time. Cell division events are more frequent in panel D compared to the panels C and E. The white scale bar is 200 μm.

4.8 Statistical strain rate tensor computations

These statistical methods have been derived to evaluate the discrete counterparts of the isotropic and anisotropic tissue deformations based on the dynamics of the spatial links connecting the centroids of cells (Figure 4.10)[90]. For the calculation of the cellular deformation based on the positions of the cell centroids we calculated the texture tensor M that provides information on the size, shape and alignment of the cells at a given time point in a particular region[90].

$$M = \begin{pmatrix} \langle X^2 \rangle & \langle XY \rangle \\ \langle YX \rangle & \langle Y^2 \rangle \end{pmatrix} \tag{4.8}$$

Where

$$(X, Y) = (x_2 - x_1, y_2 - y_1) = r_2 - r_1 = l \tag{4.9}$$

The links l were defined as vectors connecting the centroids of neighbouring cells (Figure 4.10). The length and orientation of the links were captured in the so called link matrices which are averaged over the domain of interest. We calculated these averages based on the links between all neighbouring cells in circular domains of 65 μm radius that cover the embryo (Figure 4.10A,A').

The dynamic changes in link length and orientation were used to calculate the statistical symmetrized velocity gradient V, the discrete analogue of the tissue strain rate tensor. It was calculated as follows [90]:

$$V = \frac{N_C}{2N_{tot}} \left(M^{-1}(t) \langle l \otimes \frac{\Delta l}{\Delta t} \rangle + \langle \frac{\Delta l}{\Delta t} \otimes l \rangle M^{-1}(t) \right) \tag{4.10}$$

where

$$\Delta l = l(t + \Delta t/2) - l(t - \Delta t/2) \tag{4.11}$$

Here N_c is the number of links present at both ends points of time interval Δt and N_{tot} is number of all links of cells that have their centroid within the circular domain at the time t. The symbol ⊗ represents the tensor outer product. M is calculated as previously shown. The tensor variation was evaluated between successive time intervals, typically 2.5-3 min (Figure 4.10 B,B').

We also computed the variation of statistical internal strain rate dU/dt. This tensor quantifies how cell size and shape change contribute to the total tissue deformation. The tensor is defined as follows[90]:

$$\frac{dU}{dt} = \frac{1}{2\Delta t}[\log M(t + \Delta t/2) - \log M(t - \Delta t/2)] \quad \textbf{(4.12)}$$

Here links are chosen from end points of the same time interval (Δt) as for evaluation the tensor V (Figure 4.10 D,D').

Finally, we calculated the statistical topological rearrangement rate P. This tensor measures contribution of cell intercalation to the total tissue deformation[90].

$$P = -\frac{1}{2\Delta t N_{tot}}(N_a\langle m_a\rangle - N_d\langle m_d\rangle)M^{-1}(t) \quad \textbf{(4.13)}$$

Where, m_a are links that exist in the end the time interval Δt but not in the beginning and m_d are links that exist in the beginning of the time interval but not in the end. N_a is number of appearing links and N_d is number of disappearing links (Figure 4.10C,C'). For visualisation, the computed tensor fields were displayed as a moving average over 10 time points (~ 30 min).

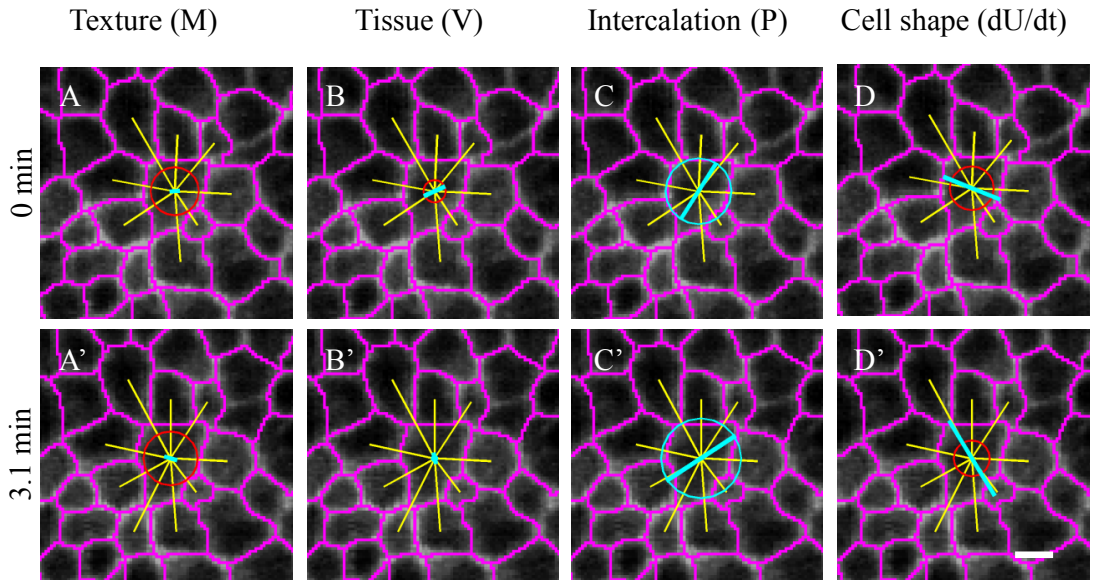

Figure 4.10 Statistical strain rate tensors computed from cell tracks and cell segmentations. AA') Tissue texture tensor computed using link vectors (yellow lines) between centre cell and all the neighbouring cells. Neighbour relationships are determined from the cell segmentation (red pixelated lines). Isotropic part of the tensor is visualised with red circles and with blue circles in case of expansion and contraction of tissue, respectively. Anisotropic part of the tensor is visualised with blue line in direction of contraction. All colours are the same in rest of the panels. **BB')** Tissue deformation tensor computed using changes in preserved links between two consecutive time points. **CC')** Intercalation strain rate tensor is calculated from appearing and disappearing links between two consecutive time points. The intercalation strain rate may not be traceless for a single cell but when averaged over a larger domain a traceless tensor is obtained. **DD')** Change in cell shape tensor is change of the tissue texture tensor over time. The white scale bar is 5 μm.

4.9 Tissue tectonics

This method uses automatic cell tracks and cell segmentation to quantify how tissue is deforming[24]. In addition, relative contribution of intercalation and cell shape changes are quantified by the method. All of these three measures are expressed as tensors (2x2 matrices) for each cell. To compute a tensor for a cell its nearest neighbours and second nearest neighbours are consider from three time points long intervals (in our study ~6 min). The neighbouring cells and the centre cell are called a domain[24].

Firstly a first order approximation of the velocity field within the domain is performed. The constant velocity component is ignored. Then deformation rate tensor is computed

by finding the symmetric part of the approximated tissue velocity field gradient matrix. Eigenvalues and eigenvector of the deformation rate tensor describe magnitude and direction of deformation, respectively. Negative (contraction) and positive (expansion) deformations were visualised from blue lines and with red lines, respectively[24].

The cell shape change strain rate is approximated independently from the deformation strain rate tensor using ellipses fitted to the shapes of the cells within domains. The cell shape change tensor is then computed by approximating the required deformation of an ellipse of a cell from first time point of the interval to the last time point of the interval for each cell within the domain. All these individual deformations are then averaged to obtain a tensor for the cell in the middle. Finally, intercalation strain rate tensor is approximated indirectly by subtracting the cell shape change deformation strain rate from the overall deformation strain rate[24].

4.10 Automatic drift compensation in confocal microscopy

During my project I developed and implemented an algorithm for automatic control of sample position for Leica TCS SP8 MP microscope equipped with Matrix Screener CAM. This algorithm enabled user to select an initial position from embryo and keep imaging the same tissue over time even if sample is drifting along any of the three coordinate axes. The algorithm is implemented in Matlab that is running on the same computer with the software controlling the microscope. Matlab is communicating with the microscope's software using the CAM to adjust position of the stage and to collect images.

The first step in the drift compensation algorithm is for user to choose initial imaging position (X, Y), Z-interval ($[Z_0, Z_1]$) and number of z-slices (Figure 4.11). After this a network communication socket is opened between the script running in Matlab and the software running the microscope. After this consecutive time points will be acquired

until user requests to stop the drift compensation script running in Matlab. A z-stack with pre-defined number of images (and relative heights) is acquired per each acquired time point. The acquisition of a time point is triggered on pre-defined time intervals to achieve constant time interval between consecutive time points. Each slice within a z-stack is acquired independently by first sending a CAM command to move stage to the correct position and subsequently triggering imaging of the slice.

From the first time point the user may choose for which region of the image drift compensation is computed. This is done using the graphical user interface of the drift compensation Matlab script (Figure 4.11). Once the region has been chosen surface height of the embryo is automatically evaluated by finding which acquired z-slice has highest mean intensity within the interrogation region. The height from the first image is then used as a reference height for all the following time points. The difference between the reference height and detected surface height is used to adjust Z-coordinate of the stage position between all the consecutive time intervals.

To compensate drifts occurring along the other two stage axes (x and y), the tissue flow between two consecutive time points is estimated (Figure 4.11). This is done by computing the cross-correlation between images of two consecutive time points within the interrogation region. The location of maximal cross-correlation is then used as the flow vector between the two time points. This process is repeated independently between the selected “surface” slice of the first time point and each slice of the z-stack of the subsequent time point. Finally, the flow vector from the z-slice having the maximum cross-correlation value is chosen to be used as flow vector between the time points. This part of the algorithm is similar to the drift compensation algorithm used for the light sheet microscope (subsection 4.1.5). Previous stage shift is taken into account as shown previously in equation (4.3).

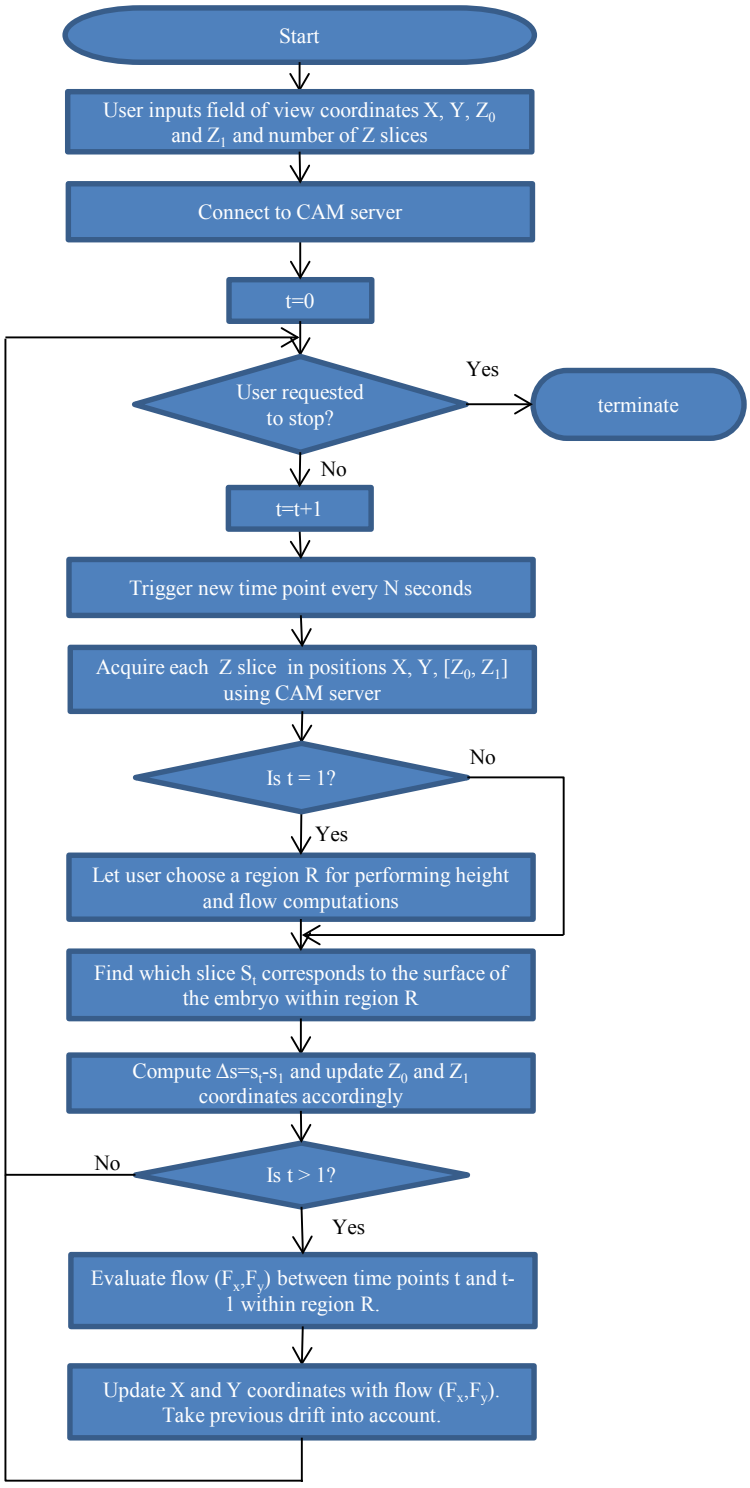

Figure 4.11 Flowchart of tissue drift compensation algorithm for confocal microscope.

The automatic drift compensation algorithm allows imaging of a feature in embryo over several hours while tissue might be drifting along any of the spatial dimensions. As an example we imaged tip of forming primitive streak over 4.8 hours (Figure 4.12 AB). During this time interval the primitive streak was held approximately in middle of the

field of view while the tissue drifted over 500 µm in direction of y axis and nearly 200 µm along the z-axis (Figure 4.12 CD). Without the drift compensation the tip of the streak would have not been visible throughout the imaged time lapse sequence.

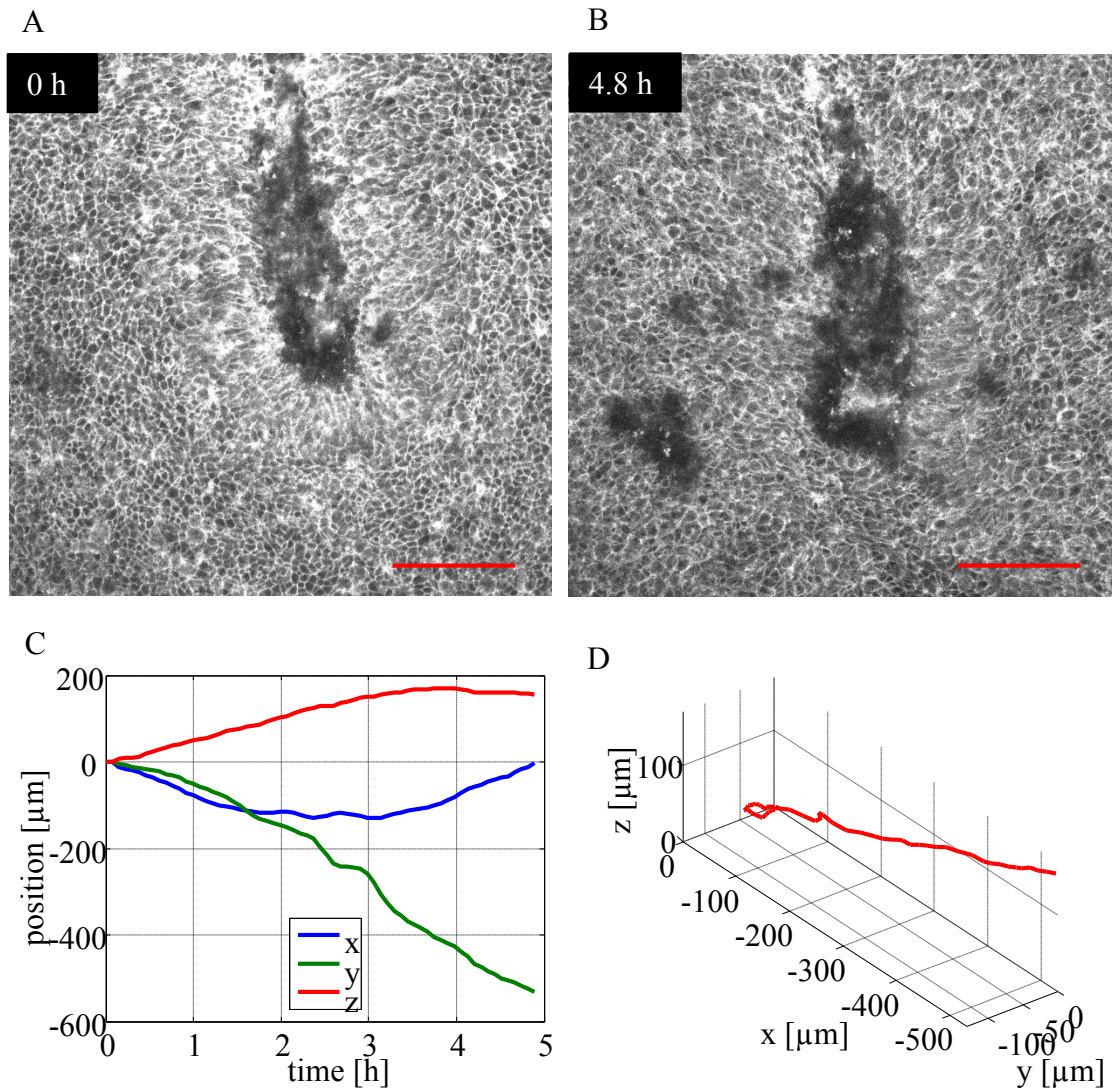

Figure 4.12 Drift compensation for confocal microscope. A) Maximum projection of z-stack (90 µm) in the beginning of the experiment (scale bar 100 µm). **B)** Maximum projection of z-stack (90 µm) 4.8 h after the beginning (Scale bar 100 µm). **C)** Adjustment of embryo's position over time along each of three coordinate axes. **D)** Stage position in 3D axis coordinates. First time point (0 h) is at the origin.

5 PRELIMINARY RESULTS ON LINEAR FILAMENTS BETWEEN THE VITELLINE MEMBRANE AND EPIBLAST

While analysing and processing the volumetric time lapse image sequences of primitive streak formation we identified tubular structures between the vitelline membrane and the apical side of (myr-EGFP) expressing cells. These image sequences were acquired using the light sheet microscope described in the previous chapter (see section 4.1).

The cell membrane tag highlighted tubular structures between the vitelline membrane and the apical side of the epiblast cells (Figure 5.1 A). In rest of this chapter we call these tubular structures filaments. The filaments were not detected prior to the onset of motion in embryo. The filaments could be identified only once epiblast cells started to move relative to the vitelline membrane. Initially the filaments were spanning the space from the apical side of the cells to the vitelline membrane (Figure 5.1 D). Once the epiblast cells started to move the filaments started to elongate in the direction of movement whilst staying connected to the two initial attachment points (Figure 5.1 D). The attachment points in the apical side of cells kept moving with respect the point on the vitelline membrane thereby elongating the filaments (Figure 5.1 D). It seemed that filaments could elongate to span distances covering tens of cell diameters but this maximum distance has not been verified quantitatively. The rate at which the filaments elongated depended of the rate at which the underlying cells moved. The filaments were potentially visible in all the regions of the embryo but it seemed that filaments were denser in the posterior area pellucida where the primitive streak started to form. Furthermore, density of the filaments was higher in the posterior area pellucida where the primitive streak is forming. In every embryo, where at least some filaments were visible, the filaments were found in the posterior are pellucida.

The diameter of the filaments was between one and two microns. The intensity of the filaments was approximately three times less than the intensity of the apical cell membranes (Figure 5.1 BC). This could be due to fact that the filaments are thin structures (compared to the cell membranes) and thus contain less signal molecules. The filaments are difficult to detect since their signal intensity is close to the noise level (Figure 5.1 C). The signal-to-noise ratio varied between different experiments and in most of the experiments no filaments were visible. Most of the filaments had a similar intensity suggesting a rather uniform thickness (Figure 5.1 A). Only few of the filaments were significantly brighter than the others although this has not been analysed quantitatively. For example, brightness of the filament in Figure 5.1 D was not enhanced and intensity on this filament is similar to the intensity on the cell membranes. A reason for this could be that some of the filaments are thicker than others and thus contain more fluorescent signal molecules. The intensity of the filaments was always strongest when the filaments were initially observed and their intensity then gradually faded. Over a period of approximately 10 hours from the onset of motion the majority of filaments were not detectable anymore, this could be due to photobleaching, or due to increased light scattering as a result of bacterial infection.

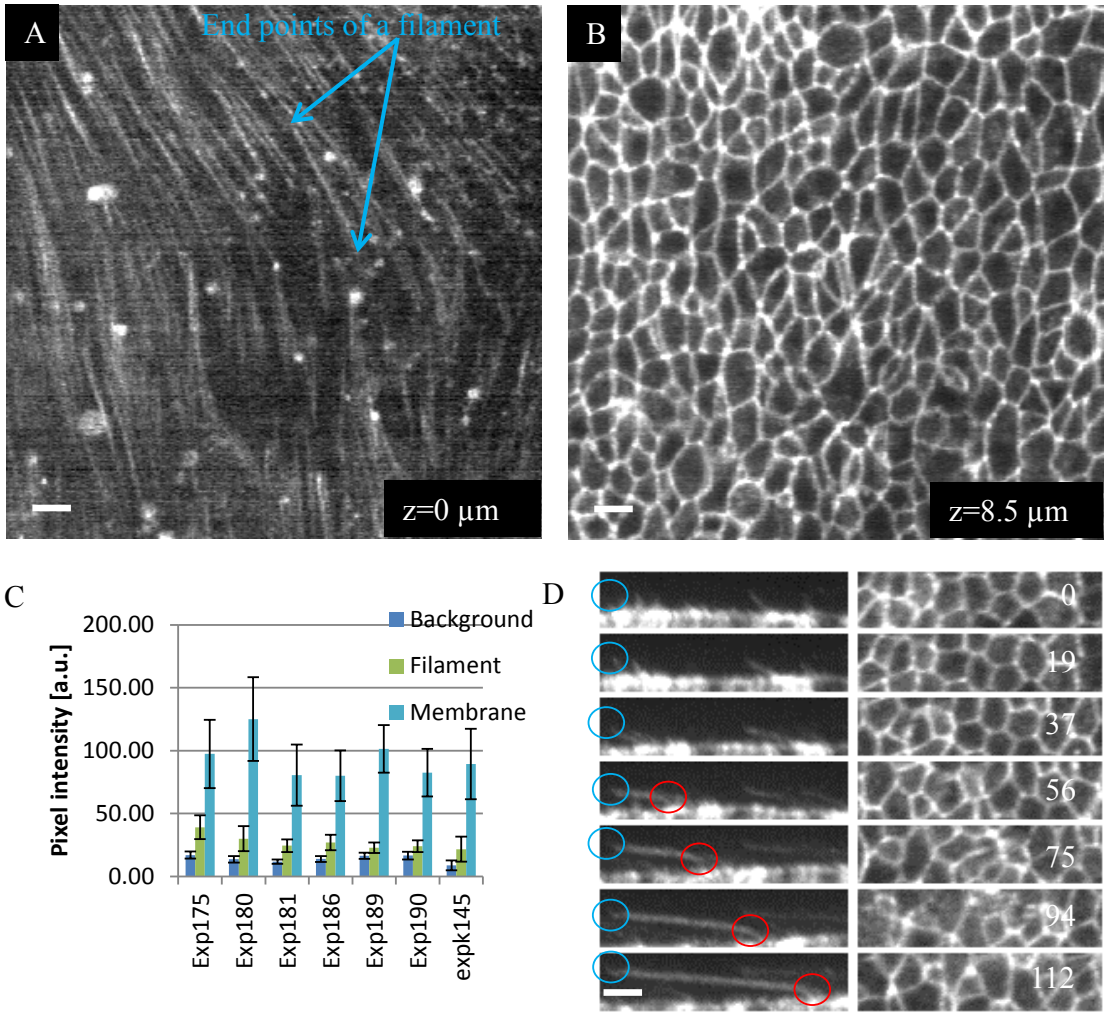

Figure 5.1 Linear filaments between the vitelline membrane and the epiblast. A) Linear filaments spanning over several cell diameters are located between the vitelline membrane and apical side of the epiblast cells. End points of a filament are marked with cyan arrows. These filaments are labelled with same marker (GFP) as the cell membranes. **B)** The apical cell membranes are located 8.5 µm below the filaments. The contrast and brightness of the panels A and B has been adjusted independently as the intensity of the filaments is lower than the intensity of the cell membranes. Brightness of image of panel A has been increased fourfold relative to the panel B. **C)** Intensity of filaments, cell membranes and background in different embryos. **D)** Dorsal ventral cross sections (left column) of a filament over period of two hours. Vitelline membrane end of the filament is marked blue circle and the end attached to the apical side a epiblast cell is marked with red circle. Right column shows the corresponding cross sections of apical side of epiblast cells. Elongation of the filament corresponds to the flow of the epiblast cells. Numbers in the right column are minutes. The white scale bars are 5 µm.

6 DISCUSSION AND FUTURE WORK

6.1 Light sheet microscopy enables robust imaging of cell and tissue movement of the epiblast of the chick embryo

We developed and used a light sheet microscope that enabled us to image the epiblast of the chick embryo during the primitive streak formation (Figure 1.5). The DSLM method was used instead of the SPIM to achieve a better quality light sheet for imaging[35]. To be able to use light sheet microscopy in imaging of the flat chick embryos it was essential to develop a new culture technique[86]. Furthermore, to achieve consistent imaging of all the epiblast cells we developed a transgenic chick strain where the cell membrane are labelled through tagging with Myr-EGP [85]. It is essential to collect information of the majority of cells in epiblast to draw conclusions about the roles of distinct cell behaviours during morphogenesis[60, 64]. One advantage of this chick strain is that cell neighbour relationships can be studied in great detail as the cell membranes are tagged instead of nuclei (Figure 1.4). The ability to label cell membranes has allowed a detailed study of cell behaviours like intercalation and cell shape changes in Drosophila and in zebrafish[24, 79]. Furthermore, light sheet microscopy is an excellent technique for performing this study as photobleaching and phototoxicity are minimal.

As a result of light sheet microscopy imaging we obtained large volumetric time lapse image sequences covering more than half of the chick embryo. Imaging was typical done at 10x magnification with 1.84 um steps by imaging around 2500 slices. After appropriate interpolation this yielded datasets of 8000x2560x300 pixels that was sufficient to observed outlines of cells in detail (Figure 1.4). This provided a basis to study the behaviours of all the individual cells at the position of the forming primitive streak (as will be discussed in following section). Even broader spatial coverage was achieved by imaging two adjacent halves of the embryo in a sequential manner (Figure

1.3). The temporal resolution of single scans was around three minutes, which enabled a detailed spatio-temporal analysis of cell behaviours during formation of the primitive streak. The temporal resolution was at the lower limit of that suitable to observe detailed cell behaviours and a higher temporal resolution, as used with smaller organisms[60, 64], would presumably facilitate the tracking of cells. This was certainly the case in the double scan experiments where it was not always possible to correctly link up cells over time due to too long intervals between successive time points.

To further improve image quality an automatic height adjustment algorithm was implemented to keep the surface of the embryo in the focus of the light sheet (Figure 4.2). This was achieved by automatically adjusting position of the stage of the microscope to compensate for the surface undulations along the AP axis of the embryo. An advantage of a variance based surface finding is that the method is fast[91].Without this feature of the program driving the microscope it would not have been possible to acquire a consistent high quality image of the whole epiblast. This method only achieves optimal focus only along one axis, if surface of the embryo is curved along the medial lateral axis not all areas will be in optimal focus. The dynamic height adjustment enabled a reduction of the volumetric image data to be collected since the surface of the embryo was guaranteed to stay in the middle of the acquired image. This is crucial as the light sheet microscopes generally produce large data sets and any reduction in the size of the image data is useful[35, 48]. In addition to reduction of the image data size, the use of compression algorithms could be utilised to further reduce the data set size for storage but this has not been implemented in our data handling pipeline, since these algorithms are currently still too slow. Reduction of data set size would enable storage of the full data sets for an increased number of experiments.

The processes described above enabled imaging of the primitive streak formation over a period of around 15 h. The previously reported vortical flows are clearly visible in the data sets obtained. These data now form a basis for a detailed reconstruction of the observed cell flows in terms of spatiotemporal patterns of cell behaviours (Figure 1.3)[10]. The level of detail in the acquired volumetric image data sets is similar to the quality achieved with model organisms such as Drosophila and zebrafish[41, 45]. This suggests that similar level of detail of analysis of cell behaviours should be possible as has been achieved in the lower organisms in order to understand morphogenesis[60, 64].

A further development of the program controlling the light sheet microscope enabled us to keep a desired feature of imaged sample in a fixed position in the imaged field of view (Figure 4.4). This was achieved by measuring the displacement of the feature in embryo between the consecutive time points and then adjusting position of the embryo accordingly using the stage of the microscope (Figure 4.3). This enabled imaging of a feature of embryo (like tip of the streak) with high spatial resolution using high magnification (for example 40 times). The ability to observe a fixed piece of tissue at high magnification enables the study of cell behaviours in a greater detail. This feature will be used in future studies to observe how individual cell are behaving in or in the proximity of the primitive streak. This could then provide more detailed information about cell intercalation and cell ingression processes.

A similar automatic drift compensation scheme was developed for controlling a confocal multiphoton microscope (Figure 4.11). This algorithm kept surface of the imaged embryo in a fixed position in an acquired image stack over time. Similarly, a desired feature on the surface of the imaged embryo was kept in a fixed position (Figure 4.12). This enabled detailed imaging of small region of embryo over period of several hours (Figure 4.12). The automatic drift compensation was implemented using the

CAM interface provided by Leica Microsystems. This algorithm enables detailed imaging of a fixed feature of embryo and such a data set may be used for a detailed analysis of cell behaviours at high magnification by two photon microscopy which should allow analysis at larger depth. A disadvantages of the use of the confocal microscope is that it is not possible to acquire dense 3D stacks as are acquired using light sheet microscopy and there is also the added problem of extensive photodamage[35]. The CAM interface allows interaction with software controlling the microscope and has enabled development of interesting user based applications like a rare event detection and high resolution sample screening[92]. The use of the CAM enables in principle the use of a commercial microscope setup to develop user specific imaging protocols, making full use of the existing optics. This is an easier approach as a custom build microscope is not required.

In the future, the temporal resolution of the current light sheet microscope will be improved to enable even more detailed imaging of the chicken embryo. Additionally, the automatic drift compensation will be used to acquire data sets were a feature of embryo (like primitive streak) is imaged with higher magnification which then enables more detailed analysis of cell behaviours. Finally, imaging with several channels would enable simultaneous membrane and nuclei segmentations as has been used in studies of lower organisms[54, 63].

6.2 Automatic cell tracking enables quantitative analysis of large tissues

6.2.1 Extracting 2D image sequences from volumetric microscopy data

The light sheet microscope generates volumetric time lapse image sequences but due to scattering of emitted light the deeper layers are not well visible. This implies that the basal side of epiblast cells was not visible in most parts of the embryo. Thus we decided to extract a cross section through the apical surface of the epiblast of chicken embryo to

perform automatic cell tracking (Figure 4.5). The surface projection algorithm used for extracting the apical surface relied on image intensity and changes in the image intensity (high number of Fourier power spectrum components). This approach worked well if the epiblast was thick enough but especially in the later stages the method started select tissues from the hypoblast. This was a problem particularly outside of the central region (area pellucida) of the embryo. It is critically important to extract best possible surface for tracking. Further improvement of the surface finding would likely facilitate automatic cell tracking and segmentation. One way to improve the surface finding would be to detect the rapid intensity change between apical side of epiblast and low intensity noise on top of the epiblast. Although occasional occurrence of bright objects between vitelline membrane and apical side of cells would need to be handled as a special case in this approach. Projection of 2D surfaces from volumetric image sequences has been a successful approach in quantitative cell tracking based studies of morphogenesis of Drosophila and zebrafish embryos[24, 79].

Secondly, some of the embryos were imaged in two halves in order to cover larger area from the epiblast and thus to increase likelihood to image the whole primitive streak. This increased likelihood to simultaneously image the observed the vortical flows and the entire midline of developing embryo (Figure 1.3). The two halves of embryo were stitched together to generate a continuous surface projection image covering the whole embryo (Figure 4.7). The projected and stitched 2D time lapse image sequence was then used for tracking of cells to achieve a large field of view from the whole embryo (Figure 1.3).

6.2.2 Automatic cell tracking

To track cells and outlines of cells from an embryo wide time lapse sequence containing in the order of 100,000 cells several hundred time points make it not feasible to use

manual methods for annotation and tracking of cells[49]. To achieve tracking and detection of the outlines of each cell within the chick epiblast a tracking algorithm was developed (Figure 2.1 and Figure 2.4). In this algorithm the segmentation (detection of outlines of cells) was performed using a watershed algorithm[57]. Watershed segmentation was chosen in order to avoiding of undersegmentation[49]. Thresholding based segmentation approaches were not suitable in our study since membrane signal was not consistent enough[93]. Level set methods would have not been fast enough for the large scale segmentation and is also not suitable for the tracking approach we have chosen[64]. It is anyway possible that future work on the level set methods would yield results demonstrating their feasibility for solving the cell segmentation and tracking problem in chicken epiblast. Additionally, level set methods are prone to under-segmentation of cells which is not ideal for our efforts to track all the epiblast cells[49]. Watershed algorithms have been successfully used to segment cells in several studies of embryos of other organisms[54, 60-62]. In studies of Drosophila and zebrafish embryos that contain order of 10,000 cells nuclear markers are often used which makes the segmentation task easier[54, 60, 64, 74]. An advantage of cell membrane based segmentation is ability to quantify the cell neighbour relationships accurately, which enables detailed dissection of cell behaviours like intercalation [24, 79, 80].

The temporal sampling interval used in our experiments where cells were potentially moving more than half of average cell diameter between consecutive time points, making the use of tracking methods based on nearest point assignment not applicable[72, 73]. Studies of lower organisms do not suffer this problem as due to their much smaller size the whole tissue can generally be imaged at higher temporal resolution[60, 64]. In addition multidimensional level set methods could not be used to propagate segments over time[64]. Instead the tracking step of our automatic cell tracking algorithm was

achieved by first computing the approximate cell motions between two consecutive time points using PIV[46].

The second step of the tracking algorithm was to use the PIV velocity field to estimate where cells will move between two consecutive time points and finally the watershed segmentation was performed using the estimated new locations as seed points. By assigning the seed points we avoided oversegmentation problem associated to the watershed segmentation technique[49]. In addition, the cell tracking and segmentation were achieved in a same step that conserves the number of segments from time point to the next. The disadvantage of this technique is that cells flowing into the field of view have to be detected separately. As a result we are able to track all the cells in chick epiblast during primitive streak formation. This has not been achieved in previous studies trying to dissect the primitive streak formation[10, 15, 27].

6.2.3 Quality of tracking

The quality of tracking achieved by the automatic tracking algorithm was assessed by comparing the automatically obtained tracks with tracks from the semi-automatically annotated domains. 50% of all the tracks were found to be correct throughout tracking periods and on average 69% of the track lengths were tracked correctly. Some of these tracking errors arise due to cells displaying only small cross sections in the surface of tracking. A reason for cells to have small cross sections is that diving cells exert pressure to the neighbouring cells. Secondly, temporal fluctuations in the absolute heights of surface sectioning induce problems for consistent cell detection. To improve this, global optimisation methods could be used generate consistent cell tracks by connecting segments in a spatiotemporally optimal manner[60, 73]. Another measure for quantifying the correctness of tracking is the cell linkage accuracy. This measure showed initially comparable results (close to 98%) to the linkage accuracy achieved in

tracking of cell nuclei in Drosophila embryos[60, 64, 94]. In later time points the cell linkage accuracy decreased in sections of tissue approaching the site of the forming primitive streak. In these tissues the cross sectional areas of cells are rapidly decreasing and number of narrow cells (small cross sectional area) was too high for the tracking algorithm to work correctly.

The quality of segmentation was quantified using the Dice similarity measure, an on average 90% accuracy was achieved for the first 5 hours of the image sequences. After this the accuracy was decreasing in all the domains, but the decrease was largest in the domains approach the primitive streak. Similar initial segmentation quality has been achieved in zebrafish embryos[54]. One reason for the Dice measure to show poor results towards the end of the time sequences is that several small cells were not correctly detected and thus tissue was undersegmented. This occurs especially in area of the primitive streak.

Cell divisions were detected in our algorithm using heuristic rules. Similar approaches have been taken in case of zebrafish and Drosophila embryos[64]. The F-measure for cell division detection achieved by our algorithm was 0.67. Similar quality of division detection (0.72) has been achieved in a recent study of Drosophila embryo[60]. In other studies cell divisions were automatically detected during Drosophila nervous system development (F-measure 0.48) and later manually curated to obtain correct cell divisions[64]. This type of manual curation would not be possible in our study as the number of cell divisions is much larger and thus manual curation of whole data set would be far too time consuming. To improve the cell division detection capability of our algorithm, global tracking techniques or probabilistic machine learning techniques could be used [60, 73].

Ingressing cells are detected in our automatic tracking algorithm using simple heuristic rules. Ingression detection quality 0.19 (F-measure) is poor and is not good for quantitative ingression detection. To improve ingression detection external cues like high membrane signal intensity of junctions in ingressing cells could be used, although this could be difficult as in many cases membranes of non ingressing cells also have brighter areas. Additionally, when an ingression event occurs, junctions between cells collapse into a single vertex point (with four or more edges). Such vertices could be detected from the segmentation and used to increase probability of detection of ingression events. Furthermore, in the region were ingressions occur frequently the cross sectional areas of cells are small and thus it is presumable not enough to detect ingressions using external cues only but robust a cell tracking is a required. Correct ingression detection is highly dependent on the correct and consistent detection of the surface of the embryo. If this detection is not accurate enough false ingression events may be generated. We observed that in many cases dividing cells are squeezing their neighbours, which also may lead to false positive ingression detection. To solve this problem accurate 3D segmentation of cells would be most helpful, however at present this process is to slow to be practical for our large data sets.

6.2.4 Future work to improve cell tracking

A problem in using 2D projections of surface of epiblast is that the shapes of the cells may vary temporarily as the surface is not always projected from the same position in apical-basal direction. In future, this problem could be solved by performing three-dimensional segmentation as has been performed in lower organisms[60, 64]. Even if this 3D segmentation would not cover full length of cells in apical-basal direction the segmentation could be used for more detailed observation of cell-cell intercalation and cell division processes. In addition, identification of apical side of cells based on sudden intensity change would help to localise the surface of the embryo better. A problem of

this approach would be that bright objects on top of the epiblast that we often observe are likely to interfere with this type of detection. In addition, it might be an interesting idea to try if a spatiotemporally global tracking methods could yield more consistent tracking results[60]. Finally, a use of nuclear marker might enable use of recent methods developed for tracking epithelial cells in Drosophila and in zebrafish[60, 64]. Finally, future work is required to achieve tracking speed that would enable real time tracking of cell as achieved in C++ and GPU powered methods and algorithms[64].

6.3 Tissue deformations and cell behaviours in chicken embryo during the primitive streak formation

6.3.1 Tissue deformation during the primitive streak formation

After onset of motion the central area pellucida starts to contract while all the surrounding regions begin to expand slowly (Figure 3.1). Furthermore, the tissue in posterior area pellucida starts to contract perpendicular to the midline and expand along the forming primitive streak. These cell movement patterns are similar as shown in a previous study[15]. While this process continues the tissue in the anterior end of the forming primitive streak starts to buckle up. The mesendoderm tissue is initially arranged in a sickle shaped region, which then transforms into the primitive streak (Figure 3.2, Figure 3.3 and Figure 3.4). This suggests that cells from the sickle shaped region from the posterior area pellucida are forming the primitive streak.

The tissue strain rate field showed that mesendoderm population of cells contracts in an anisotropic manner perpendicular to the midline of the embryo (and expands along the midline) throughout the primitive streak formation. In a study based on movement of individual scattered cells the authors argued that the anisotropic motion of cells is likely caused by intercalation but could not present evidence based on all the individual cells in the epiblast[15]. Only when the primitive streak has already started to form (but not yet

fully elongated) the tissue in the streak starts to contract in an isotropic manner (Figure 3.2, Figure 3.3 and Figure 3.4). This implies that the anisotropic process starts to act before the isotropic contraction begins. This suggests the primitive streak forms as a biphasic process[27, 85].

The onset of motion in the embryo occurs in the midline of the embryo and then spreads rapidly laterally suggesting that the anisotropic contraction in the midline of the embryo is driven actively[85]. This also implies that the cells from the lateral positions are actively pulled by the cells in the midline in order to induce the observed cell flows. The anterior buckling of the tissue along the forming primitive streak is pushing the cells anterior of the forming streak resulting in lateral expansion of these tissue domains. These two tissue deformations (the posterior pulling and the anterior buckling) are presumable responsible of establishing and maintaining the observed vortical flows identified by tracking the individual cells as reported in literature (Figure 1.2 and Figure 1.3)[13, 15]. We calculated the strain rates in the tissue using PIV based velocity fields as well as from the cell segmentation and tracking data. The results from both methods are in very good agreement, indicating that tissue deformation was robustly measured with both methods (Figure 3.2 and Figure 3.3)[77]. Based on the tissue based measurements and the cell based measurements both cell intercalation, cell shape changes are plausible potential drivers of the observed cell flows and elongation of the primitive streak. A discussion of cell behaviours underlying these deformations is provided in the following subsection.

6.3.2 Cell behaviours driving the primitive streak formation

Starting from the onset of motion and throughout period of the extension of the streak the mesendoderm precursor cells are intercalating (Figure 3.5 and Figure 3.6). This contracts the same sickle shaped cell population in direction perpendicular to the midline of the embryo and elongates the mesendoderm along the forming primitive

streak. This suggests that intercalation is a key driver of the elongation of the primitive streak. Additionally, this mechanism explains the induction of the vortical cell flows as the tissue is pulled to the midline and then further elongated along the midline. Our observations are consistent with an intercalation mechanism[15]. Similar observations based on limited number of cells have been reported in literature but with our analysis it is clear that potentially all the mesendoderm cells are intercalating[15].

In addition to the intercalation the cross sections of the epiblast cells were decreasing over time whilst the volumes of the epiblast cells stayed nearly constant (Figure 3.7). Cross sections of the cells in the posterior area pellucida shrank most (Figure 3.7). Isotropic contraction of the cross sectional cell shapes was weak at the time of onset of motion and got stronger in the site of the primitive streak when the streak had already formed (Figure 3.10). The contraction of the tissue in the site of the primitive streak has been argued to occur only due to ingressing cells but here we have shown that isotropic cell shape changes are also responsible of the tissue contraction[27]. Finally, cells in the site of the primitive streak are ingressing (Figure 3.16 and Figure 3.17). This suggests that the apical contraction of mesendoderm cells culminates to the ingression of cells which then further drives the contraction of mesendoderm cell population. Similar, observations were made in a recent study were authors reported that rate of ingressions is high in the site of forming primitive streak[27]. The ingression events are not detected very accurately using the automatic tracking algorithm and thus exact spatiotemporal patterns of ingression are likely to be inaccurate.

Future work is required to improve the ingression detection in order to quantify the important ingression events accurately. The apical cell contraction mechanism pulls cells from the lateral positions to the midline of the embryo and thus assists formation of the lateral vortical cell flows. In addition, the contraction mechanism counteracts the

elongation of the primitive streak, but magnitude of this counteracting strain rate is not as strong as elongation strain rate induced by intercalation (Figure 3.11). Ingression and apical cell shape change driven deformation mechanism has previously been proposed to drive primitive streak formation[4]. It has been proposed that ingression could be an actively driven with Nodal signalling dependent mechanism[27]. In Drosophila ingressions have been observed to occur passively in some circumstances[95]. We propose that cells in front of the extending streak are squeezed out and may ingress passively.

A previous study has shown that the mechanism driving germband extension during development of Drosophila consist of two processes: cell shape changes and intercalation[79]. This highlights the importance to quantify different cell behaviours simultaneously. It is also worth noting that development of the primitive streak driven by combined intercalation and cell shape change mechanism might not require long range interactions between cells[27].

Prior to the onset of motion polarised cell shapes were oriented perpendicular to midline of the embryo (Figure 3.10 and Figure 3.13). Soon after the motion onset the polarity of cells was largely lost. This oriented polarity of the cell shapes presumably assists the observed intercalation of cells and propagation of pulling forces in direction of the lateral mesendoderm. In addition to the orientation of asymmetrically shaped cells, cell divisions were initially also oriented in the direction perpendicular to the midline of the embryo (Figure 3.15). Similarly, a previous study has reported that some of the cell divisions are polarised in direction of the motion of mother cells, although this study was done only on a small scattered subset of cells of epiblast[15]. Our results show consistent pattern of biased cell division orientations of almost all the divisions in the deforming mesendoderm. Our hypothesis is that the orientations of the cell divisions are biased due to polarised shapes of the cells as has been reported in case of different

model organisms[96, 97]. As the cell divisions are polarised in direction perpendicular to the forming primitive steak it is unlikely the oriented cell divisions would be the driver of elongation of the primitive streak as has been suggested previously[18].

In future studies different chicken embryos could be aligned in a similar spatiotemporal manner as in the contraction-expansion fields (Figure 3.1). This would enable more accurate quantification wild type embryos and also enable detailed comparison of these embryos to inhibitory experiments.

6.3.3 Myosin cables

Myosin light chain phosphorylation was found to localise in the apical cell junctions (Figure 3.18). In the posterior area pellucida the expression was forming 2 to 8 cells long cables that were oriented perpendicular to the forming primitive streak, in direction of the cell flows. The cables were not detected in other regions in the embryo. Inhibition of myosin II prevented the observed cables from forming and also strongly inhibited formation of the primitive streak[85]. This suggests that myosin II is in a key role of junctional contraction that could be the driver of the observed intercalation of the mesendoderm. Interestingly inhibition of myosin I prevented the myosin cables from forming (Figure 3.18). Furthermore, tissue deformation was inhibited completely (Figure 3.19). In addition, the cell shape change and intercalation strain rates were very low and as a result no largescale tissue deformations were observed (Figure 3.19). This suggests that myosin I has role in the formation of myosin II cables. Myosin I has been shown to act as a tension sensor[98]. It is possible that increasing tension on the aligned junctions leads to assembly of myosin II via myosin I mediated mechanism as tissue is contracting. This mechanism would promote contraction of new junctions and thus drive the observed intercalation behaviour. The observed myosin II dependent directional contraction mechanism driving the intercalation of cells is similar to the

mechanism driving Drosophila germband elongation[84]. Similarly, myosin cables were identified to be responsible of rosette based intercalation of cells in Drosophila[99, 100].

6.4 Filaments between vitelline membrane and epiblast of cells in chicken embryo

The cell membrane tag (Myr-EGFP) labelled tubular structures between the apical side of cells and the vitelline membrane (Figure 5.1). These filamentous structures spanned between two points on the apical side of epiblast cells and on the vitelline membrane. During the movement of the epiblast, the filaments elongated since they appeared to stay attached to the same point on the vitelline membrane. As these filaments are tagged with a membrane label it is likely that the filaments are membrane tubes spanning between the two attachment points.

The filaments were not observed in all embryos investigated. A reason for this could be that in most of the experiments the imaging conditions were not suitable for distinguishing the weak fluorescence of the filament signal from noise level in the acquired images. It might be that the filaments can only be seen in highly fluorescent embryos and under conditions of optimal alignment of the light sheet of the microscope. Alternatively, the filaments could be an artefact from the culture method used for imaging chicken embryos with the light sheet microscope[86].

The filaments were spanning tens of cell diameters and diameter of the filaments seemed to vary from one to two microns. The filaments appear to be similar as thin super cellular projections discovered from Drosophila[101]. These projections, called cytonemes, have been found to contain parallel actin filaments bundles and to be thin tubular extensions of plasma membranes of cells[101]. A function of cytonemes in drosophila is to assist Hedgehog signalling that regulates growth[102]. The cytonemes appear geometrically similar to the filaments we found from the chicken embryos.

Filaments were identifiable only once the underlying cells started to move relative the vitelline membrane but presumable the filaments existed even prior the onset of motion. The filaments seemed be strongly visible in the posterior are pellucida in the region where the primitive streak started to form. This suggests that the filaments would have a role in formation of the primitive streak.

Future work on these filaments is required to characterise why the filaments disappear over time. This could be done by annotating both end points of filaments over time and by observing what happens at the time the filaments disappear. Furthermore, the annotation of the apical end of the filament would answer to the question if filaments are attached to the same epiblast cell over time. So far only 10 times magnification has been used to image filaments successfully. In future, experiments with higher magnification (20x or 40x) would presumable provide more details on the localisation of the filaments. Secondly, more work is required to characterise what are the optimal culture and imaging conditions in order to observe the filaments. Thirdly, it is an interesting question whether the filaments contain actin or transmit any signalling molecules as the cytonemes do in Drosophila? Finally, the key question will be to uncover the role of the filaments in primitive streak formation. One hypothesis could be that the filaments are responsible of cell-cell signalling.

REFERENCES

1. Stern, C.D. *Gastrulation, from cells to embryo's*. (Cold Spring Harbor Laboratory Press, New York; 2004).
2. Chuai, M. & Weijer, C.J. The mechanisms underlying primitive streak formation in the chick embryo. *Current topics in developmental biology* **81**, 135-156 (2008).
3. Nakaya, Y. & Sheng, G. Epithelial to mesenchymal transition during gastrulation: an embryological view. *Dev Growth Differ* **50**, 755-766 (2008).
4. Chuai, M., Hughes, D. & Weijer, C.J. Collective epithelial and mesenchymal cell migration during gastrulation. *Current genomics* **13**, 267-277 (2012).
5. Eyal-Giladi, H. & Kochav, S. From cleavage to primitive streak formation: a complementary normal table and a new look at the first stages of the development of the chick. I. General morphology. *Dev Biol* **49**, 321-337 (1976).
6. Downie, J.R. The mechanism of chick blastoderm expansion. *J Embryol Exp Morphol* **35**, 559-575 (1976).
7. Futterman, M.A., García, A.J. & Zamir, E.A. Evidence for partial epithelial-to-mesenchymal transition (pEMT) and recruitment of motile blastoderm edge cells during avian epiboly. *Developmental Dynamics* **240**, 1502-1511 (2011).
8. Stern, C.D. & Downs, K.M. The hypoblast (visceral endoderm): an evo-devo perspective. *Development* **139**, 1059-1069 (2012).
9. Bertocchini, F. & Stern, C.D. The Hypoblast of the Chick Embryo Positions the Primitive Streak by Antagonizing Nodal Signaling. *Developmental cell* **3**, 735-744 (2002).

10. Chuai, M., Zeng, W., Yang, X., Boychenko, V., Glazier, J.A. & Weijer, C.J. Cell movement during chick primitive streak formation. *Dev Biol* **296**, 137-149 (2006).

11. Graeper, L. Die Primitiventwicklung des Huehnchens nach stereokinematographischen Untersuchungen kontrolliert durch vitale Farbmarkierung und verglichen mit der Entwicklung anderer Wirbeltiere. *Wilhelm Roux' Arch. Entwicklungsmechan.Org* **116**, 382-429 (1929).

12. Chuai, M. & Weijer, C.J. Regulation of cell migration during chick gastrulation. *Current opinion in genetics & development* **19**, 343-349 (2009).

13. Cui, C., Yang, X., Chuai, M., Glazier, J.a. & Weijer, C.J. Analysis of tissue flow patterns during primitive streak formation in the chick embryo. *Developmental biology* **284**, 37-47 (2005).

14. Chapman, S.C., Collignon, J., Schoenwolf, G.C. & Lumsden, A. Improved method for chick whole-embryo culture using a filter paper carrier. *Developmental Dynamics* **220**, 284-289. (2001).

15. Voiculescu, O., Bertocchini, F., Wolpert, L., Keller, R.E. & Stern, C.D. The amniote primitive streak is defined by epithelial cell intercalation before gastrulation. *Nature* **449**, 1049-1052 (2007).

16. Yanagawa, N., Sakabe, M., Sakata, H., Yamagishi, T. & Nakajima, Y. Nodal signal is required for morphogenetic movements of epiblast layer in the pre-streak chick blastoderm. *Dev Growth Differ* **53**, 366-377 (2011).

17. Gong, Y., Mo, C. & Fraser, S.E. Planar cell polarity signalling controls cell division orientation during zebrafish gastrulation. *Nature* **430**, 689-693 (2004).

18. Wei, Y. & Mikawa, T. Formation of the avian primitive streak from spatially restricted blastoderm: evidence for polarized cell division in the elongating streak. *Development* **127**, 87-96. (2000).

19. Bodenstein, L. & Stern, C.D. Formation of the chick primitive streak as studied in computer simulations. *Journal of Theoretical Biology* **233**, 253-269 (2005).

20. Mikawa, T., Poh, A.M., Kelly, K.A., Ishii, Y. & Reese, D.E. Induction and patterning of the primitive streak, an organizing center of gastrulation in the amniote. *Developmental Dynamics* **229**, 422-432 (2004).

21. Heisenberg, C.-P. & Tada, M. Wnt Signalling: A Moving Picture Emerges From van gogh. *Current Biology* **12**, R126-R128 (2002).

22. Wallingford, J.B., Rowning, B.A., Vogeli, K.M., Rothbacher, U., Fraser, S.E. & Harland, R.M. Dishevelled controls cell polarity during Xenopus gastrulation. *Nature* **405**, 81-85 (2000).

23. St Johnston, D. & Sanson, B. Epithelial polarity and morphogenesis. *Current opinion in cell biology* **23**, 540-546 (2011).

24. Blanchard, G.B., Kabla, A.J., Schultz, N.L., Butler, L.C., Sanson, B., Gorfinkiel, N., Mahadevan, L. & Adams, R.J. Tissue tectonics: morphogenetic strain rates, cell shape change and intercalation. *Nat Methods* **6**, 458 - 464 (2009).

25. Köppen, M., Fernández, B.G., Carvalho, L., Jacinto, A. & Heisenberg, C.-P. Coordinated cell-shape changes control epithelial movement in zebrafish and Drosophila. *Development* **133**, 2671-2681 (2006).

26. Weinberger, C. & Brick, I. Primary hypoblast development in the chick II. The role of cell division. *Wilhelm Roux' Arch. Entwicklungsmechan.Org* **191**, 127-133 (1982).

27. Voiculescu, O., Bodenstein, L., Lau, I.J. & Stern, C.D. Local cell interactions and self-amplifying individual cell ingression drive amniote gastrulation. *eLife* **3**, e01817 (2014).

28. Chuai, M. & Weijer, C.J. The Mechanisms Underlying Primitive Streak Formation in the Chick Embryo. *Current Topics in Developmental Biology* **81**, 135-156 (2008).

29. Vasiev, B., Balter, A., Chaplain, M., Glazier, J.A. & Weijer, C.J. Modeling Gastrulation in the Chick Embryo: Formation of the Primitive Streak. *PloS one* **5**, e10571 (2010).

30. Graner, F. & Glazier, J.A. Simulation of biological cell sorting using a two-dimensional extended Potts model. *Physical Review Letters* **69**, 2013-2016 (1992).

31. Sandersius, S.A., Chuai, M., Weijer, C.J. & Newman, T.J. A 'chemotactic dipole' mechanism for large-scale vortex motion during primitive streak formation in the chick embryo. *Phys Biol* **8**, 045008 (2011).

32. Zamir, E.A., Rongish, B.J. & Little, C.D. The ECM moves during primitive streak formation--computation of ECM versus cellular motion. *PLoS Biol* **6**, e247 (2008).

33. Chuai, M. & Weijer, C.J. Who moves whom during primitive streak formation in the chick embryo. *HFSP Journal* **3**, 71-76 (2009).

34. Sandersius, S.a., Chuai, M., Weijer, C.J. & Newman, T.J. Correlating cell behavior with tissue topology in embryonic epithelia. *PloS one* **6**, e18081 (2011).

35. Stelzer, E.H.K. Light-sheet fluorescence microscopy for quantitative biology. *Nat Meth* **12**, 23-26 (2015).

36. Huisken J., Swoger J., Del Bene F., Wittbrodt J. & K., S.E.H. Optical Sectioning Deep Inside Live Embryos by Selective Plane Illumination Microscopy. *SCIENCE* **305**, 1007-1009 (2004).

37. Santi, P.A. Light sheet fluorescence microscopy: a review. *J Histochem Cytochem* **59**, 129-138 (2011).

38. Keller, P.J., Schmidt, A.D., Wittbrodt, J. & Stelzer, E.H. Reconstruction of zebrafish early embryonic development by scanned light sheet microscopy. *Science* **322**, 1065-1069 (2008).

39. Huisken, J., Swoger, J., Del Bene, F., Wittbrodt, J. & Stelzer, E.H. Optical sectioning deep inside live embryos by selective plane illumination microscopy. *Science* **305**, 1007-1009 (2004).

40. Keller, P.J., Schmidt, A.D., Santella, A., Khairy, K., Bao, Z., Wittbrodt, J. & Stelzer, E.H.K. Fast, high-contrast imaging of animal development with scanned light sheet-based structured-illumination microscopy. *Nat Meth* **7**, 637-642 (2010).

41. Truong, T.V., Supatto, W., Koos, D.S., Choi, J.M. & Fraser, S.E. Deep and fast live imaging with two-photon scanned light-sheet microscopy. *Nat Methods* **8**, 757-760 (2011).

42. Vettenburg, T., Dalgarno, H.I., Nylk, J., Coll-Llado, C., Ferrier, D.E., Cizmar, T., Gunn-Moore, F.J. & Dholakia, K. Light-sheet microscopy using an Airy beam. *Nat Methods* **11**, 541-544 (2014).

43. Tomer, R., Khairy, K., Amat, F. & Keller, P.J. Quantitative high-speed imaging of entire developing embryos with simultaneous multiview light-sheet microscopy. *Nat Methods* **9**, 755-763 (2012).

44. Verveer, P.J., Swoger, J., Pampaloni, F., Greger, K., Marcello, M. & Stelzer, E.H. High-resolution three-dimensional imaging of large specimens with light sheet-based microscopy. *Nat Methods* **4**, 311-313 (2007).

45. Ahrens, M.B., Orger, M.B., Robson, D.N., Li, J.M. & Keller, P.J. Whole-brain functional imaging at cellular resolution using light-sheet microscopy. *Nat Methods* **10**, 413-420 (2013).

46. Krzic, U., Gunther, S., Saunders, T.E., Streichan, S.J. & Hufnagel, L. Multiview light-sheet microscope for rapid in toto imaging. *Nat Methods* **9**, 730-733 (2012).

47. Weber, M. & Huisken, J. Light sheet microscopy for real-time developmental biology. *Current opinion in genetics & development* **21**, 566-572 (2011).

48. Mikut, R., Dickmeis, T., Driever, W., Geurts, P., Hamprecht, F.A., Kausler, B.X., Ledesma-Carbayo, M.J., Maree, R., Mikula, K., Pantazis, P., Ronneberger, O., Santos, A., Stotzka, R., Strahle, U. & Peyrieras, N. Automated processing of zebrafish imaging data: a survey. *Zebrafish* **10**, 401-421 (2013).

49. Meijering, E., Dzyubachyk, O., Smal, I. & van Cappellen, W.A. Tracking in cell and developmental biology. *Seminars in cell & developmental biology* **20**, 894-902 (2009).

50. Wu, Q. & Kenneth R, C. Chapter 9 - Image Segmentation, in *Microscope Image Processing*. (eds. Q. Wu, F.A. Merchant & K.R. Castleman) 159-194 (Academic Press, Burlington; 2008).

51. Gerlich, D., Mattes, J. & Eils, R. Quantitative motion analysis and visualization of cellular structures. *Methods* **29**, 3-13 (2003).

52. Dormann, D. & Weijer, C.J. Imaging of cell migration. *The EMBO Journal* **25**, 3480-3493 (2006).

53. Meijering, E., Dzyubachyk, O. & Smal, I. Chapter nine - Methods for Cell and Particle Tracking, in *Methods in Enzymology*, Vol. Volume 504. (ed. P.M. conn) 183-200 (Academic Press, 2012).

54. Mosaliganti, K.R., Noche, R.R., Xiong, F., Swinburne, I.a. & Megason, S.G. ACME: Automated Cell Morphology Extractor for Comprehensive Reconstruction of Cell Membranes. *PLoS Computational Biology* **8**, e1002780 (2012).

55. Meijering E., S.I., Dzyubachyk O., Olivo-Marin J.C. Time-Lapse Imaging, in *Microscope Image Processing*. (ed. F.A.M. Q. Wu, K. R. Castleman) 401-440 (Academic Press, 2008).

56. Kachouie, N.N., Fieguth, P., Ramunas, J. & Jervis, E. Probabilistic model-based cell tracking. *Int J Biomed Imaging* **2006**, 12186 (2006).

57. Meyer, F. Topographic distance and watershed lines. *Signal Processing* **38**, 113-125 (1994).

58. Lin, G., Chawla, M.K., Olson, K., Barnes, C.A., Guzowski, J.F., Bjornsson, C., Shain, W. & Roysam, B. A multi-model approach to simultaneous segmentation and classification of heterogeneous populations of cell nuclei in 3D confocal microscope images. *Cytometry. Part A : the journal of the International Society for Analytical Cytology* **71**, 724-736 (2007).

59. Malpica, N., de Solórzano, C.O., Vaquero, J.J., Santos, A., Vallcorba, I., García-Sagredo, J.M. & del Pozo, F. Applying watershed algorithms to the segmentation of clustered nuclei. *Cytometry* **28**, 289-297 (1997).

60. Schiegg, M., Hanslovsky, P., Haubold, C., Koethe, U., Hufnagel, L. & Hamprecht, F.A. Graphical model for joint segmentation and tracking of multiple dividing cells. *Bioinformatics* **31**, 948-956 (2015).

61. Umesh Adiga, P.S. & Chaudhuri, B.B. An efficient method based on watershed and rule-based merging for segmentation of 3-D histo-pathological images. *Pattern Recognition* **34**, 1449-1458 (2001).

62. Olivier, N., Luengo-Oroz, M.A., Duloquin, L., Faure, E., Savy, T., Veilleux, I., Solinas, X., Débarre, D., Bourgine, P., Santos, A., Peyriéras, N. & Beaurepaire, E. Cell Lineage Reconstruction of Early Zebrafish Embryos Using Label-Free Nonlinear Microscopy. *Science* **329**, 967-971 (2010).

63. Luengo-Oroz, M.A., Rubio-Guivernau, J.L., Faure, E., Savy, T., Duloquin, L., Olivier, N., Pastor, D., Ledesma-Carbayo, M., Debarre, D., Bourgine, P., Beaurepaire, E., Peyrieras, N. & Santos, A. Methodology for Reconstructing Early Zebrafish Development From In Vivo Multiphoton Microscopy. *Image Processing, IEEE Transactions on* **21**, 2335-2340 (2012).

64. Amat, F., Lemon, W., Mossing, D.P., McDole, K., Wan, Y., Branson, K., Myers, E.W. & Keller, P.J. Fast, accurate reconstruction of cell lineages from large-scale fluorescence microscopy data. *Nat Methods* **11**, 951-958 (2014).

65. Tarnawski, W., Kurtcuoglu, V., Lorek, P., Bodych, M., Rotter, J., Muszkieta, M., Piwowar, L., Poulikakos, D., Majkowski, M. & Ferrari, A. A Robust Algorithm for Segmenting and Tracking Clustered Cells in Time-Lapse Fluorescent Microscopy. *Biomedical and Health Informatics, IEEE Journal of* **17**, 862-869 (2013).

66. Dufour A., S.V., Tajbakhsh S., Guillén-Aghion N., Olivo-Marin J.C., Zimmer C. Segmenting and tracking fluorescent cells in dynamic 3-D microscopy with coupled active surfaces. *IEEE Trans Image Process* **14**, 1396-1410 (2005).

67. Mikula, K., Peyrieras, N., Remesikova, M. & Stasova, O. Segmentation of 3D cell membrane images by PDE methods and its applications. *Comput Biol Med* **41**, 326-339 (2011).

68. Mikula, K., Špir, R. & Peyriéras, N. Numerical algorithm for tracking cell dynamics in 4D biomedical images. *Discrete and Continuous Dynamical Systems - Series S* **8**, 953-967 (2015).

69. Mikula, K., Špir, R., Smíšek, M., Faure, E. & Peyriéras, N. Nonlinear PDE based numerical methods for cell tracking in zebrafish embryogenesis. *Applied Numerical Mathematics* **95**, 250-266 (2015).

70. Zanella, C., Campana, M., Rizzi, B., Melani, C., Sanguinetti, G., Bourgine, P., Mikula, K., Peyrieras, N. & Sarti, A. Cells Segmentation From 3-D Confocal Images of Early Zebrafish Embryogenesis. *Image Processing, IEEE Transactions on* **19**, 770-781 (2010).

71. Bourgine P., Čunderlík R. , Drblíková-Stašová O., Mikula K., Remešíková M., Peyriéras N., Rizzi B. & A., S. 4D Embryogenesis image analysis using PDE methods of image processing. *Kybernetika* **46**, 226-259 (2010).

72. Li, G., Liu, T., Tarokh, A., Nie, J., Guo, L., Mara, A., Holley, S. & Wong, S.T. 3D cell nuclei segmentation based on gradient flow tracking. *BMC Cell Biol* **8**, 40 (2007).

73. Jaqaman, K., Loerke, D., Mettlen, M., Kuwata, H., Grinstein, S., Schmid, S.L. & Danuser, G. Robust single-particle tracking in live-cell time-lapse sequences. *Nat Methods* **5**, 695-702 (2008).

74. Amat, F., Myers, E.W. & Keller, P.J. Fast and robust optical flow for time-lapse microscopy using super-voxels. *Bioinformatics* **29**, 373-380 (2013).

75. Cicconet, M., Gutwein, M., Gunsalus, K.C. & Geiger, D. Label free cell-tracking and division detection based on 2D time-lapse images for lineage analysis of early embryo development. *Comput Biol Med* **51**, 24-34 (2014).

76. Kanade, T., Zhaozheng, Y., Bise, R., Seungil, H., Sungeun, E., Sandbothe, M.F. & Mei, C. in Applications of Computer Vision (WACV), 2011 IEEE Workshop on 374-3812011).

77. Graner, F., Dollet, B., Raufaste, C. & Marmottant, P. Discrete rearranging disordered patterns, part I: robust statistical tools in two or three dimensions. *The European physical journal. E, Soft matter* **25**, 349-369 (2008).

78. Bosveld, F., Bonnet, I., Guirao, B., Tlili, S., Wang, Z., Petitalot, A., Marchand, R., Bardet, P.L., Marcq, P., Graner, F. & Bellaiche, Y. Mechanical control of morphogenesis by Fat/Dachsous/Four-jointed planar cell polarity pathway. *Science* **336**, 724-727 (2012).

79. Butler, L.C., Blanchard, G.B., Kabla, A.J., Lawrence, N.J., Welchman, D.P., Mahadevan, L., Adams, R.J. & Sanson, B. Cell shape changes indicate a role for extrinsic tensile forces in Drosophila germ-band extension. *Nature cell biology* **11**, 859-864 (2009).

80. Blanchard, G.B., Murugesu, S., Adams, R.J., Martinez-Arias, A. & Gorfinkiel, N. Cytoskeletal dynamics and supracellular organisation of cell shape fluctuations during dorsal closure. *Development* **137**, 2743-2752 (2010).

81. Gorfinkiel, N., Blanchard, G.B., Adams, R.J. & Martinez Arias, A. Mechanical control of global cell behaviour during dorsal closure in Drosophila. *Development* **136**, 1889-1898 (2009).

82. Dice, L.R. Measures of the Amount of Ecologic Association Between Species. *Ecology* **26**, 297-302 (1945).

83. Mulchrone, K.F. & Choudhury, K.R. Fitting an ellipse to an arbitrary shape: implications for strain analysis. *Journal of Structural Geology* **26**, 143-153 (2004).

84. Bertet, C., Sulak, L. & Lecuit, T. Myosin-dependent junction remodelling controls planar cell intercalation and axis elongation. *Nature* **429**, 667-671 (2004).

85. Rozbicki, E., Chuai, M., Karjalainen, A.I., Song, F., Sang, H.M., Martin, R., Knölker, H.-J., MacDonald, M.P. & Weijer, C.J. Myosin-II-mediated cell shape changes and cell intercalation contribute to primitive streak formation. *Nat Cell Biol* **17**, 397-408 (2015).

86. Rozbicki E, Chuai M & CJ, W. Liquid Culture Technique for Early Chick Embryos Suitable for Long Term Live Imaging *Nature Protocol Exchange***:** **http://dx.doi.org/10.1038/protex.2015.012** (2015).

87. Thielicke, W. & Stamhuis, E.J. *PIVlab - Time-Resolved Digital Particle Image Velocimetry Tool for MATLAB*. (2014).

88. MATLAB *version 8.2.0 (2013b)*. (The MathWorks inc., Natick, Massachusetts; 2013).

89. Schneider, C.A., Rasband, W.S. & Eliceiri, K.W. NIH Image to ImageJ: 25 years of image analysis. *Nat Meth* **9**, 671-675 (2012).

90. Graner, F., Dollet, B., Raufaste, C. & Marmottant, P. Discrete rearranging disordered patterns, part I: robust statistical tools in two or three dimensions. *The European physical journal. E, Soft matter* **25**, 349-369 (2008).

91. Yeo, T.T.E., Ong, S.H., Jayasooriah & Sinniah, R. Autofocusing for tissue microscopy. *Image and Vision Computing* **11**, 629-639 (1993).

92. Carro, A., Perez-Martinez, M., Soriano, J., Pisano, D.G. & Megias, D. iMSRC: converting a standard automated microscope into an intelligent screening platform. *Sci. Rep.* **5** (2015).

93. Maska, M., Ulman, V., Svoboda, D., Matula, P., Ederra, C., Urbiola, A., Espana, T., Venkatesan, S., Balak, D.M., Karas, P., Bolckova, T., Streitova, M., Carthel, C., Coraluppi, S., Harder, N., Rohr, K., Magnusson, K.E., Jalden, J., Blau, H.M., Dzyubachyk, O., Krizek, P., Hagen, G.M., Pastor-Escuredo, D., Jimenez-Carretero, D., Ledesma-Carbayo, M.J., Munoz-Barrutia, A., Meijering, E.,

Kozubek, M. & Ortiz-de-Solorzano, C. A benchmark for comparison of cell tracking algorithms. *Bioinformatics* **30**, 1609-1617 (2014).

94. Schiegg, M., Hanslovsky, P., Kausler, B.X., Hufnagel, L. & Hamprecht, F.A. in Computer Vision (ICCV), 2013 IEEE International Conference on 2928-29352013).

95. Marinari, E., Mehonic, A., Curran, S., Gale, J., Duke, T. & Baum, B. Live-cell delamination counterbalances epithelial growth to limit tissue overcrowding. *Nature* **484**, 542-545 (2012).

96. Gillies, Taryn E. & Cabernard, C. Cell Division Orientation in Animals. *Current Biology* **21**, R599-R609 (2011).

97. Morin, X. & Bellaïche, Y. Mitotic Spindle Orientation in Asymmetric and Symmetric Cell Divisions during Animal Development. *Developmental cell* **21**, 102-119 (2011).

98. Laakso, J.M., Lewis, J.H., Shuman, H. & Ostap, E.M. Myosin I can act as a molecular force sensor. *Science* **321**, 133-136 (2008).

99. Blankenship, J.T., Backovic, S.T., Sanny, J.S., Weitz, O. & Zallen, J.A. Multicellular rosette formation links planar cell polarity to tissue morphogenesis. *Dev Cell* **11**, 459-470 (2006).

100. Zallen, J.A. & Blankenship, J.T. Multicellular dynamics during epithelial elongation. *Semin Cell Dev Biol* **19**, 263-270 (2008).

101. Ramírez-Weber, F.-A. & Kornberg, T.B. Cytonemes: Cellular Processes that Project to the Principal Signaling Center in Drosophila Imaginal Discs. *Cell* **97**, 599-607 (1999).

102. Bischoff, M., Gradilla, A.C., Seijo, I., Andres, G., Rodriguez-Navas, C., Gonzalez-Mendez, L. & Guerrero, I. Cytonemes are required for the

establishment of a normal Hedgehog morphogen gradient in Drosophila epithelia. *Nature cell biology* **15**, 1269-1281 (2013).

APPENDIX I

GUI of semi-automatic tracking algorithm

The semi-automatic tracking algorithm described in previous subsection is implemented as a Matlab GUI application. During starting up of the GUI user may load saved tracking session or user may start a new session. In case a new session is started user is asked to select an image sequence for tracking. A basic functionality of the graphical user interface is to change selected time point. This is done by using arrow keys, scroll wheel of mouse or slider shown in the GUI (Supplementary figure 1). The current time is shown in top left corner of the GUI. Another basic functionality is to toggle what is viewed in the image panel of the GUI (Supplementary figure 1). This is done using the checkboxes of the GUI. Options are: current segmentation, time independent segmentation, background image, projection (segmentation seed points) and cell centroids (Supplementary figure 1). Any combination of the five options may the chosen. The save button of the GUI is used to save the tracking session at any time. Background image, current segmentation and time-independent segmentation are shown in grey scale, red outline and green outline, respectively (Supplementary figure 2 A). Cell centroids and projected points are shown as coloured circles and coloured dots, respectively (Supplementary figure 2 AA'). To perform segmentation for the first time point user has to press segmentation button (Supplementary figure 1). Seed points for this segmentation are generated automatically. Result of the segmentation is overlaid with background image in the GUI (Supplementary figure 2 A). A set of cells is automatically selected from the middle of the tracking region and illustrated to user by showing corresponding cell centroids with coloured circles (Supplementary figure 2 A). User may alter which segments are selected by left clicking the segments. After current image is segmented project button of the GUI is enabled and it is used get seed points

for the next segmentation. These new seed points (coloured dots) are overlaid with following image and shown in the image panel of the GUI (Supplementary figure 2 A'). After this a new segmentation may be performed as earlier (Supplementary figure 2 A'').

In some cases the new seed points are not positioned correctly to achieve a desired segmentation as shown in figure 2 B. User may correct this by altering positions of the seed points by first left clicking a seed point and then left clicking a new location (Supplementary figure 2 B'). After this a new segmentation has to be performed to check if segmentation got corrected in a desired manner (Supplementary figure 2 B''). In case of a cell division a new segment is not generated automatically but an under segmentation occurs (Supplementary figure 2 C). To correct for this user has hold shift key while clicking seed point of a cell that has divided. After this, positions of new daughter cells are clicked to generate to new seed points (Supplementary figure 2 C'). Finally, new segmentation is generated as earlier (Supplementary figure 2 C''). In case of an over segmentation or cell ingression user may remove a seed point by holding control key while clicking a seed point and perform a new segmentation (Supplementary figure 2 D'D'D''). If user wants to create a new seed point key 'a' should be pressed after clicking a desired location of the new seed point.

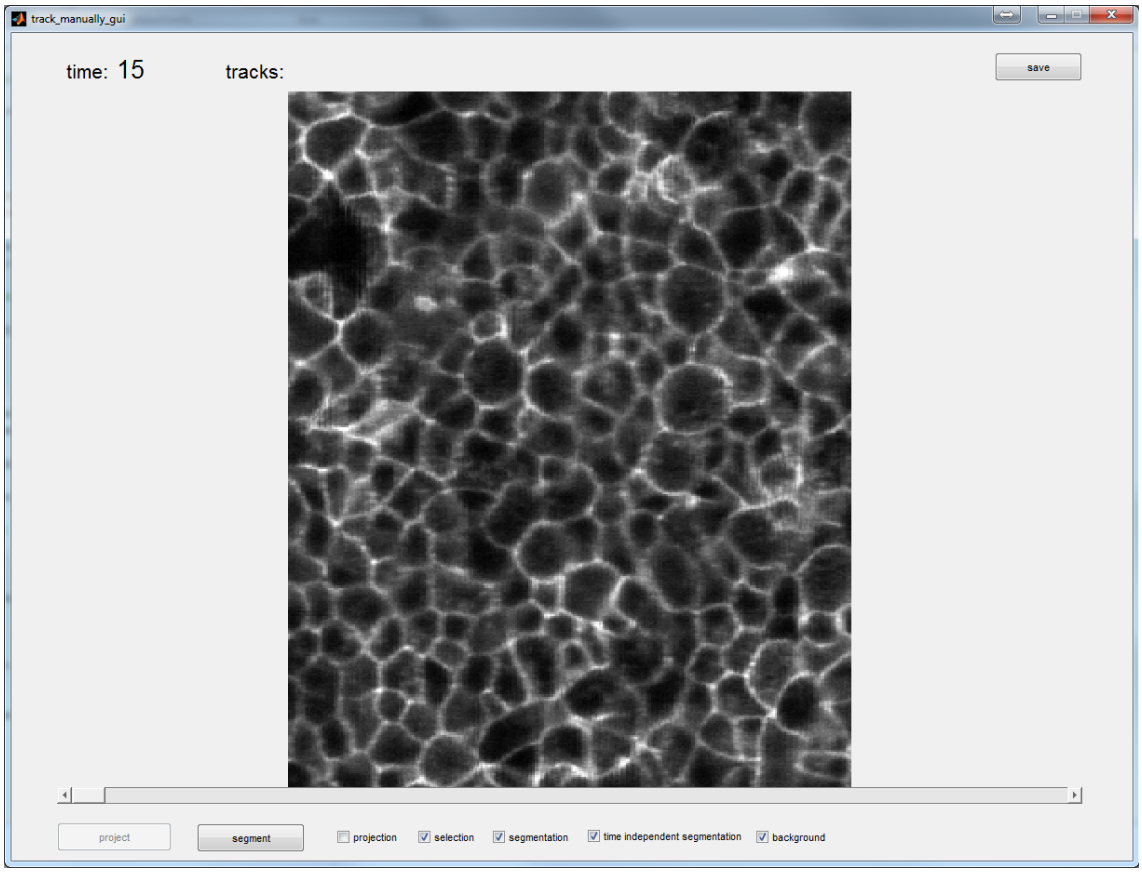

Supplementary figure 1. Graphical user interface of semi-automatic tracking algorithm. Image in the middle shows background image of currently selected time point. Time point number is shown in top left corner. Segment button segments the image using current seed points. In case of initial time point seed points are generated automatically. With project button user may generate seed points for the next time point. User may use slider, scroll wheel or arrow keys to move between time points. Checkboxes are used to alter which all information is overlaid in the image window. Save button is used to save current session.

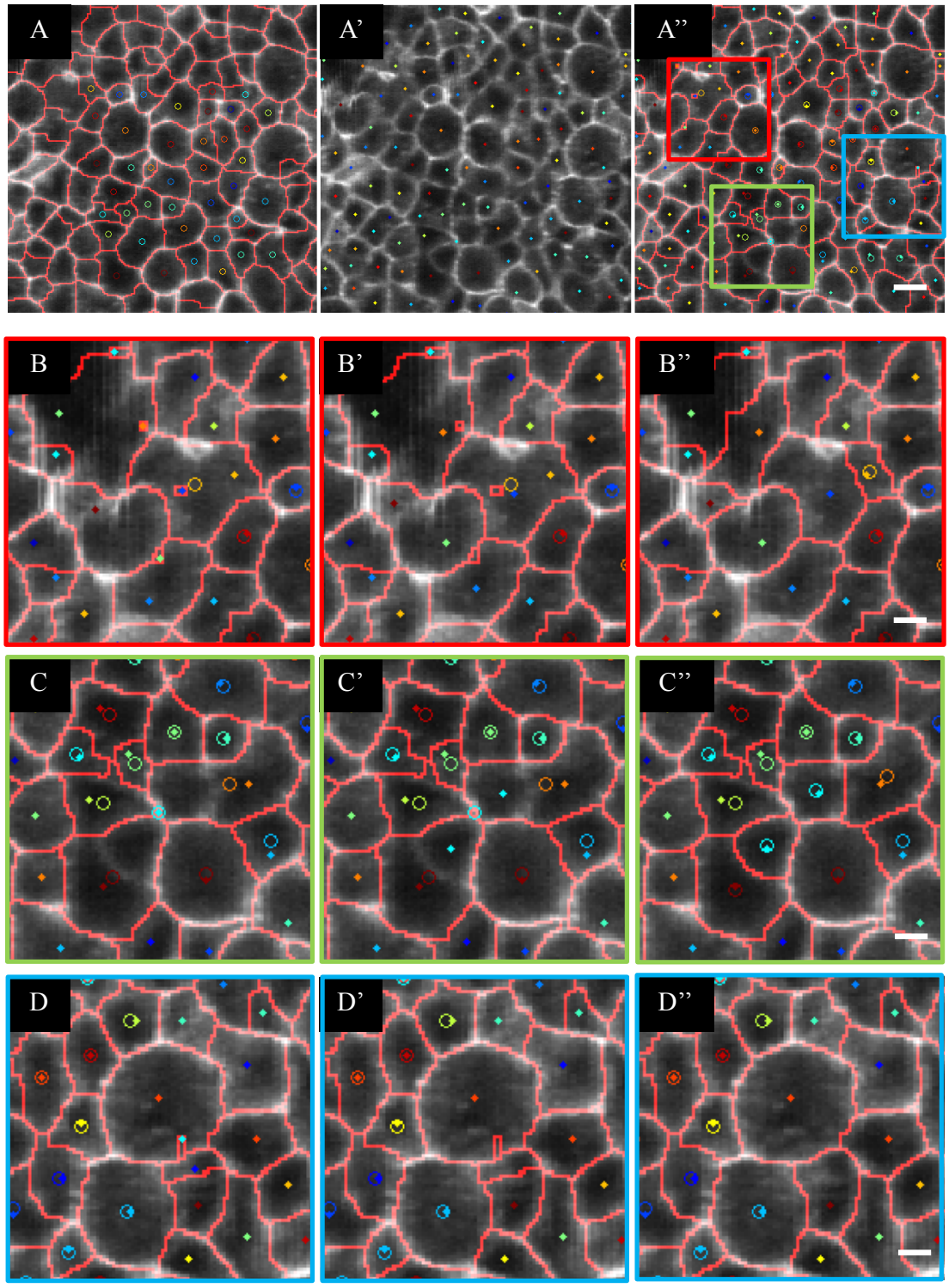

Supplementary figure 2. Use of the semi-automatic tracking algorithm. A) Segmentation of current time point is shown with red pixels. Coloured circles show which centroids user is actively tracking. **A')** Newly generated seed points for the following time point. **A'')** Segmentation of the new time point. **B)** Several mistakes in segmentation. **B')** User has repositioned several seed points. **B'')** New segmentation is generated based on the new seed points. Position of all three B panels is shown as red square in panel A''. **C)** Cell coloured with cyan has divided and is incorrectly segmented. **C')** User induces daughter seed points. **C'')** Position of all three C panels is shown as green square in panel A''. **D)** Cells in the region appear oversegmented or a cell has ingressed. **D')** User removes the seed points. **D'')** Position of all three D panels is shown as blue square in panel A''. The white scale bars are 5 μm in length.